UNIVERSITY OF SOUTHAMPTON

Faculty of Natural and Environmental Sciences

Department of Ocean and Earth Sciences

The Heat, Freshwater and Mass of the Arctic Ocean: A Model Overview

by

Stephen Andrew Fawcett

Thesis for the degree of Doctor of Philosophy

September 2015

UNIVERSITY OF SOUTHAMPTON

ABSTRACT

FACULTY OF NATURAL AND ENVIRONMENTAL SCIENCES

Ocean and Earth Sciences

Thesis for the degree of Doctor of Philosophy

THE HEAT, FRESHWATER AND MASS OF THE ARCTIC OCEAN: A MODEL OVERVIEW

Stephen Andrew Fawcett

The Nucleus for European Modelling of the Ocean (NEMO) Ocean General Circulation Model (OGCM) is shown for the first time to conserve Boussinesq mass at the limit of uncertainty from computer precision when using output data offline, which is sufficient for thermodynamic calculations to be reliable. Long term variability and seasonal cycles of freshwater surface and boundary fluxes show different response rates to perturbations of freshwater flux: a slow baroclinic response leading to freshwater storage and a fast barotropic response redistributing summer river inflow. Two thirds of Arctic Ocean surface heat loss occurs in the Barents and Kara Seas, a region only 14% of its total area. The seasonal thermodynamic storage cycle shows that the limited observations of the Arctic Ocean happen to be made when minimum storage occurs, implying that observations are unbiased by storage.

The Arctic Ocean has an important role in global ocean circulation, sea ice and climate. It is poorly observed, so OGCMs complement observations but these must conserve mass for heat and freshwater estimates to be reliable and independent of any reference value. Atlantic Water is a layer of Atlantic Ocean origin water that enters the Barents Sea, providing a major source of Arctic Ocean heat. Its varying strength has implications for Arctic sea ice and freshwater. The monthly, annual and seasonal patterns of heat and freshwater storage in a modelled Arctic Ocean area are studied from 1981–2007, showing that surface fluxes have a strong seasonal variability and boundary fluxes show a diluted version of this variability. The water circulating through the Barents Sea drastically decreases in temperature as heat is lost to the atmosphere from cooling and formation of ice and denser water. A large surface heat loss also occurs near the Arctic Ocean in the Nordic Seas, from recirculating water from Fram Strait.

Table of Contents

List of tables

List of figures

DECLARATION OF AUTHORSHIP

I, Stephen Andrew Fawcett

declare that this thesis and the work presented in it are my own and has been generated by me as the result of my own original research.

The Heat, Freshwater and Mass of the Arctic Ocean: A Model Overview

I confirm that:

1. This work was done wholly or mainly while in candidature for a research degree at this University;
2. Where any part of this thesis has previously been submitted for a degree or any other qualification at this University or any other institution, this has been clearly stated;
3. Where I have consulted the published work of others, this is always clearly attributed;
4. Where I have quoted from the work of others, the source is always given. With the exception of such quotations, this thesis is entirely my own work;
5. I have acknowledged all main sources of help;
6. Where the thesis is based on work done by myself jointly with others, I have made clear exactly what was done by others and what I have contributed myself;
7. None of this work has been published before submission.

Signed:.....

Date:.....

Acknowledgements

I would firstly like to thank my main supervisor, Sheldon Bacon, for his guidance, discussions and input towards me achieving a complete body of work and Yevgeny Aksenov, for the assistance he has provided me to be able to analyse the data and write the necessary programs, and for the large amount of time he has spent helping me. I would also like to thank the rest of my advisory team, Alberto Naveira Garabato and Kevin Oliver for their insights that they have provided during the course of this project. Additional thanks go to a number of people for the technical support I have received in order to be able to make sense of the programming and the results found in this project: Beverly de Cuevas, George Nurser, Jeffrey Blundell and Gurvan Madec.

On a personal level, I wish to thank the friendship and support of my officemates and other colleagues at the National Oceanography Centre Southampton, the various housemates I have lived with during my time in Southampton and the light relief provided by the members of Southampton University Archery Club. I also want to thank my friends that I have volunteered with and who have inspired me over the last four years at a school science club and an educational charity and finally my family who are always there for me.

Some Definitions and Abbreviations

+ve – positive

-ve – negative

AO – Arctic Oscillation

ASBB – Arctic Shelf Break Branch

BSB – Barents Sea Branch

BSO – Barents Sea Opening

C_v – volume content

CAA – Canadian Arctic Archipelago

CORE II – Coordinate Ocean Experiments, phase II

DFS – Drakkar Forcing System

e_1 – horizontal scaling factor, grid cell length parallel to zonal direction

e_2 – horizontal scaling factor, grid cell length parallel to meridional direction

e_3 – vertical scaling factor, grid cell length perpendicular to the horizontal plane

ECMWF – European Centre for Medium-Range Weather Forecasts

EMP – Evaporation minus precipitation

EVP – Elastic-viscous-plastic

FSB – Fram Strait Branch

f – Coriolis parameter

F_a – Boundary flux

F_s – Surface flux

FW – Freshwater

GCM – General Circulation Model

mSv – milliSverdrup, 10^3 m^3 s^{-1}

LIM – Louvain-la-Neuve Ice Model

NCEP – National Centers for Environmental Prediction

NEMO – Nucleus for European Modelling of the Ocean

NOC – National Oceanographic Centre

OGCM – Ocean General Circulation Model

OPA – Océan PArallélisé

ρ – density

psu – Practical Salinity Units

S – salinity

S' – salinity anomaly

SSH – Sea surface height

Sv – Sverdrup, 10^6 m^3 s^{-1}

T – temperature

TPD – Trans Polar Drift

TW – terawatt

U – vector velocity

v – velocity

v' – velocity anomaly

Chapter 1: Introduction

This section outlines the present knowledge, what is not yet known, and what this project does to increase the knowledge of the scientific community.

This project aims to test the ability of an Ocean General Circulation Model (OGCM) and its diagnostic tools to accurately calculate thermodynamic fluxes and to increase the understanding of the thermodynamic properties of the Arctic Ocean. The properties that are investigated are mass, heat and freshwater.

1.1 Modelling

From the early days of ocean dynamics as a research field, it has been difficult to solve the nonlinear equations of the ocean circulation and the behaviour of the ocean surface, which have an effect on the overall climate. An aim of this branch of work is that we want climate projections to be better in the Arctic. Modelling the oceans is difficult to do well as there are several challenges that models face. A principal issue with achieving an effective Arctic Ocean model is the lack of observations available to help configure initial settings and parameters and to accurately create atmospheric models for the region.

There are difficulties in observing the Arctic Ocean. The remoteness of the region and large logistical costs (i.e., ship time or flight time for on-ice deployment) involved means that only a limited number of instruments can be deployed. Therefore, compromises are made about how much is surveyed, which leads to a sparseness of data. Where the spacing between measurements is greater than 1/3 of the Rossby radius (from less than 1km on

the shelves to ca. 15 km in the central Arctic Ocean, see e.g. Nurser and Bacon, 2013), features of the main ocean circulation and structure of the ocean can be missed since the radius defines the scale of features such as eddies and the width of the boundary currents, such as at the Fram Strait moorings, which are spaced apart at 10 km at the upper shelf slope and 30 km at the deeper area (Schauer and Beszczynska-Möller., 2009).

The temporal discontinuity of observations is another problem, since there are gaps in time series where no data is collected due to instrumental failure or because observational programmes are not continuous or coordinated (e,g, in Bering Strait or Nansen Amundsen Observational System – NABOS). There are seasonal biases in the data. Most of the hydrographic sections are completed in the summer, as the Arctic Ocean is almost completely ice-covered in the winter and icebreakers are required to complete observational transects. Most satellites (except for the recently launched Cryosat-2 in 2010) are not able to provide absolute values of quantities such as ice thickness but they can help with coverage and variability. In the ice free area of the ocean, the harsh winter weather makes a serious obstacle to the measuring programmes. A number of measurements in the central Arctic Ocean were collected from ice camps on winter-spring using sea ice as a platform, introducing a winter bias in the data. As the oceanic conditions change during the surveying time, and the collected data is usually not a true snapshot of the entire region; this is termed as “asynopticity of hydrographic data” (Allen et al., 2001).

This created a gap between the theory and being able to match it to observed data from oceanographic expeditions as the data could be limited. Numerical models were developed to try to use computing in order to help resolve this issue (Bryan, 1969). OGCMs are used to simulate ocean dynamics at both regional and global scales and are of particular benefit to regions where it is

difficult to frequently obtain measurements. They are able to fill in gaps where observations are unavailable or happen infrequently and have poor temporal and spatial resolution. One such inhospitable area is the Arctic Ocean (Steele et al., 2001). Using a set of governing physics and equations, it is vital that they are able to successfully replicate known conditions in order to be used to estimate what may happen in the future to Earth's climate, for which the ocean circulation has a role. They must also do so in such a way so that the results can be trusted to be reliable, as simplifications are made in order for the governing equations to be solved effectively and efficiently. Models such as NEMO are widely used and are generally accepted to work properly, though they have limitations such as the calculations of averages of averages (Roullet and Madec, 2000, Tsubouchi et al., 2012). A fundamental property of an OGCM like NEMO is that it conserves mass, which means that a temperature flux is the equivalent of a heat flux as within the system the calculations are independent of any reference temperature used, and freshwater storage is likewise independent of the reference salinity chosen. The mass conservation is often assumed but has never been tested. Since mass conservation should be perfect in the model, testing this will give an understanding towards the uncertainties in calculations stemming from the design of the model and the processing of the numbers involved from the running of the model and the diagnostic software used to analyse the data. It will also suggest whether any uncertainty that is introduced from the calculations significantly impacts other more complex variables such as heat and freshwater.

1.2 Thermodynamic properties

The Arctic Ocean is an area of scientific interest because of the role it has in driving the global circulation (Dickson et al., 2007) and the climate (Thompson and Wallace, 1998) due to the inflow of warm water, outflow of cold water, sea ice coverage (Rind et al., 1995) and it being almost surrounded by land except for four principal entrances to the rest of the global ocean (Aagaard and Carmack, 1989).

Two of the major vertical structures in the Arctic Ocean are the halocline and the Atlantic layers. The halocline is a cold layer below the surface that serves as a pycnocline due to the density being more strongly related to salinity than temperature in cold regions such as the Arctic (Aagaard et al., 1981). It is made up of water that originates from winter convection of relatively high saline water from Fram Strait entering to the north of Barents Sea and the Barents Sea Branch, which then circulates around the Eurasian Basin (Rudels et al., 2004, Rudels et al., 1996).

The Atlantic Water is a layer of warm water that is a major source of heat that enters the Arctic Ocean at the surface from the Atlantic Ocean, where it then cools and sinks to form dense water. If all the heat available were accessible to the surface, there would be sufficient heat to melt all the sea ice in the Arctic in a few years (Turner 2010). The halocline that exists between the deeper intermediate layer Atlantic Water and the surface mixed layer inhibits the upward release of the Atlantic water heat. The progression in model development has allowed for the creation of increasingly high resolution models of the ocean, which is useful for the ability to better resolve small scale features in the ocean that have a small Rossby radius of deformation, such as eddies. Eddies are present in the Canada Basin halocline and could be a

method of mixing the underlying Atlantic water with the surface mixed layer (Timmermans et al., 2008).

The heat flux could influence the sea ice via an albedo-feedback mechanism that may lead to an increase in ice retreat. This would be most evident in the Barents Sea, a region of ice formation and also dense water as a result of cooling (Årthun et al., 2012). This could relate to the behaviour of the Atlantic Water layer, as the reduction has coincided with a strengthening of the Atlantic inflow. There has also been a retreat in the Arctic halocline, as the warm Atlantic Water penetrated further into the Arctic Ocean (Steele and Boyd 1998), though the halocline has started to return towards the Fram Strait (Boyd et al., 2002) so this is not a persistent feature.

There have been a small number of attempts to assess the entire energy budget of the northern polar region, such as Nakamura and Oort (1988) Overland and Turet (1994), and Serreze et al. (2007). These have contrasting regions as there is no consistent definition of the Arctic Ocean used in studies but Serreze et al. analysed the period 1979-2001 and obtained a summer energy gain of 100 Wm^{-2} and a winter energy loss of 175-180 Wm^{-2}. The Barents Sea has been studied by Smedsrud et al. (2010), and shows that about 70 TW of heat is lost through latent, sensible and long wave radiation.

Arctic warming has reduced the polar cap, and Atlantic Water is believed to be a factor (Polyakov et al., 2010). Observations show a decrease in sea ice extent in the summer minimum over the last 30 years (Stroeve et al., 2011) and in sea ice thickness over the last 15 years (Kwok and Rothrock, 2009). Therefore, changes in the Atlantic Water distributions and its modification and loss are of vital interest for our understanding of the climate.

Current observational studies of the freshwater budget generally only cover part of the Arctic Ocean or have a limited observation period or use sparse data (Rabe et al., 2014). Obtaining an understanding of the whole Arctic Ocean freshwater system is relevant though as it is a major part of the climate system (Tartinville et al., 2001, Webster, 1994). There is 74,000 km^3 of freshwater in the Arctic Ocean's upper layer, separated by the halocline from the warmer, higher salinity water below it (Serreze et al., 2006). The dominant source of this is river run-off (38%), followed by Bering Strait inflow (30%) and precipitation (24%). 11% of the world's river runoff directly enters the Arctic Ocean (Fichot et al., 2013). The content has increased in recent decades with a link being made to the wind circulation of the Arctic causing convergence in the Beaufort Gyre which has increased the freshwater storage by an estimated 8000 km^3. A reversal of this cycle could release this water into the rest of the Arctic Ocean (Giles et al., 2012). The export of freshwater from the Arctic may modulate the large-scale ocean overturning circulation by causing density fluctuations that affect the convection strength (Jungclaus et al., 2005). The freshwater budget has an impact on the density stratification of the Arctic Ocean and the formation of sea ice (Aagaard and Carmack, 1989). The reduction of sea ice and the increase in liquid freshwater alters the sea surface topography and can change the flow of geostrophic currents (McPhee et al, 2009). The potential consequences include an acceleration of the global water cycle and an increase in river runoff from a warming temperature (Dickson et al., 2007). A link has also been made to decreasing sea ice coverage and 'Arctic Amplification', the rise in near surface air temperature being much greater in the Arctic than the global average (Screen and Simmonds, 2010). Rudels (2010) suggests that an increase in sea ice melt may eventually limit the effect of warming as the increased freshwater would increase the stratification

and reduce the effects of warmer Atlantic water in the Arctic Ocean, especially since much of the heat is lost to the atmosphere. This suggests that the effect of Atlantic Water on sea ice melt would not be as significant as the direct potential from the stored reservoir of heat in the ocean.

This project will use recent NEMO runs to extend the period studied in the previous research to 2007, which is as far as these model runs reached, and investigate the seasonal cycle as well as the average net fluxes of heat and freshwater storage. It will also investigate sub-regional heat loss of individual seas within the whole Arctic Ocean region and the significance of this and the effects of using different climatologies and resolutions. To put these regions into context, the next chapter presents an overview of the Arctic Ocean geography.

Chapter 2: Overview

This chapter presents an overview of the Arctic Ocean to describe the region investigated in this project and the fundamental features of it that govern its behaviour. The Arctic Ocean is described as 'Mediterranean' in that it is a body of water that is almost entirely enclosed by land and only has contact with the rest of the global ocean by relatively narrow passages. Within the Arctic Ocean are shelf seas on the coast and deeper central basins, dotted by ridges on the sea floor.

2.1 Geography of the Arctic Ocean

It is necessary to understand the geography of the Arctic Ocean to be able to investigate its physical properties. We examine the region being considered in the project, how the overall circulation of the Arctic Ocean operates, and the ocean gateways that contribute volume, heat and salinity through boundary fluxes.

2.1.1 Definition of Arctic Ocean

The Arctic Ocean geographical boundaries are defined by the International Hydrographic Organisation. The Arctic Ocean consists of central ocean basins and marginal seas by the coast and islands on the periphery of the basins; these are shelf seas where the water meets the continental shelf and is shallow. The four principal central oceanic basins are separated by the oceanic ridges in the following order (Figure 2.1): The Nansen and Amundsen Basins are separated by the Gakkel Ridge, the Amundsen and Makarov basins by the

Lomonosov Ridge, and the Makarov and Canada basins by the Alpha-Mendeleev Ridge. The Nansen and Amundsen basins constitute the Eurasian Basin, whereas the Makarov and Canada Basins constitute the Canadian Basin. The Arctic shelf seas are the Barents, Kara, Laptev Seas, East Siberian and Chukchi Sea, and the margins are at the Canadian Arctic Archipelago (CAA), Lincoln Sea, and Baffin Bay. The five passages, Fram Strait, the Barents Sea Opening (BSO), Fury and Hecla Strait and Davis Strait on the Atlantic side, and the Bering Strait on the Pacific side, connect the Arctic Ocean and Arctic seas to the global ocean (eg. Tsubouchi et al,. (2012)). For the regions, see Figure 2.1. This is broadly similar to the regions used by Serreze et al. (2007) except this definition includes Baffin Bay. Serreze et al. wanted to focus on the polar cap, but Baffin Bay contains water that is readily identifiable as Arctic Water that is in transition to being exported to the Atlantic Ocean.

The straits are relatively shallow – the BSO is 500 m deep (O'Dwyer et al., 2001), except for the Fram Strait, which has a sill at ca. 2500 m (Thiede et al, 1990). Therefore, the latter is the only passage where the deep water exchange between the Arctic and the Nordic Seas is possible. However, deep water flow between the Nordic Seas and the North Atlantic is restricted by the Greenland-Scotland Ridge (sill depth of 840 m in the Faroe-Bank channel, Hansen and Østerhus, 2000), keeping the deep Arctic Ocean isolated from the global ocean. Hence the Arctic is sometimes referred to as the 'Arctic Mediterranean'. In this study, the Arctic excludes the Hudson Bay and Hudson Strait, the regions chosen to be consistent with the results by Tsubouchi et al. (2012), which built upon previous studies and used mooring stations as the boundaries.

2.1.2 Water masses

The Arctic Ocean is characterised by strong stratification of water masses in the top 200–300 m and weak stratification of the water below this depth. The vertical structure of the Arctic water masses is broadly divided into the mixed layer (ca. top 50 m of the water column), halocline (ca. 50–300 m), intermediate waters (ca. 300–1500 m) and deep waters (>1500 m) (Aagaard et al., 1981) (Figure 2.2). Rudels (1989) distinguishes the different water masses within these layers, introducing the modes of intermediate water which include the warm and saline (S >35, T >0°C) Atlantic water, which is in contrast to the overlaying cold, fresh surface layer. This Atlantic water is the major source of heat advection into the Arctic Ocean. Further around the Arctic Ocean, where Pacific water also enters the Arctic Ocean through the Bering Strait, Smethie (2000) describes upper halocline water as modified water from the Pacific (S = 33.2), found on the Chukchi, East Siberian and Laptev shelves. Lower halocline water (S = 34.2) is Atlantic water modified by the river runoff and sea ice melt north of the Barents Sea to become the Barents Sea Branch Water. This forms water masses that are advective in origin but are distinct from each other, enabling the circulation of the Atlantic-origin water to still be identifiable. The two different water masses produces a varying halocline in the Canada Basin unlike that in the Eurasian Basin, in that there are some regions with a greater temperature due to the circumpolar Barents Sea Branch Water (Rudels et al., 2004), but also some regions with a lower temperature due to Pacific Water inflow (Salmon and McRoy, 1994).

The temperature of the Arctic surface water layer is close to freezing down to the thermocline. The water is close to the freezing point of seawater and there is little temperature variation, so the α-coefficient in the salinity term dominates over the β-coefficient in the temperature term in the equation of

state for seawater (Millero 1980), and the density of Arctic Ocean is dependent on salinity at low temperatures (Aagaard et al., 1981) (Figure 2.3). Thus a small modification of the freshwater content has a significant impact on the convective processes can that take place (Aagaard and Carmack 1989) as the halocline can be weakened or strengthened. The halocline inhibits convection from below to limit the transfer of heat from the Atlantic Water to the surface, and therefore the ice too (Timmermans et al., 2008). However, an alternative view is that Atlantic Water heat has been responsible for thinning of the sea ice and contributing to its retreat over the last few decades (Polyakov et al., 2010). Sea ice is discussed further in Section 2.2.

2.1.3 Circulation

The overall Arctic Ocean circulation consists of four constituent parts. In the ocean basin sub-region there are separate circulation patterns at the surface and the deeper interior. There are also boundary currents in the shelf seas that circulate around the basins, and there are exchanges between the Arctic Ocean and the neighbouring Atlantic and Pacific oceans.

There are two different modes of atmospheric circulation that provide the wind forcing that contributes to the ocean circulation, an anticyclonic system in the Beaufort Sea and a cyclonic system over the Eurasian Basin (Gudkovich 1961, Proshutinsky and Johnson, 1997). The two systems fluctuate over how much of the Arctic they cover and the extent of the coverage of each system is known to oscillate on a decadal timescale. The surface layer of the ocean (0-200 m) circulates anti-cyclonically in the Canadian Basin, while in the Eurasian Basin the surface layer circulates cyclonically (Figure 2.4). The spatial extent of these circulations is related to the Arctic Oscillation (AO) (Polyakov and Johnson, 2000), an index of atmospheric pressure above the Arctic that

fluctuates between a positive and negative mode over seasonal, annual and decadal timescales (Thompson and Wallace, 1998). Positive AO is when the cyclonic circulation is more dominant, creating low pressure at the North Pole and bringing Atlantic Water closer to the sea surface. The AO could influence ice circulation and the temperature and salinity structure of the ocean, including the Atlantic Water (Proshutinsky and Johnson, 1997). The Atlantic Water is shown in a tracer model experiment to extend further around the Arctic towards the Canadian Basin during a positive AO index (Maslowski et al., 2000) as the wind forcing is acting in the same direction as the ocean circulation, which could be important for the transport of heat as the inflow of warm Atlantic Water is either suppressed or accelerated. The Transpolar Drift (TPD), a flow of sea ice and surface-subsurface water, is driven by the interaction of the two surface atmospheric forcings at their boundary with each other. The TPD flows from the Siberian coast, across the North Pole and into the North Atlantic through Fram Strait (Serreze et al., 2007). This is shown on Figure 2.5 with the other circulation patterns.

Below the surface, the interior circulation has four cyclonic gyres (Figure 2.5), controlled by the topography of the ridges, the Coriolis force, friction from the wind driven circulation above, and geostrophic flow. The anticyclonic surface circulation in the Canada Basin creates a shear that opposes the interior cyclonic circulation.

The Atlantic Layer water (200-800 m depth) circulates around the Arctic Ocean by the circumpolar boundary current, which consists of inflow of the Fram Strait Branch (FSB), the Barents Sea Branch (BSB) (Rudels et al., 1994), and the Arctic Shelf Break Branch (ASBB) (Aksenov et al., 2011). The FSB enters through Fram Strait, and the BSB and ASBB enters through the St. Anna Trough. The boundary current flows cyclonically along the Siberian continental slope, and

the warmer part of the FSB is then diverted north to flow along the Lomonosov Ridge to return and exit through Fram Strait. The colder part joins the BSB to flow into the Canadian Basin. Part of this combined Atlantic Water is presumed to then follow the topography of the Mendeleev Ridge to exit through Fram Strait, while the rest of the current continues to form a circuit around the Canadian coastline before leaving through the CAA and Fram Strait (Rudels et al., 2000). The Barents Sea cyclonic circulation may be due to buoyancy forcing rather than wind fluxes, which are more responsible for the circulation in the Amerasian basin side of the Arctic Ocean (Karcher et al., 2007).

2.1.4 Inflow/Outflow

The Arctic Ocean is a large store of liquid freshwater (74,000 km^3) and an additional annual average of 10,000 km^3 of sea ice. The store is large due to a large amount of low salinity water inflow (Serreze et al., 2006).

Surface fluxes of river runoff, precipitation and ice melt are sources that lower the salinity of the ocean, while evaporation and sea ice formation are sinks that increase the salinity. These sources and sinks modify imports and exports transported through the straits. Inflow is through the West Spitzbergen Current through the eastern Fram Strait, the BSO (Schauer et al., 2002), and the Bering Strait, while exports are through the CAA and the East Greenland Current which is through the western Fram Strait, (Dickson et al., 2007). With the definition of the Arctic Ocean used in this report, the transport through the CAA leaves the Arctic Ocean through Davis Strait and Fury/Hecla Straits.

The Bering Strait inflows to the Arctic due to a mean sea level slope (Overland and Roach, 1987) and wind forcing (Woodgate et al. 2012), and is an important

source of low salinity water despite being only ca. 50 m deep and ca. 80 km wide.

The layers of water masses in the ocean are modified partly by interior mixing from double diffusive processes (Lenn et al., 2009), and surface fluxes. The Arctic transforms low density Atlantic water into an export of high density intermediate and deep waters, but also exports surface water that is of lower salinity and density (Meincke et al., 1997).

For surface fluxes, there are nine main rivers that flow into the Arctic Ocean. Of these, the four major rivers are the Ob, Yenesey and Lena in Russia, and the Mackenzie River in Canada, while the Kolyma, Severnaya Dvina, Khatanga and Pechora, in Russia, and the Yukon in Canada have smaller contributions (Peterson et al., 2002). River discharge rates are seasonal, with winter flow being a tenth of that in June (Yang et al., 2014), but the nine rivers add to 3300 km^3yr^{-1}. This is considerable – the Arctic Ocean contains only ca. 1% of the world's ocean volume (Menard and Smith, 1966), but ca. 10% of the world's river runoff flows into the Arctic Ocean. The river influx mainly constitutes the water from their drainage basins, but there is also a small amount of groundwater and glacial melt that contributes 1% to the freshwater budget of the Arctic Ocean (Lewis and Jones, 2000).

River discharge is the greatest contributor to the Arctic freshwater flux, that which can be considered to be added through the surface of the ocean, (ca. 60%, Dickson et al., 2007); direct precipitation from rain and snow adds ca. 40% of the input. The precipitation constitutes 24% of the total freshwater input, when including the advective boundary flux transported from other oceans (Serreze et al., 2006).

In the shelf seas, as the water freezes, freshwater is taken out of the ocean by forming ice, increasing the salinity of the water. The reverse happens when the ice melts; the fresh water is added to the ocean.

2.2 Sea ice

The Arctic Ocean is significantly covered by sea ice. In September, when the ice is at a minimum due to the preceding months of melting, the sea ice has an estimated area of ~4 x 10^6 km^2. (Serreze et al., 2003). The estimate is based from satellite imagery on the extent to which the region has greater than 15% sea ice and the weighting value of the ice concentration, as the given region is not entirely covered by sea ice. The winter drop in temperature freezes the surface of the ocean, so that by February much of the Arctic Ocean is covered in sea ice, except for the Barents Sea (Figure 2.6). Ice is predominantly exported through Fram Strait, with 10% of the ice in the Arctic Ocean travelling to the Atlantic Ocean each year (Langehaug et al., 2006). In the centre of the Arctic, the ice can have a residence time of 4-5 years as it neither freezes nor melts and remains fairly stationary.

Sea ice is important for the climate and ocean circulation of the Northern Hemisphere, as its variability has implications for heating and the freshwater content of the Arctic Ocean. Ice (and snow which may fall on the ice) has a high albedo, meaning that a lot of the incoming solar radiation is reflected back and not absorbed to heat the ice and the ocean below it. The ice and snow albedo is 60%, while the ocean's albedo is only 10% (Hartmann, 1994). This creates a positive feedback mechanism in that a reduction of ice cover decreases the albedo, which increases the amount of radiation being absorbed, which in turn further reduces the ice cover. The reverse is also possible to

create a cooling feedback. Exposed areas that are uncovered by ice are also able to radiate heat and cool the surface of the ocean.

The sea ice is also a store of freshwater, and the formation of it increases the salinity of the surface of the ocean via a process called brine rejection, where salt is excluded from the ice crystals (Ruddimann 2001). The formation of sea ice along with cooling increases the density of the surface water, causing it to sink, particularly along ocean shelf seas, and create deep water. The deep water circulation is a major part of the overall global circulation of the ocean, taking in warm water from the Atlantic Ocean and exporting it as cooler water.

The major concern about an excessive reduction in the sea ice coverage due to melting is that this would increase the density stratification and inhibit the formation of deep water. The suggestion is that the Arctic Ocean may eventually become ice-free in the summer in the long-term future based on current trends, though as previously stated by Turner (2010) there is already enough heat content to melt all the ice. There have been several studies about Arctic sea ice decline and trends in the minimum summer sea ice coverage, such as Holland et al. (2006), Stroeve et al. (2007), and Wang and Overland (2009).

The Arctic Ocean is a complex region with importance for the wider world. It has multiple ocean and atmospheric circulation regimes and is an area which is unique for being salinity-dependent for density variations. Warm, salty water is imported from the Atlantic Ocean through the eastern part of the Fram Strait and the Barents Sea Opening and with the formation and melting of sea ice and radiative heat transfer, cold, fresh water is exported through Davis Strait and the western part of Fram Strait. Understanding the behaviour of this is valuable towards our understanding of the Arctic Ocean and the long-term

future of the global ocean circulation. In order to achieve this effectively, it is necessary to use modelling techniques. These techniques are introduced in the next chapter.

2.3 Figures

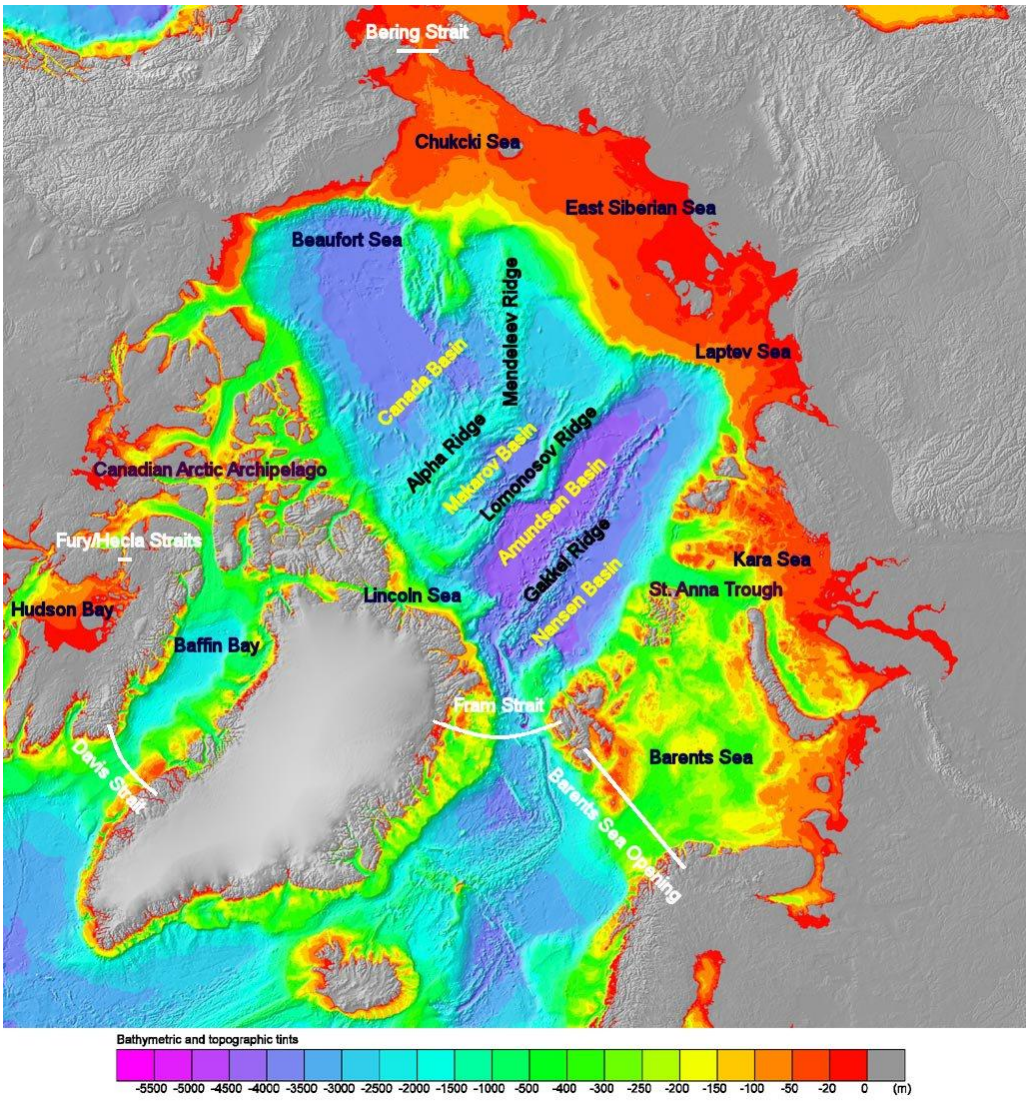

Figure 2.1 – Bathymetric map of the Arctic Ocean with key geographical features highlighted. White lines are straits between the Arctic Ocean and the rest of the global ocean. Blue text features are the marginal seas of the Arctic Ocean. Black text features are underwater ridges; yellow text features are ocean basins separated by the underwater ridges. The Amundsen and Nansen Basins are collectively the Eurasian Basin; the Canada and Makarov Basins form the Canadian Basin. Purple features are other important locations mentioned in the project. Adapted from Ahlenius (2008) and Jakobsson et al. (2012).

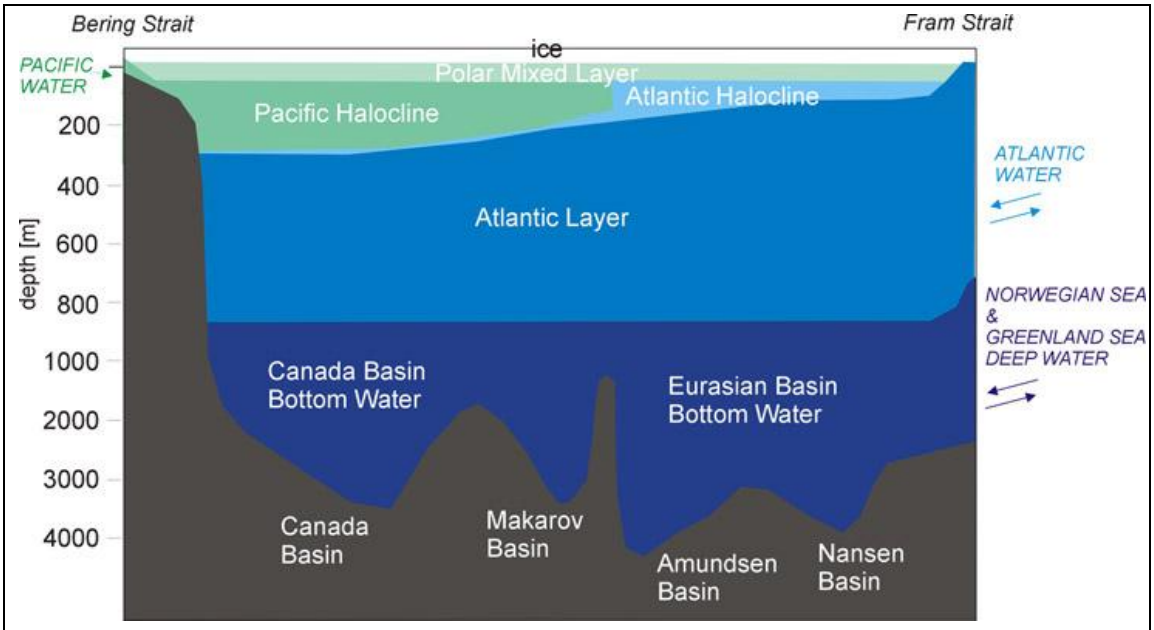

Figure 2.2 – Schematic diagram of the stratification of water masses in the Arctic Ocean, as viewed from Greenland towards the north. The mixed layer is the uppermost layer at the boundary between the ocean and the ocean surface. Below this is the halocline, formed by brine rejection from ice formation. There are two different types of halocline – Atlantic origin and Pacific origin from the Bering Strait. The ocean circulation takes the water to the east of Bering Strait, so Pacific Halocline is only found on the Canadian Basin side of the Arctic Ocean. Below the halocline are intermediate waters including the warm, salty Atlantic Layer, and below that is deep bottom water, produced by the cooling of dense water at the shelf seas sinking down.

At the Fram Strait, Atlantic Water enters the Arctic Ocean at the surface, before it follows topography and sinks downwards. Adapted from MacDonald et al. (1996).

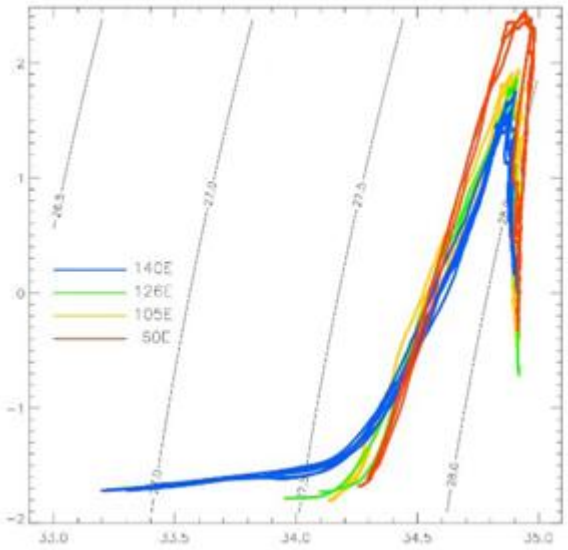

Figure 2.3 – T-S diagram of the Arctic Ocean. The different colours represent different cross sections of the ocean in a 2009 study. The contours are almost parallel to the plot except for at low salinities (<34.3 psu), showing that there is a high dependence on salinity for the density of the seawater. Higher temperatures are found at low salinities in the east of the Arctic (blue line), suggesting the upward transfer of heat from Atlantic Water in this area.

Taken from Polyakov, I, www.iarc.uaf.edu/JAMSTEC/research/monitoring-arctic-ocean-climate.

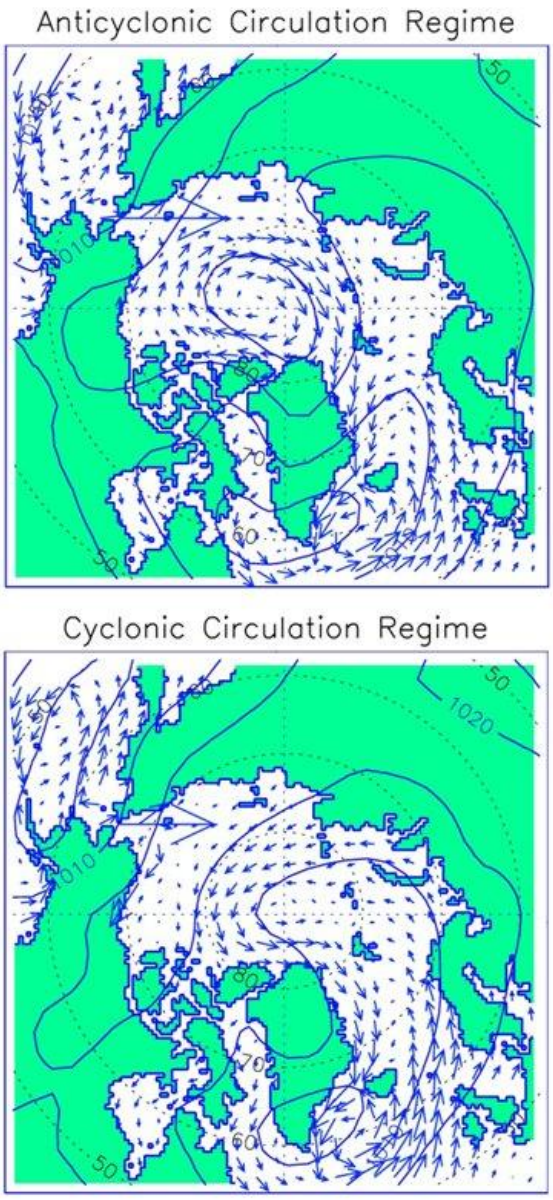

Figure 2.4 – The two atmospheric circulation modes in the Arctic that produce the Arctic Oscillation. Top: the anticyclonic (negative) regime over the Canadian Basin dominates, extending into the Eurasian Basin. Bottom: The cyclonic (positive) regime over the Eurasian Basin dominates, extending into the Canadian basin. The wind circulation has an effect on the ocean circulation, depending on whether they act in the same direction (bottom) or oppose each other (top), influencing the course and intrusion of the Atlantic inflow. Taken from Proshutinsky and Johnson (1997).

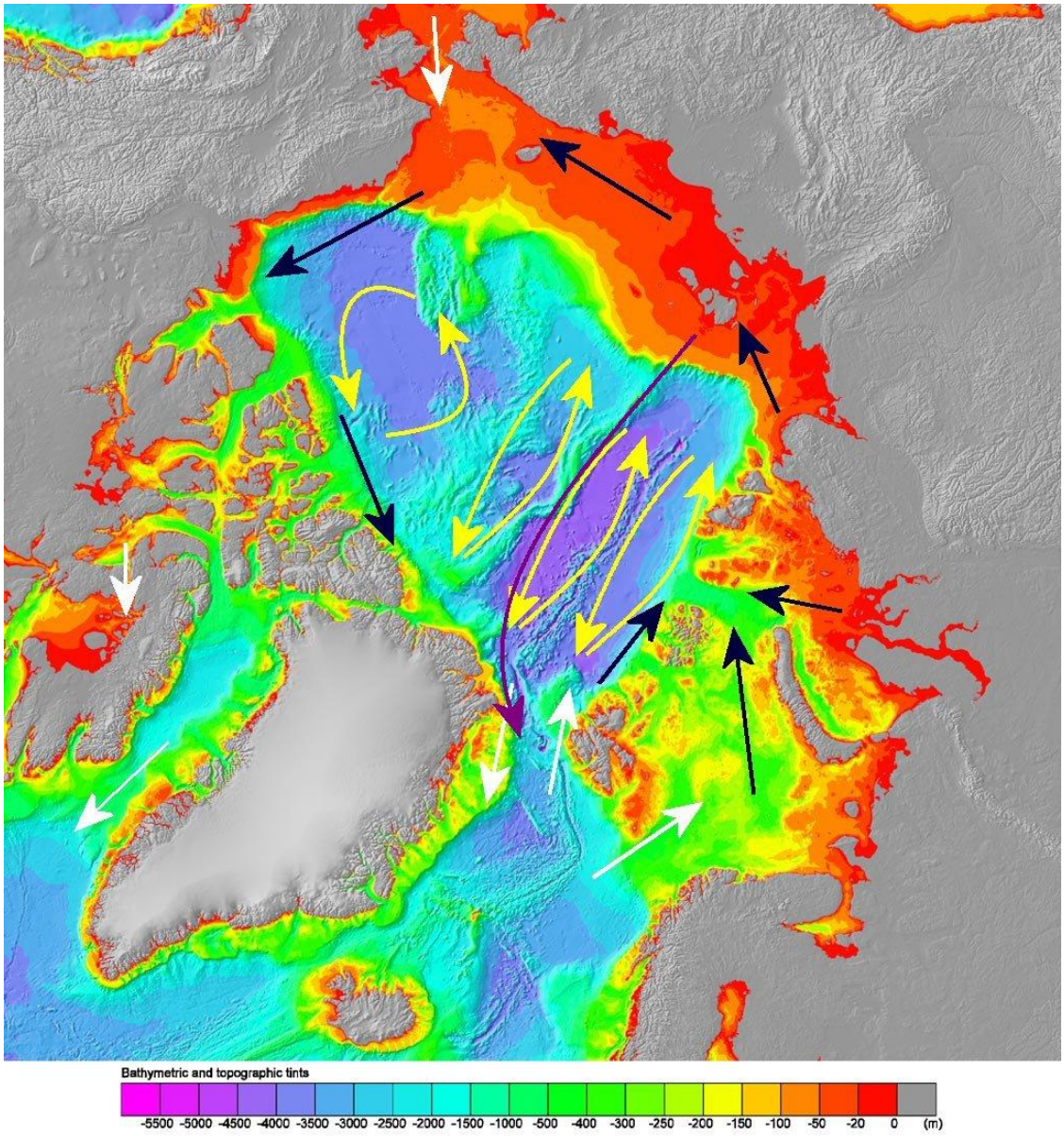

Figure 2.5 – Bathymetry map of the Arctic Ocean showing ocean circulation patterns. White arrows represent the exchanges between the Arctic Ocean and the rest of the global ocean. Blue arrows represent the boundary current, including the Fram Strait Branch and Barents Sea Branch along the shelf seas. Yellow arrows represent the interior circulation, constrained by topography. The purple arrow is the Transpolar Drift, a surface circulation feature that is a response to the atmospheric circulation regimes. Adapted from Jones (2001) and Jakobsson et al. (2012).

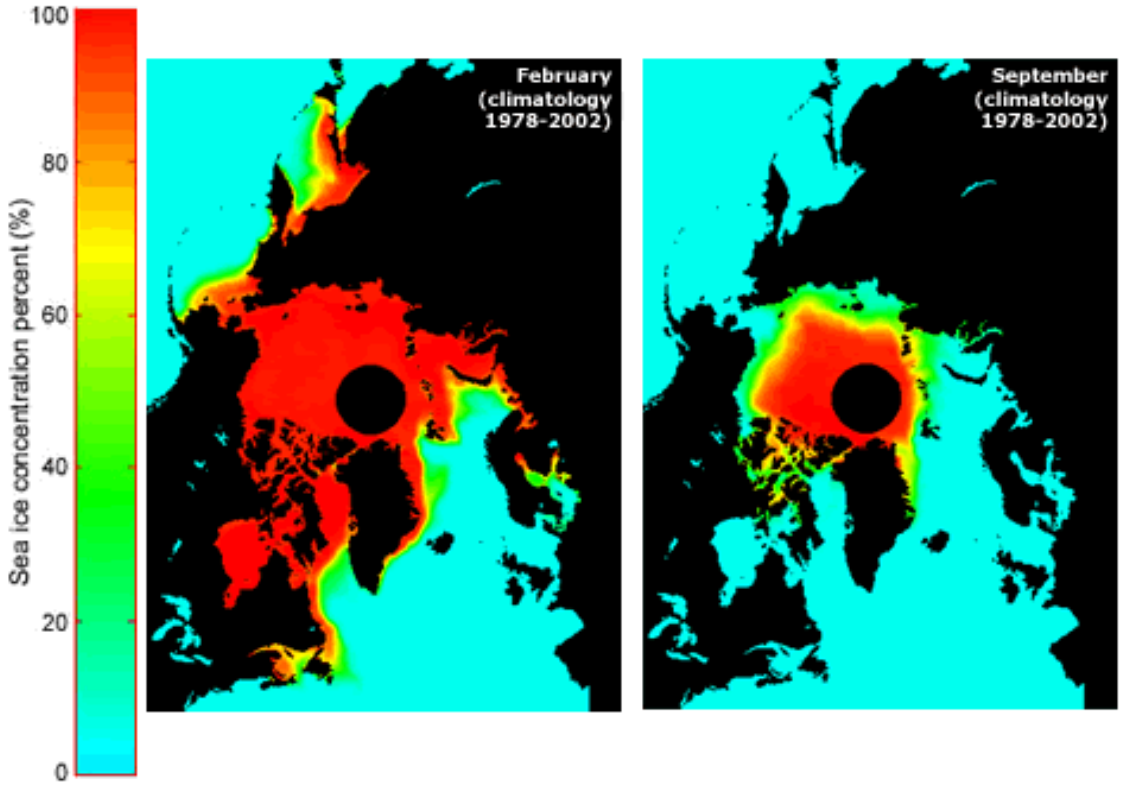

Figure 2.6 – Map of the Arctic Ocean showing differences in February and September sea ice concentrations, averaged from 1978–2002 satellite data, representing winter and summer seasonal maximum and minimum levels respectively. In February, the entire ocean is ice-covered, except for in the Barents Sea, while in September all the shelf seas have reduced ice coverage, with concentrations below 60%, while the high arctic still has 100% ice concentration. Image taken from National Snow and Ice Data Center, University of Colorado.

Chapter 3: **Modelling**

This section describes the model used in the project and the key properties of the configurations of the model runs.

3.1 NEMO OCGM

General Circulation Models (GCMs) are used for studying the Earth's climate. They solve the primitive Navier-Stokes equations of fluid motion for the rotating Earth along with an equation of state.

Ocean General Circulation Models (OGCMs) specifically model the world's oceans, and can be coupled to other models, such as sea ice or the atmosphere. The NEMO (Nucleus for European Modelling of the Ocean) framework is a widely used Boussinesq hydrostatic sea ice-ocean GCM that is used at the National Oceanography Centre (NOC). It uses the OPA (Océan PArallélisé) primitive equation model for ocean dynamics and thermodynamics and LIM (Louvain-la-Neuve Ice Model) for sea-ice dynamics and thermodynamics (Madec et al., 1998). The primitive equations are a set of nonlinear differential equations used to calculate atmospheric and oceanic flows.

The set of equations that are solved by NEMO cover momentum balance (equation 3.1), hydrostatic equilibrium (equation 3.2), incompressibility (equation 3.3), heat and salt conservation (equations 3.4 and 3.5), and an equation of state in a set of orthogonal unit vectors i,j and k (equation 3.6). In large-scale motions, gravitational force is dominant so k is the local upward vector and i and j are tangent to geopotential surfaces. By defining U as the

vector velocity, $U = U_h + \omega$k (subscript h denoting the horizontal plane), T as potential temperature, S as salinity, ρ is in situ density, the equations are as follows:

$$\frac{\partial U_h}{\partial t} = -\left[(\nabla \times U) \times U + \frac{1}{2}\nabla(U^2)\right]_h - fk \times U_h - \frac{1}{\rho_0}\nabla_h p + D^U + F^U \quad (3.1)$$

$$\frac{\partial p}{\partial z} = -\rho g \quad (3.2)$$

$$\nabla . U = 0 \quad (3.3)$$

$$\frac{\partial T}{\partial t} = -\nabla . (TU) + D^T + F^T \quad (3.4)$$

$$\frac{\partial S}{\partial t} = -\nabla . (SU) + D^S + F^S \quad (3.5)$$

$$\rho = \rho(T, S, p) \quad (3.6)$$

∇ is the vector operator in (i,j,k) directions, t is time, z is the vertical coordinate, ρ is density given by the equation of state (3.6), ρ_0 is a reference density, f is the Coriolis parameter, g is gravitational acceleration. The terms D^T, D^S, D^U represent the parameterisation of small scale mixing physics for temperature, salinity and momentum respectively and F^T, F^S, F^U are the equivalent for surface forcing terms, for example from winds.

Being Boussinesq means that there is a constant reference density of the ocean as the differences in density in the ocean are negligible. The only consideration for density differences is when calculating in-situ buoyancy effects from an equation of state as gravity is strong enough to make a difference in weight noticeable. Examples of these buoyancy effects are pressure gradient force, vertically averaged density and stratification, and defining neutral surfaces for along-isopycnal mixing (Shchepetkin and

McWilliams, 2011). The model mathematically conserves volume; multiplying the conserved volume by the constant density produces the Boussinesq mass, which is conserved. Mass conservation in the model is vital for the conservation of tracer quantities (see Chapter 4.1). The model also follows hydrostatic equilibrium, which reduces vertical momentum to a balance between the buoyancy forcing and pressure gradients by removing convective processes from the initial Navier-Stokes equations. Convection of momentum is instead parameterised. Incompressibility means that the density of a moving fluid remains constant, which is equivalent to having a zero three dimensional divergence of the velocity vector.

The NEMO model runs in a grid of a variety of horizontal resolutions from 2° to 1/12° and in different vertical resolutions, from 36 to 75 depth levels. The bathymetry is built from interpolation on to the mesh grid of a global elevation product such as ETOPO2 (Earth Topography Digital Data Set), which features data from IBCAO (International Bathymetric Chart of the Arctic Ocean) north of 64°N. The models are able to resolve the advection of physical quantities such as momentum, and tracers such as temperature and salinity. At the 1/12° resolution, some mesoscale eddies are resolvable where they are at a greater scale than the grid cells, such as at high latitudes in the Arctic where the Rossby radius is only 5-15 km (Nurser and Bacon, 2013), while the 1/4° resolution is too coarse for this. In the Arctic Ocean shelf seas the Rossby radius is smaller, so the 1/12° model is also not eddy resolving here. In the 1/4° and 1/12° models, eddy velocities are not featured in the calculations and are instead parameterised as part of a lateral diffusion process.

There are different ways to model the vertical grid. Some models use depth (z-grid) or density (isopycnic coordinates) as the vertical coordinate; others follow seabed topography (s-grid). The NEMO runs use a z-coordinate based

vertical scale that is divided into layers of grid cells that are not of equal depth, increasing from 1 m at the surface to 200 m at depth (Figure 3.1) to create a finer resolution in the upper ocean than the deep ocean. This is chosen because there are greater vertical density gradients in the upper ocean but as a greater number of layers increases the number of cells that the model has to process, reducing the deeper detail minimises the limitations of computing power to run the model efficiently.

The ocean is bounded by coastlines, bottom topography and an air-sea interface at the top. These can be modelled in different ways to varying levels of complexity in order to create a better representation of reality and the physical processes that this enables. The air-ocean interface describing the change in sea surface height (SSH) is considered to be a free surface (Campin et al., 2004). A free surface is one in which there is zero force in a perpendicular direction to the surface, and there is no shear stress component, and in this sense means the pressure on the ocean surface is equal to the atmospheric pressure. The change in sea surface height η over time t depends on the input of precipitation P and evaporation E and the advection of water given by A, which is the divergence composed of the total height of the water column and its mean horizontal velocity $\overline{U}_h$.

$$\frac{d\eta}{dt} = -A + P - E \,, where\ A = \nabla[(H + \eta)\,\overline{U}_h] \tag{3.7}$$

The free surface equation can either be solved nonlinearly or linearly. The nonlinear formulation of the free surface allows the volume of the model to vary over time; these adapted z- and s- grids are known as the z* grid and s* grid respectively and have all the cells in the column change thickness proportionately to the total SSH at each point in time. This project features

model run configurations that use the z- or z* grid depending on whether they have linear or nonlinear free surfaces.

In the model linear free surface, the variations in SSH are entirely manifested at the surface, while all the cells at depth maintain constant thickness. The non-linear version enables perfect conservation of freshwater and heat, while this is not the case in the linear version due to the products of averages (Roullet and Madec, 2000) that create an extra unknown term in the equation. The linear approximation is made by assuming that the SSH is small relative to the total depth of the column (Levier et al., 2007) and ignoring the interaction of high frequency waves with the baroclinic structure of the ocean. This allows a larger timestep to be used which does not need to represent fast external gravity waves.

The accuracy of the model grids used in this project is improved by the optional implementation of partial bottom cells, in which the thickness of the bottom ocean cell is variable to better fit the topography, rather than approximating by having the full cell at the closest matching depth. The use of partial steps has been shown to have an important contribution to the model performance, especially in regions with strong current-topography interactions (Penduff et al., 2005, Barnier et al., 2006). Heat and salinity fluxes between the sea floor and the ocean are negligible and are generally ignored.

NEMO has a tri-polar horizontal grid, with two northern hemisphere poles situated in Canada and Siberia to avoid the computational problems of having a singularity in the ocean, while the third model pole is at the Geographical South Pole, which is already overland. The model grid coincides with the geographical latitude and longitude grid south of 56° N. The use of a tripolar grid results in a singularity line between the two model North Poles, termed

'The North Fold' (Murray 1996). When the spherical tri-polar model grid is mapped onto the indexed model array, a boundary condition is required to ensure continuity of the model field across the singularity line, as well as a cyclic boundary condition on the 180° meridian line. This means that the Arctic Ocean is split into two separate regions in both the indexed model arrays and the output field, with the overlapping of a number of lines of cells either side of the boundary. This overlap must be accounted for when analysing the region to avoid the double counting of cells.

The spherical coordinates are mapped on to a 3-D mesh of model cells in order to numerically solve the model equations. The mesh is defined by a transformation that gives the spherical coordinates of latitude, longitude and depth as a function of (i,j,k) grid index arrays (Figure 3.2). The half (i,j,k) values are at the cell faces, which is important for defining the locations of the grid of different variables that maps on to this mesh.

NEMO uses an Arakawa C-grid (Arakawa and Lamb, 1977) In this grid, each cell is face-centred in curvilinear (i,j,k) space, with the scalar variables such as ocean temperature and salinity, sea ice thickness and fraction, sea surface height and surface fluxes placed in the geometrical centre of the cell (T-point), while the velocity vector components are at the centre of the faces of the cell, at u-, v- and w- points (Figure 3.3). The product of a scalar field and a vector field is calculated by interpolating the vector field as T-points. The dimensions of a grid cell are known as the scaling factors, with e_1 and e_2 representing the horizontal and e_3 the vertical lengths. These lengths are defined according to spherical geometry as follows (Figure 3.4)

$$e_1 = (r + z)\left[\left(\frac{\partial\lambda}{\partial i}\cos\varphi\right)^2 + \left(\frac{\partial\varphi}{\partial i}\right)^2\right]^{\frac{1}{2}} \tag{3.8}$$

$$e_2 = (r + z)\left[\left(\frac{\partial \lambda}{\partial j}\cos\varphi\right)^2 + \left(\frac{\partial \varphi}{\partial j}\right)^2\right]^{\frac{1}{2}} \quad (3.9)$$

$$e_3 = \left(\frac{\partial z}{\partial k}\right) \quad (3.10)$$

φ is the longitude, λ is the latitude, r is Earth's radius and z is the altitude above a reference sea level.

OGCMs need surface fluxes of heat, freshwater and momentum from wind stress as surface boundary conditions (Brodeau et al., 2010). The influence of the atmospheric conditions on the ocean is parameterised in NEMO as a forcing field. Different reanalyses are available for describing the climate, though their validity is limited by the lack of observations in the Arctic. There are three model atmospheric forcings used in this project: CORE II (COoRdinate Ocean Experiment, phase II), ERA-Interim and DFS4 (Drakkar Forcing Set).

CORE II is from the National Centers for Enviromental Prediction (NCEP) (Large and Yeager, 2009) and incorporates several datasets from various satellite and buoy data sources such as POLES (Rigor et al., 2000) to compute a complete set of atmospheric fluxes that produce a near-zero global heat flux balance. Compared to previous models like ERA40, this gives precipitation and radiation without depending directly on clouds, the data of which is not necessarily reliable, and provides interannual variability.

ERA-Interim reanalysis forcing is from the European Centre for Medium Range Weather Forecasts (ECMWF) (Dee et al., 2011) and is designed to replace their ERA40 model. It runs from 1989 onwards and improves upon the assimilation of satellite data to produce better temporal consistency and a better representation of the hydrological cycle.

DFS4 is designed as an improvement over the ERA-40-based data and uses a combination of CORE, ECMWF data and observed flux data (Brodeau et al. 2010). It adds corrections of surface temperature and humidity, wind, radiation and precipitation to improve the global heat and freshwater budget. It improves upon a ERA40 warm bias in the Arctic by using satellite data to form a sea-ice mask and apply a -1°C offset to air temperature over water north of 70°N and an average of two different models, POLES and ERA40 over sea-ice covered regions. Damping (the application of which is described in section 4.2.2) is applied as a restoring surface salinity from the climatology of Levitus (1988) to correct for model drift due to precipitation and the ocean model not interacting with the atmosphere model.

NEMO has a so-called restoring factor for freshwater, but not temperature. Over time, a freshwater flux correction is added at the surface based on an observed, climatological or atmospheric model product, to respond to model drift from imbalances in evaporation and precipitation. Although it is a freshwater flux, the volume of water does not change and the input is treated as a virtual salinity flux at the surface. There is no corresponding physical process that produces a surface salinity flux, but it improves the freshwater balance in the model (Madec and Delecluse, 1997, Madec 2008). This flux is of the order of 10^{-5} kg m^{-2} s^{-1}.

3.2 Sea ice

Sea ice impacts on both the temperature and salinity of the Arctic Ocean. NEMO uses LIM2-EVP for modelling sea ice. This uses elastic-viscous-plastic (EVP) rheology, Semtner thermodynamics and single category sea ice.

The EVP rheology is a method for describing the physical behaviour of the ice. Compared to the basic viscous-plastic method (Hibler, 1979) the EVP method converts the ice from plastic to elastic behaviour at small strain rates and is able to respond better to short timescale physical forces and is more efficient computationally (Hunke and Dukowicz, 1997, Bouillon et al., 2013).

The Semtner thermodynamics describe the formation of sea ice due to vertical ice accretion and melting (Semtner 1976) in a computationally efficient way. There is a horizontally uniform ice thickness, an overlying snow thickness that can accumulate seasonally, and one dimensional heat equations that govern the ice and snow temperatures. The melting of snow is considered to happen in such a relatively short time that the temperature change during this is not considered. The model also considers the effect of solar radiation on the ice, simplifying the formulation of previous work by Maykut and Untersteiner (1969) by storing the fraction of penetrating radiation not immediately melting the surface of the ice in a heat reservoir, representing internal meltwater. This energy keeps the temperature near the surface of the ice above its freezing point until it is exhausted, which has the effect of simulating the release of heat from the refreezing of internal brine pockets, preventing immediate surface melting in summer but slowing down internal cooling in autumn.

Single category sea ice means that the sea ice in a grid cell is represented by a single thickness and area. More recent sea ice models such as LIM-3 have multi-category sea ice, which means that a given grid cell can contain different thicknesses of sea ice sharing the area.

The ice in the model is ‘levitating’, as opposed to ‘embedded’. Levitating ice means that there is no direct exchange of mass between the sea ice and the ocean and the ocean volume does not change, which is the case when

embedding ice. The effects of sea ice formation and melting on ocean freshwater are instead represented by the effect that the constant salinity ice has on the ocean salinity, creating a virtual salinity flux. The disadvantage of such a method is that the exchange of salinity relies on a reference salinity value, which means that it is possible for salinity to not be fully conserved in a linear free surface model or one in which mass is not perfectly conserved (Tsubouchi et al., 2012). The embedded method can have its own deficiencies when dealing with the water being exchanged between the ice and ocean, as this can produce a specious circulation to compensate for the exchange (Stommel 1984).

The ice volume is determined by a product of ice fraction, the ratio of the cell covered by ice to the cell area, and the thickness of ice, considered to be the average over the whole cell (Fichefet and Morales Maqueda, 1997).

3.3 Run configurations

The model has a set of initial conditions when it runs, and it takes a substantial length of time to reach a quasi-steady state. This initial period of integrations is known as 'spin-up'. In NEMO, the initial temperature and salinity values are taken from the World Ocean Atlas (Levitus, 1988), while initial velocities are set at rest to zero, and sea surface height is flat, which sets an equal starting point for the model but means it has to spin-up before it produce meaningful results.

This project uses four different model runs to investigate the heat and freshwater of the Arctic Atlantic Water and the effects of different model configurations. These are all based on a global domain; regional domains are possible in NEMO. They are ORCA025-N206, ORCA025-N206Valor,

ORCA025-N206 ValorERA and ORCA0083-N001. The Valor runs are from the VALOR (VAlue Of the RAPID array) project, designed to assess the value of observations from the RAPID array in the Atlantic Ocean. The different configurations are outlined in Table 3.1. This makes it possible for this project to investigate different atmospheric forcings and resolutions.

ORCA025-N206 is effectively identical to ORCA0083-N001 except that ORCA025-N206 is a 1/4° model run with a linear free surface, while ORCA0083-N001 is 1/12° resolution and has a nonlinear free surface. The increased resolution should mean that circulation features and topography are better defined and more accurate, with the trade-off being processing power required. ORCA025-N206Valor and ORCA025-N206ValorERA are both 1/4° resolution runs with a linear free surface but differ in their atmospheric forcing, to see what effect this has on the model, as ORCA025-N206ValorERA uses ERA-Interim forcing.

ORCA025-N206 and ORCA025-N206Valor have identical configurations but have different start dates. The ORCA025-N206 run period is 1958-2007 and ORCA0083-N001 is 1978-2007, with data being used from 1981 onwards. The Valor experiment runs are for the period 1989-2007 and the data used starts at 1990.

The 1/12° run with the nonlinear free surface hence uses the z* grid but the data in this run was stored as if it was a linear free surface z-grid, so a calculated correction has to be added when dealing with advection, the method of which is detailed in Chapter 4.

3.3.1 Model outputs

NEMO produces output data files in NetCDF format that contain variables used for analysing runs. These fields include the corresponding coordinate and mask files for use depending on which part of the cell the tracer variables are positioned. The output is saved after every defined series of timesteps and then these are saved as averages over a time interval. The standard files have averages every five days, referred to here as 5-day means and then these files are averaged together to also produce monthly, annual and multi-annual average fields. This produces a trade-off between the amount of computer processing to do during analysis and the accuracy of the products of averages. For the most part, monthly means are used as the interval for this project as this provides sufficient information to be useful for seasonal trends while also being computationally practical.

This section has described how the NEMO model runs in this project are configured, from the primitive equations and the grid system to the features of the individual runs and the data that is available. The next chapter tests the accuracy of the model for use in understanding the Arctic Ocean heat and freshwater budget by investigating the fundamental property of mass conservation.

3.4 Tables and figures

Table 3.1: Summary of model runs used

Model Run	ORCA025-N206	ORCA025-N206 Valor	ORCA025-N206 ValorERA	ORCA0083-N001
Horizontal Resolution (degrees)	1/4°	1/4°	1/4°	1/12°
Run period	1958-2007	1989-2007	1989-2007	1978-2010
Atmospheric forcing	CORE-II	CORE-II	ERA-Interim	DFS3.2, DFS4.1, DFS5.12

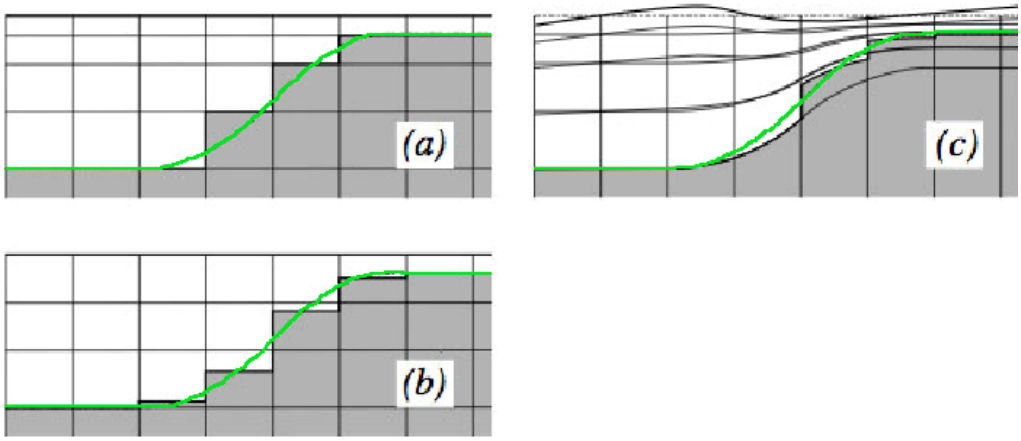

Figure 3.1 – The ocean bottom (green line) represented in different vertical coordinates: (a) z-coordinate with full step bottom cells, where the ocean bottom is rounded to the nearest cell, (b) z-coordinate with partial step topography, such that the ocean depth is taken at an average position for the grid cell it is in, (c) hybrid s-z coordinate with partial step, showing nonlinear free surface, adapted from Madec (2008).

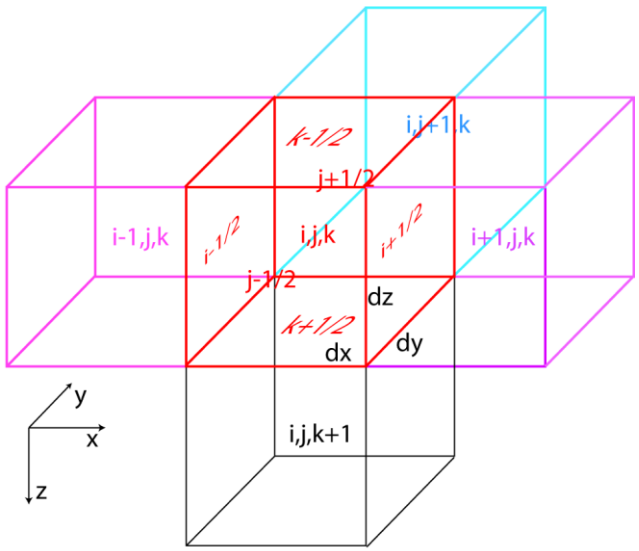

Figure 3.2 – Diagram of (i,j,k) grid array, taken from Huerta-Casas and Webb (2012). Half points are at cell faces, which correspond to translated Arakawa C-cell positions used in the model's u-, v- and w- grids.

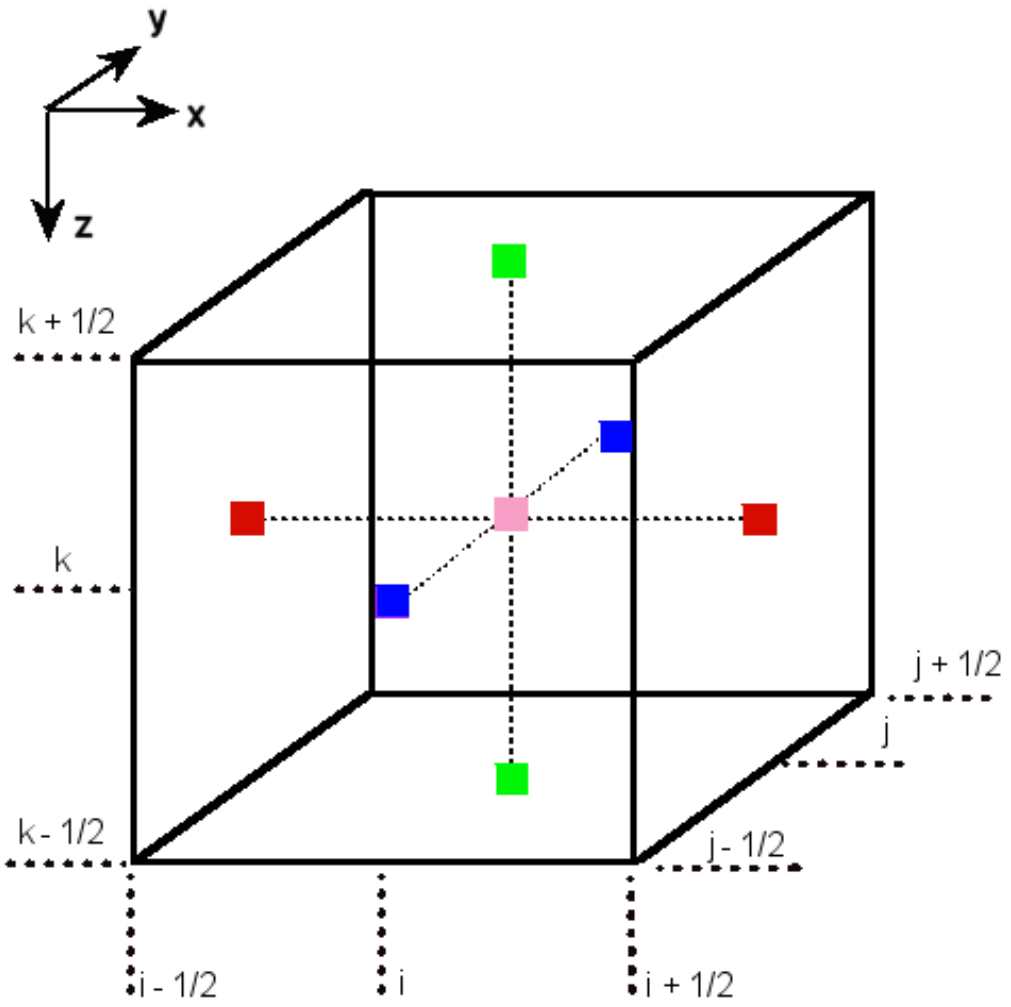

Figure 3.3 – Arakawa C-cell representation in 3D in (i,j,k) space, with T-point (pink) at centre of the body. U-points (red), V-points (blue) and W-points (green) are offset by half a cell. T-points are where quantities such as heat and salinity content values are stored, U-, V- and W- points are where velocity values between cells are stored. Redrawn from Ikawa and Saito (1991).

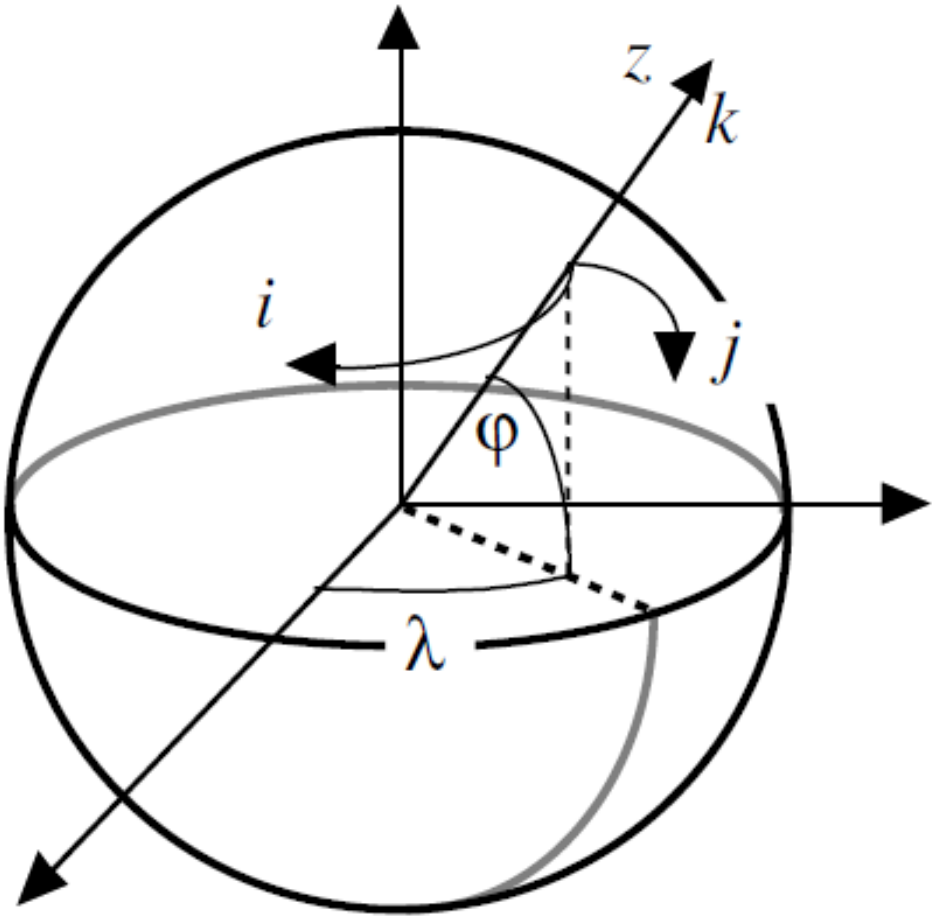

Figure 3.4 – The relation of curvilinear coordinate system (i,j,k) to geographical coordinates (λ, φ, z). From Madec (2008).

Chapter 4: Mass Conservation in NEMO

This section details the method of calculating NEMO model mass conservation from the smallest scale in the model of a single grid cell up to the Arctic Ocean region-wide scale in order to test the reliability of the model. Mass conservation is a fundamental property of an Ocean General Circulation Model, required for accurate calculation of the heat and freshwater budget. By conducting these calculations in 1/4° resolution for the first time, the uncertainty in the conservation is shown to be within the limitations of computer processing power and the model is suitable for analysis of the Arctic Ocean.

4.1 Mass conservation

NEMO is written formally and mathematically to conserve volume and Boussinesq mass (Chapter 3.1) and this applies in the whole ocean while the model is running. The standard use of the model runs is to use output data sets for subsequent calculations. The offline outputs are stored in discrete time intervals which means that the calculation processes have to be replicated in order to test conservation. In this project, we make offline calculations, using the standard Fortran 90 diagnostics software package for NetCDF4 files, CDFTools 2.1 (Molines 2006). The CDFTools calculate volume fluxes in exactly the same way that they are calculated in NEMO. The hypothesis is that the model outputs should also be able to conserve mass, supported by the fact that the model has previously been used effectively in other work (section 3.1).

The offline calculations could however lead to systematic error from the accuracy of output fields, data manipulation and other sources of uncertainty

that are described in detail further in section 4.6.4. Testing the mass conservation in the model will show the level to which other calculations made in the project are valid by how far the calculated conservations deviate from the expected value of perfect zero mass balance. This deviation shows the amount of uncertainty produced from making calculations.

Mass conservation in this sense is the balance in the system of the mass of water coming into and out of a region over a period of time. The accuracy of the mass conservation is important because if mass conserves perfectly then the inflow and outflow of temperature and salinity are independent of reference values (Tsubouchi et al., 2012).

This is demonstrated by the deriving the conventional equation for freshwater flux calculation. Consider the enclosed Arctic Ocean with volume V and salinity S. The net rate of change in freshwater by surface fluxes is F_s and the ocean flux through the sides (hereby known as boundary flux) is F_a. Assuming that there is mass conservation,

$$F_s + F_a = 0 \tag{4.1}$$

$$F_a = \oint v \, \partial A \tag{4.2}$$

where v is the distribution of ocean velocity perpendicular to the sides of the enclosed volume and dA is an area element of the side that the velocity acts on.

The surface freshwater flux is derived from volume and salinity fluxes. The rate of change in salinity inside the enclosed region is equal to the change in salinity from boundary fluxes.

$$\oint vS \, \partial A - \frac{\partial}{\partial t} \oint S \, \partial V = 0 \tag{4.3}$$

where ∂V is a volume element.

v and S around the boundary can be decomposed into a mean value and an anomaly, the deviation from the mean.

$$S = \bar{S} + S' \tag{4.4}$$

and

$$v = \bar{v} + v' \tag{4.5}$$

Crucially, mass conservation means that

$$\oint S' \partial A = 0 \tag{4.6}$$

and

$$\oint v' \partial A = 0 \tag{4.7}$$

This means that equation (4.3) can be expanded as

$$\frac{\partial}{\partial t} \oint S \, \partial V = \oint (\bar{S} + S')(\bar{v} + v') \partial A = \bar{S} F_a + \oint S' v' \partial A \tag{4.8}$$

The means multiplied by the integrals of the anomalies are exactly zero, so these terms vanish. This would not be the case if mass was not conserved.

Applying equation (4.2) to equation (4.6) and rearranging gives

$$F_S = \frac{\oint S' v' \partial A}{\bar{S}} - \frac{\frac{\partial}{\partial t} \oint S \, \partial V}{\bar{S}} \tag{4.9}$$

The first term on the right hand side is the boundary flux, which has a reference salinity implicitly being represented by the boundary-mean salinity $\bar{s}$ which is a clearly defined quantity. The second term is content change, the storage resulting from the difference between surface and boundary fluxes. Equation (4.9) is used in the freshwater calculation in section 5.5.2.

Mass conservation makes a temperature change equivalent to heat change as the temperature change will have been self contained from tracer advection in the ocean and not dependent on an unknown source. If the mass is not conserved then there is a dependence on the heat exchange on the predefined temperature of the system, which means conservation is not properly defined and that calculations on heat and salinity are subject to bias (Tsubouchi et al., 2012). When mass is conserved, a similar argument is made for salinity changes in the region being independent of the reference salinity.

If a model does not conserve mass then the sea surface height becomes out of control and the model will eventually fail and cease running. If Z-grid coordinates are used (section 3.1), it is possible for numerical instabilities to form in the simulations, such as cells becoming 'dry' with nothing stored in them (Adcroft and Campin, 2004) which then produces false results such as negative salinities. This would then need to be corrected by fixing a minimum sea surface height. If the Z* grid is used, which adjusts the grid length to accommodate the sea surface height, then this drying problem cannot happen but model velocities can then become unstable. In both cases, even if the model may be stable, the results will be inaccurate and the models cannot make long term climate predictions. There is scope for models to not conserve energy because they are used for short-term work (hour to day scale) and use data assimilation to want to understand winds and rainfall rather than to be stable in the long-term, such as weather forecast models. A model that assimilates data and maintains conservation would be extremely computer-intensive.

4.2 Transport components

There are three quantities that constitute the transport balance in and out of each model cell. These are horizontal advection, vertical advection, and content change.

In the regional calculation where there are multiple cells in three dimensions, the advections of adjacent cells balance each other out so that the only cells of interest are those at the region's exterior. In the case of the vertical transport, this boundary is at the atmosphere-ocean surface, where the term is a surface flux. This incorporates the restoring factor described in section 3.1 as part of it. In the horizontal direction, a continuous line of columns of cells forming a boundary is called a section. Figure 4.1 is a schematic of the transport balance for this formulation.

4.2.1 Advection

Horizontal advection is the transport perpendicular to the vertical cell faces. The vertical faces are parallel to either the grid zonal or meridional direction, so there are two forms of the advection equation. Advective transport of volume, F_a, is given by the velocity through the cell face multiplied by the cross-sectional area of the face.

$$F_a = v_u \times e_{2u} \times e_{3u} \tag{4.10}$$

or

$$F_a = v_v \times e_{1v} \times e_{3v} \tag{4.11}$$

Equation (4.10) is zonal transport, equation (4.11) is meridional transport. v is velocity, e_3 is the vertical scaling factor length and e_1 and e_2 are the

corresponding horizontal scaling factors, while the subscripts u and v denote which grid is being referenced. This terminology is consistent with that used by NEMO from section 3.1. This calculation is made over a section of grid cells which make up a vertical plane on the model grid defined by the start and end coordinates.

Vertical advection is perpendicular to the horizontal plane and acts vertically between cells that are below the surface. This works similarly to the horizontal advection except that the grid being referenced is now the w-grid and the surface area is the product of the horizontal scaling factors e_1 and e_2.

$$F_z = v_w \times e_{1w} \times e_{2w} \tag{4.12}$$

In a run with a linear free surface (described in section 3.1), the sea surface height is added to the top layer of cells for the e_3 height, while a nonlinear free surface has the sea surface height distributed among all the cells in a column. As outlined in section 3.1, an extra term is added to the advection in the ORCA0083-N001 run because it has a nonlinear free surface, but the data is only stored as if it was a linear free surface (pers. comm. G. Madec). This would otherwise create an error due to the incorrect definition of the e_3 term, as over time the calculated advections would be products of the average velocity, v and average depth, H, rather than the average of $(v \times H)$.

Starting with equation (4.11) (a similar equivalent correction is derived from equation (4.10)), and writing formally,

$$F_a = \sum_k \sum_i [e_1(i,j) \times e_3(i,j,k,t) \times v(i,j,k,t)] \tag{4.13}$$

where F_a is the horizontal boundary flux, e_1 is the horizontal scaling factor, e_3 is the vertical scaling factor, v is the velocity perpendicular to the grid cell, (i,j,k) are the summation indices and t is time.

The vertical scaling factor decomposes into the unperturbed depth $e_{3\phi}$ and the additional depth from the sea surface height, η as a fraction of the total depth H_ϕ.

$$e_3(i,j,k,t) = e_{3\phi}(i,j,k).(1+\frac{\eta}{H_\phi}) \tag{4.14}$$

Substituting (4.5) into (4.4)

$$F_a = \sum_k \sum_i \left[e_1 \times e_{3\phi}(1+\frac{\eta}{H_\phi}) \times v \right] \tag{4.15}$$

The e_1 term is independent of time, so this is taken outside as a constant. Expanding,

$$F_a = \sum_k \sum_i \left[e_{3\phi} \times v + e_{3\phi} \times \left(\frac{\eta}{H_\phi}\right) \times v \right] \tag{4.16}$$

The first half is already calculated as before and the second half is the required correction. To resolve this, the velocity is decomposed into a baroclinic and barotropic component as the baroclinic term will vanish and the barotropic term can be approximated into a solvable form. The correction term is

$$C = \sum_k \sum_i \left[e_{3\phi}.\left(\frac{\eta}{H_\phi}\right).(v_{baroclinic} + v_{barotropic}) \right] \tag{4.17}$$

Since the summation is over all depth, by definition

$$\sum_k v_{baroclinic} = 0 \tag{4.18}$$

Since the calculation is entirely barotropic and the pressure gradient force does not change with depth, the geostrophic assumption can be used. This assumption states that the Coriolis force is balanced by the pressure gradient force. This approximation is valid since it is being used at high latitudes, where the the Rossby number is small as the Coriolis parameter f is non-negligible.

The geostrophic assumption is

$$-fv = g\frac{\partial \eta}{\partial x} \tag{4.19}$$

where ρ_0 is reference density and g is gravity. The Coriolis parameter is calculated as

$$f = 2\Omega \sin \varphi \tag{4.20}$$

where Ω is angular velocity and φ is the latitude.

Substituting (4.19) into (4.17) for v,

$$C = \sum_k \sum_i \frac{e_{3\phi}}{H_\phi} \times \eta \times \frac{g}{f} \times \partial x\, \eta \tag{4.21}$$

Summing over k,

$$\sum_k e_{3\phi} = H_\phi \tag{4.22}$$

Substituting equation (4.22) into equation (4.21),

$$C = \sum_i \frac{H_\phi}{H_\phi} \times \eta \times \frac{g}{f} \times \partial x\, \eta \tag{4.23}$$

Since

$$\sum_i \frac{H_\phi}{H_\phi} = 1 \tag{4.24}$$

this leaves

$$C = g \sum_i \frac{1}{f} \eta \, \partial x \, \eta \tag{4.25}$$

Since

$$\eta \, \partial x \, \eta = \frac{1}{2} \partial x \, \eta^2 \tag{4.26}$$

substituting into (4.25)

$$C = \frac{g}{2} \times \sum_i \frac{1}{f} \partial x \, \eta^2 \tag{4.27}$$

This is integrated for all the cells along a section, the i index, from x_0 to x_1. f is a smooth function, which means that it has continuous derivatives. The solution is well defined within the limits of the integral however, so it can be taken outside of the integral. f^* is the mean value of f calculated over the path of the section. At the Arctic Ocean gateways, f^*changes by 0.05 across the Barents Sea Opening, while the other gateways are parallel to lines of latitude and f^* does not vary.

This leaves the correction to be added to the boundary flux in the nonlinear free surface ORCA0083-N001 model run as

$$C = \frac{g}{2f^*} (\eta_1^2 - \eta_0^2) \tag{4.28}$$

That is, the difference the between the square of the sea surface heights at the start and end of the section, scaled according to gravity and the Coriolis parameter. The squared sea surface height is an available data field in the model output.

4.2.2 Surface fluxes

The surface flux is perpendicular to the horizontal plane and acts at the atmosphere-ocean interface, which is at the top-most cell of a water column. A similar flux exists at the base of the water column between the ocean and the sea bed but the volume transport here is negligible and is considered to be zero in the model. The same applies for heat transfer.

For volume flux, the sources of water are evaporation, precipitation, river run off and damping, the sum of which is stored in the model as the variable emp (evaporation minus precipitation). The damping (described fully in section 3.1), is a restoring term that is used as a freshwater flux correction to improve the balance based on an observed, climatological or atmospheric model product, and sea surface salinity from the monthly mean Polar Hydrographic Climatology (Steele et al., 2001) and has a small influence on the flux in the order of 10^{-5} kg m^{-2} s^{-1}.

The real-world source of ice melt and freezing is treated differently in the model as the ice is considered to be levitating, so there is no volume transfer between the ice and the ocean. There is however a virtual salinity flux associated with this interaction so this term becomes necessary when calculating the freshwater conservation. Freshwater conservation is discussed further in section 5.3.3.

In summary, surface volume flux, F_s, of the top-most cell of a water column is given by the product of the volume input and the horizontal surface area.

$$F_s = emp \times e_{1t} \times e_{2t} \tag{4.29}$$

4.2.3 Content change

The content within the system is not constant; it changes due to the transports to and from the system. The volume of the cell at a point in time is calculated by multiplying the scaling factors of three dimensions together, and the volume change is the difference between the cell volumes over a time interval. For the volume conservation, if the density remains constant as defined by the Boussinesq approximation and the e_3 scaling factor remains constant, as in the model's linear free surface scenario, then the only change in volume content C_v is from a change in the sea surface height (SSH). This is applied by adding the SSH to the value of e_3 in the surface layer of cells, l=1.

$$C_{V,l=1} = e_{1t} \times e_{2t} \times (e_{3t} + \mathrm{SSH}) \tag{4.30}$$

In order to get the content change over a time interval, the content has to be calculated at the start and end of the interval, and to achieve an equivalent rate of change, the difference between the two is divided by the length of the interval.

$$\Delta C_v = \frac{C_{v\,end} - C_{v\,initial}}{\Delta t} \tag{4.31}$$

In standard model outputs, these required time points only exist as midpoints between two averaged data points either side of the required time point, which means interpolation is needed to get the volume at the correct moment in time. In the case of annual mean data, the mean volumes of the entire year either side of the required start and end of the year are used, which does not provide an accurate enough representation. The optimum is to interpolate as close to the required point in time as possible, which is done by using 5-day means either side of the point.

A better method for content change is to use model restart runs where possible, as these provide the instantaneous snapshot fields at the specific point in time. However, instantaneous fields are not commonly available, and therefore as a method it is unsuitable for long time series, something which is necessary to get a overall understanding of the variability. Also, since the data is obtained by restarting the model, the fields produced from this are independent of the fields from the standard outputs, which is a source of uncertainty when using both instantaneous and standard fields in the same calculation.

4.3 Single cell mass conservation

The starting point for calculating model mass conservation is to test it at the smallest scale possible, which is a single cell. The ORCA025-N206 run is used as this is in 1/4° resolution and to do this in the linear free surface model, we take a random cell at depth, avoiding complications from content change and surface fluxes. It is not possible to test this in 1/12° resolution because of the mismatch in the vertical lengths between the model run and the output file produced in the ORCA0083-N001 run. While is has been shown that there is a method for calculating a correction factor (equation 4.28), this is only true when considering the whole ocean column and it is not possible to determine the fraction of this correction that applies at the single-cell level.

The only inflow and outflow possible to the cell is from advection, equations (4.1), (4.2) and (4.3), at the six faces of the cell (Figure 4.2). The averaging period chosen for testing mass conservation in this configuration does not matter, since the linear free surface means that the change in vertical scaling factors and the volume conservation are independent of the temporal resolution of the output. A single 5-day mean field is chosen to minimise the

number of calculations used as the other averaging time periods are based on averages of the 5-day fields.

The volume imbalance, V_{imb}, is therefore the divergence of the cell, with the sign convention that transport is positive going out the cell.

$$V_{imb} = \sum F_a + \sum F_w \tag{4.32}$$

which is total of vertical and horizontal advection.

The numerical accuracy of the diagnostic tools is limited by the precision at which calculations are made. The uncertainty that this represents increases with the number of calculations.

The machine accuracy, ϵ_m is the smallest magnitude floating-point number which, when added to the floating point number 1.0 by the computer, produces a floating-point result that is different from 1.0. A typical 32-bit computer with floating point representation in base-2 has a machine accuracy of around 3×10^{-8} (Press et al., 1992). The round-off error that this produces depends on the number of arithmetic calculations, N, being made. If truly random, the round-off error can be on the order of $\sqrt{N} \times \epsilon_m$ while if the errors accumulate preferentially in one direction, it is closer to $N \times \epsilon_m$. This gives the relative error.

Since each advective transport is the product of the velocity and the two scaling factors perpendicular to the velocity, this is two arithmetic calculations per transport. The relative error, RE, is given by machine precision for the stored data multiplied by the square root of the number of arithmetic calculations.

$$RE = \sqrt{N} \times \epsilon_m \tag{4.33}$$

The absolute error, AE, is the relative error multiplied by the mean of the absolute value of the measured quantity, y.

$$AE = RE * y \quad (4.34)$$

If the divergence and absolute error are of the same magnitude, then it can be said that the calculation is within the limits of machine precision.

4.4 Simple region mass conservation

The progression of the mass conservation test is to then conduct an experiment over multiple cells, expanding in three dimensions to cover multiple full water columns of cells. This introduces the usage of surface fluxes and content change, with the volume imbalance now being a combination of equations (4.1), (4.2), (4.29) and (4.31).

$$V_{imb} = F_a + F_s + \Delta C_v \quad (4.35)$$

Since the input advective and surface fluxes are divergences, a positive value of these quantities means transport out of the system, while ΔC_v would be positive when the content has increased.

To obtain the Boussinesq mass imbalance, M_{imb}, the volume imbalance is multiplied by the reference density of seawater, ρ_{ref} = 1035 kg m^{-3}. The volume content and advective transport are of seawater, so this is realistic, however the surface fluxes are freshwater and the use of this reference density is only for calculating the model mass balance.

$$M_{imb} = V_{imb} \times \rho_{ref} \quad (4.36)$$

The only way for the volume of the region to change in the linear free surface model is as a change in sea surface height. The volume imbalance is

convertible to the equivalent sea level change per year Δh by dividing over the area of the region, A and multiplying by the number of seconds in a year, 3.1536×10^7.

$$\Delta h = \frac{V_{imb}}{A} \times 3.1536 \times 10^7 \quad (4.37)$$

The Arctic is chosen for this test as it is the focus of this project, and its construction has constant values of (i, j, k) at its boundaries. This means that all sections are parallel to one of the array directions, and the regional mask is rectangular, which simplifies the programming. This is appropriate for testing the properties of the model in the Arctic that do not require a precise definition of geography to derive precise physical quantities, such as the mass conservation in a region of cells.

In this simplified representation of the Arctic, the Davis Strait and Fram Strait section are effectively combined, though this section cuts through the entrance of Baffin Bay from the Canadian Arctic Archipelago and the Gulf of Boothia, which excludes Fury and Hecla Strait. This section continues on the same i-coordinate to close off the Barents Sea Opening, though this definition in reality misses much of the Barents Sea (Figure 4.3). This simplified region is an effective proxy for a more realistic domain as the most important quality of this experiment is to calculate over a similar number of cells that will have similar dimensions (as scaling factors are dependent on latitude and longitude and vary around the world) to show that the model conserves mass. The proper region is tested in Chapter 5 as a check on what the precise Arctic Ocean mass conservation value is.

This method uses ORCA025-N206 data for direct comparison with the single cell conservation, for a single time interval of one year (2007) with the optimised method where the instantaneous fields are available. It is then

conducted over the full 50-year model run as this will give an idea of the long term mass conservation, using annual mean data to reduce the amount of data to process. This also makes it obvious to use one year as the time interval between conservation tests.

4.5 Results

Table 4.1 presents the results of the advective transports through each individual cell face of the single cell mass conservation experiment using equations (4.1) (4.2) and (4.3) and the total divergence of the cell using equation (4.32). The offline calculations used 5-day mean output from ORCA025-N206 simulations to obtain the transports.

Table 4.2 presents the single year mass conservation in the Arctic Ocean for the simplified Arctic region. The offline calculations used annual mean output for advective transports and the regional surface flux for the period January-December 2007, while restart fields were used for the oceanic mass content on 1st January 2007 and 1st January 2008. The total imbalance is the sum of the divergences given by equation (4.35), converted into the Boussinesq mass using equation (4.36). There is a net outflow of mass through advective transport, and net inflow through precipitation. The precipitation is greater than the advection, and the oceanic mass increases. However, the increase in mass does not completely account for the divergence, as there is an excess mass of 1.322×10^{6} kg s^{-1} in the Arctic Ocean.

Figure 4.4 shows the mass imbalance results of the 50 year run of ORCA025-N206 per year, which uses the interpolation method for mass content change since instantaneous restart fields are not available for the series of annual time intervals. There is also a missing data point for the

content in December 1964 as the output file for this month did not exist in the system, which means that the content change cannot be calculated for 1964 or 1965, and these points are missing from the graph. The mass imbalance fluctuates over the 50 year run, with a 23 x 10^6 kg s^{-1} range.

Figure 4.5 shows the mass imbalances as a running average imbalance over the 50 years. The missing data points of 1964 and 1965 are void, as the average consists of the number of data points, not the number of years elapsed. After an initial fluctuation between 5.7 x 10^6 kg s^{-1} at 1959, which is the start of the run, and -0.5 x 10^6 kg s^{-1} in 1962, the average running imbalance settles to below 1 x 10^6 kg s^{-1} in 1975 and progressively approaches zero, while almost constantly remaining positive. At the end of the run in 2006, the running mass imbalance is 0.0341 x 10^6 kg s^{-1}.

Figure 4.6 plots the mass imbalances as a normal distribution, while Figure 4.7 plots these as a cumulative frequency distribution. Both figures use 2 x 10^6 kg s^{-1} bins of the imbalance to improve the smoothness of the curve. These curves look to have the shape that would be expected of a Gaussian distribution, with the majority of mass imbalances centred about 0 kg s^{-1}. The Anderson-Darling Test (Stephens, 1984) is used to test whether the distribution is normal. The normal probability plot (Figure 4.8) shows that the distribution is normally distributed as most points fall on the test's normal line. The P-value is 0.79, with the criterion being that if $P<0.05$, then the plot is not normally distributed, so it can be said that the distribution is normal. This means that there is a randomness to the mass imbalances rather than a systematic bias.

4.6 Discussion

The discussion section covers the mass conservation from the smallest spatial and temporal scale in the model up to the whole Arctic Ocean scale that is relevant for scientific investigation in this project, and assesses the significance and reasons behind the mass imbalance in the results.

4.6.1 Single cell mass conservation

The total divergence for the single cell was 3.2×10^{-4} m^3 s^{-1}, which is seven orders of magnitude lower than the advective transports coming in and out of the cell. While this is a very small fraction, the principle remains that there can be transports coming in and out of the cell but the overall cell divergence should be zero. In order to find the absolute error represented by this, equations (4.33) and (4.34) calculate the relative and absolute errors respectively. The machine precision for 32-bit stored data is 3×10^{-8} and there were 17 arithmetic calculations involved, with the calculation of the advective fluxes and summation of them. This gives an absolute error of 3.9×10^{-4} m^3 s^{-1}. The divergence is of the same order of magnitude as the absolute error, so this suggests that the conservation calculation is at the limits of machine precision. Therefore we conclude that the model is reliable at the individual cell scale in terms of the uncertainty caused by imperfect mass conservation. This means calculations of freshwater and heat are inherently reliable and unbiased. (equations (4.6) and (4.7)). However, this on its own does not yet prove that the level of uncertainty is acceptable when calculating over a large region of several million grid cells such as the Arctic Ocean. This is resolved in section 4.6.4.

4.6.2 Single year regional mass conservation

The first step towards testing what happens on a larger scale is by testing it for a single year, the shortest standard timescale used for annual variability. The 1/4° Boussinesq mass imbalance of -1.322×10^6 kg s^{-1} in Table 4.1 is a net excess in the 2007 mass budget of the Arctic Ocean, as the negative divergence exceeded the increase in the stored mass. With a calculated area of the ocean region of 9.596×10^{12} m^2, by using equation (4.37) this mass imbalance is equivalent to a sea level change of 4 mm yr^{-1}. The amount of mass imbalance suggests that the model conserves while there is some level of uncertainty introduced through the calculations. Although the content change is not enough to account for the disparity between the surface flux and horizontal advection, the positive value of the change shows an increase in the overall volume content, while there was net surface flux in, and net advective transport out, which agrees with the theory based on section 2.1.4 that river runoff and precipitation are the main sources of water entering the Arctic Ocean. This suggests the ocean must flush this input out due to the pressure gradient force that this excess of water that builds up, though some of it remains in the Arctic over the course of the year.

4.6.3 50-year regional mass conservation

The single year test showed that there is some mass imbalance in the Arctic Ocean. To test whether for whether there is a systematic bias in the mass conservation, indicating an issue with the model, or if there is random uncertainty causing the imbalance, indicating that it is an unpreventable consequence of making calculations, we tested the conservation for the full model run, between 1958 and 2007. Due to the absence of a full set of instantaneous restart fields, we used the next best approximation, which was

to use the 5-day means to interpolate for the start and end of each year. The restart fields, calculated by a re-run of the model from a previously calculated new starting point, would give the precise snapshot of the Arctic Ocean volume at the start and end of each year and the most accurate change in content over the year (equation 4.31).

The final year in which there is data to use for the interpolation of oceanic content is 2007, which means that the final mass imbalance data point is for 2006. Therefore, the result from the single year imbalance in 2007 cannot be directly compared with the 50-year regional test. This would have been useful to investigate the effectiveness of using instantaneous restart fields rather than the interpolation method of 5-day means for the content change.

The results show that there is some amount of random fluctuation in the mass imbalance, and some years have quite a severe imbalance, shown in Figure 4.4. However, the mean of the imbalances is very small, at 0.034×10^6 kg s^{-1}, with a standard deviation of 5×10^6 kg s^{-1}. The plotting of the running averages in Figure 4.5 shows that the first ten years of the run have a large average imbalance, before the imbalance settles to a more acceptable level and approaches zero. This suggests that the imbalance is due to a source of random uncertainty that is eventually smoothed out when looking at the entire run, such as spin-up. This means that in this period calculations of heat and freshwater are more influenced by the reference salinity and reference temperature used and are less reliable. The Gaussian shape of the frequency distribution curves in Figures 4.6 and 4.7 suggests that the uncertainty is random. The running average imbalance at the end of the run, 0.0341 s^{-1}, is positive, which means that this is the amount that the oceanic mass change has exceeded the net divergence over the course of 50 years. This is significantly smaller than the value from the single year mass conservation,

which means that over the course of the run, fluctuations even themselves out to close to zero and the model is reliable for use in calculating quantities of freshwater and heat.

4.6.4 Sources of uncertainty

The factors that produced mass balance fluctuations and non-zero mass conservation need to be examined. The potential sources of uncertainty are:

Asselin filtering - The model works by calculating at every second time step and taking the average of two time steps to obtain the value at the in-between time step. Asselin filtering is a way to connect the time steps together and smooth the results. The problem with this when trying to find the conservation is that this inherently takes weighting from time steps either side of the desired point in time, so that when a value is provided, it is not necessarily the true value at that time, and there are uncertainties obtained from outside the specified period of conservation. The Asselin filter is particular to the version of NEMO used in this project, NEMO 3.2 and earlier runs, and has been replaced in more recent builds for a system that produces calculations at the time steps because it was non-conservative. The effect of this could be tested by conducting the conservation tests on other model runs from more recent versions of NEMO.

Asynchronicity - The different forcing fields operate on slightly different time steps, so that when they form part of the same equation, as in this experiment, it is not necessarily true that each data point refers to the true value at an exact point in time as some interpolation has taken place.

Single precision NetCDF4 data files - The output data files are stored as single precision, since double precision would make the amount of data too large to

manage. Ultimately, by using millions of grid cells, the uncertainty from the lack of precision starts to accumulate, such that there could be a significant uncertainty, especially when the aim is to prove that the sum of all the components is exactly zero. The exception to this is the instantaneous restart fields used in the content change calculations, which are stored in double precision.

Double precision computing - The computing is done in double precision, and the programs are written in such a way as to generally maximise the precision available. The scaling factor data is stored in double precision and the velocities are stored in single precision in the standard outputs of annual, monthly and 5-day means. The instantaneous means used for the content were double precision.

The absolute error from the single cell calculation suggests that the precision of the computing is a plausible candidate for the limitation of the accuracy of the mass conservation. To demonstrate the affect this has when taking into account the number of model cells present in the Arctic Ocean, the calculated single cell non-conservation can be upscaled to the Arctic equivalent.

Annual non conservation is given by the 5-day error multiplied by the square root of the number of 5-day intervals in a year, 73. The multiplying factor of the number of cells in the simplified Arctic domain is 7×10^7, which gives an upscaled annual non-conservation of 22.6 $m^3 s^{-1}$. In comparison, the regional single year rate of volume imbalance was 1277 $m^3 s^{-1}$, or 10^{-3} Sv, while the long-term mean volume imbalance was 32.9 $m^3 s^{-1}$, or 3×10^{-5} Sv. The long term mean of the regional imbalance and the upscaled single cell imbalance have the same order of magnitude, which means that the computing precision is the limiting factor of accuracy in mass conservation and any other

calculations that may be subsequently made involving CDFTools analysis of NEMO. Meanwhile, the vast difference in the between the upscaled single cell and the regional single year suggests that there may be some factor creating variations over a short timescale.

The main conclusion that would be drawn from this though is that the model conserves mass to a tolerable level in ORCA025-N206, and it would be believed that similar results could be found by testing other NEMO model runs of a similar configuration because they perform calculations in exactly the same way. In the case of the 1/12° resolution, there are three times as many cells in each direction as in 1/4° resolution, but the fluxes in each should be on average a third of what they are in 1/4° resolution, so this should cancel out. This is tested in chapter 5.

Physical factors - The assumption has been made that the model works accurately and that problems are computational. However, there is a possibility that there is some sort of physical reason that the model does not fully capture that can result in an imbalance. One potential cause would be the response timescale to perturbations inside the region. Since the physical quantities are supposed to balance each other, if there is not an instantaneous response (which due to averaging periods is not guaranteed) then a short-term imbalance is inevitable. This can be represented in the annual averages if one flux has not fully compensated for another by large imbalances, which are shown to occur in Figure 4.4.

This chapter has rigorously tested the mass conservation of NEMO for the first time and has shown that this conservation holds within the limit of computer precision. There are several sources of uncertainty that produce fluctuations in the mass conservation that have been identified but these average themselves

out over a period of multiple years. This means that calculations of tracer fluxes in the model such as freshwater and heat are reliable. The next chapter calculates these quantities in the Arctic Ocean.

4.7 Tables and figures

Table 4.1: Single cell volume conservation for a single 5-day period

Cell Face	Volume transport ($m^3\ s^{-1}$)
1	2400.05078
2	-1612.75100
3	-2907.94081
4	1562.66497
5	-4955.52604
6	5513.54748
Total divergence	0.00032

Table 4.2: Arctic Ocean mass conservation for a single year

Component	2007 Mass transport ($10^6\ kg\ s^{-1}$)
Advection	150.726
Surface Flux	-169.648
Content change	17.600
Total imbalance	-1.322

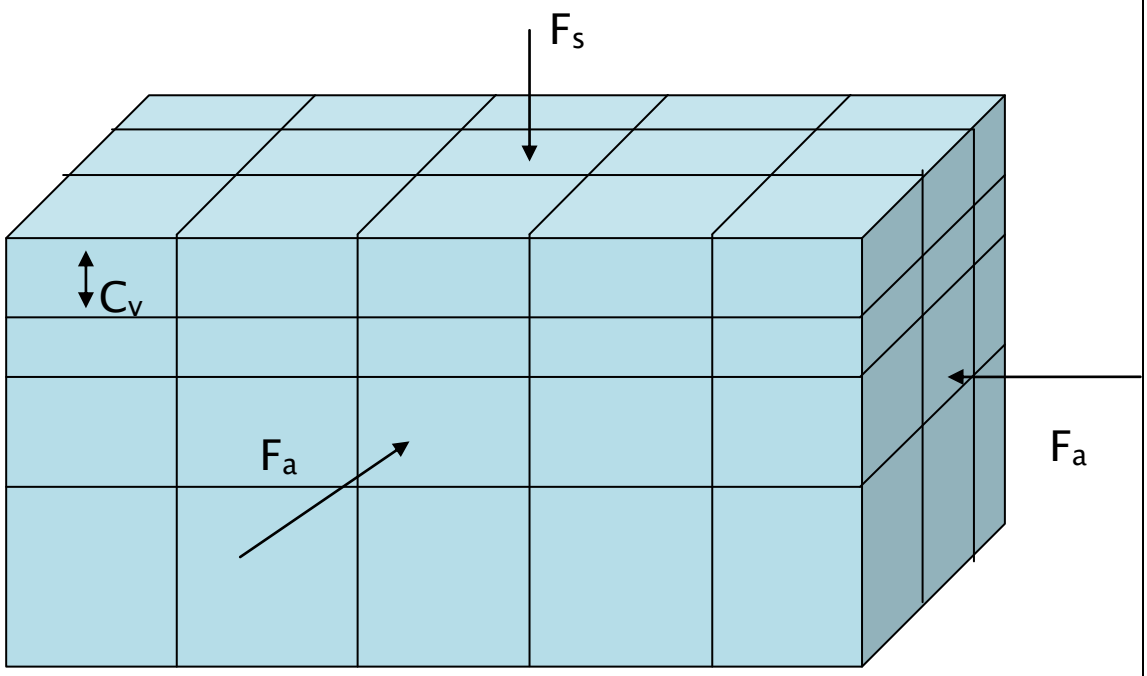

Figure 4.1 – Schematic of the transport components in the array of grid cells: horizontal advection F_a, surface flux F_s and content change C_v.

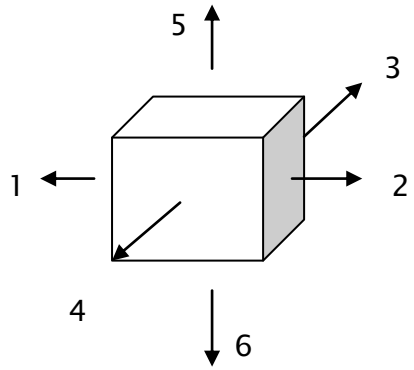

Figure 4.2 – Schematic diagram of the advective transports for a single cell. Divergence is positive.

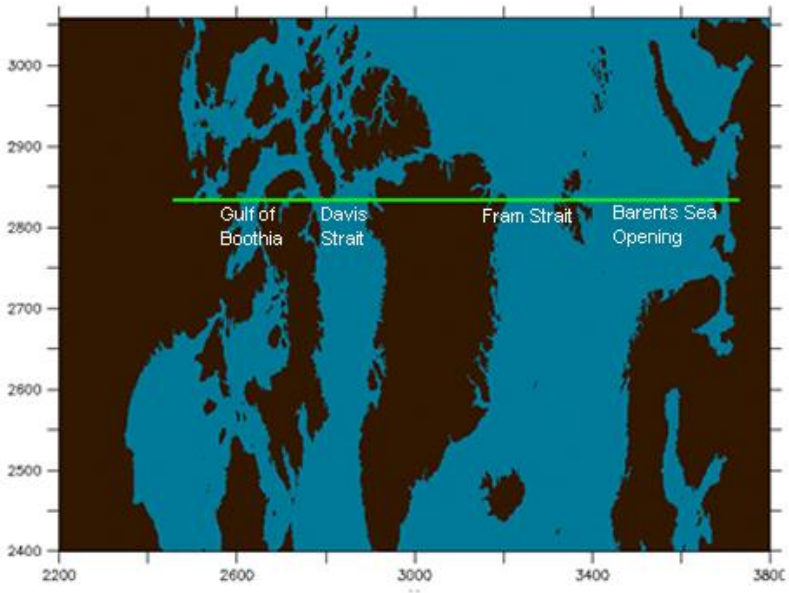

Figure 4.3 – Map of simplified Arctic region defined by southern boundary along constant model J- coordinate neglecting much of Barents Sea and Baffin Bay.

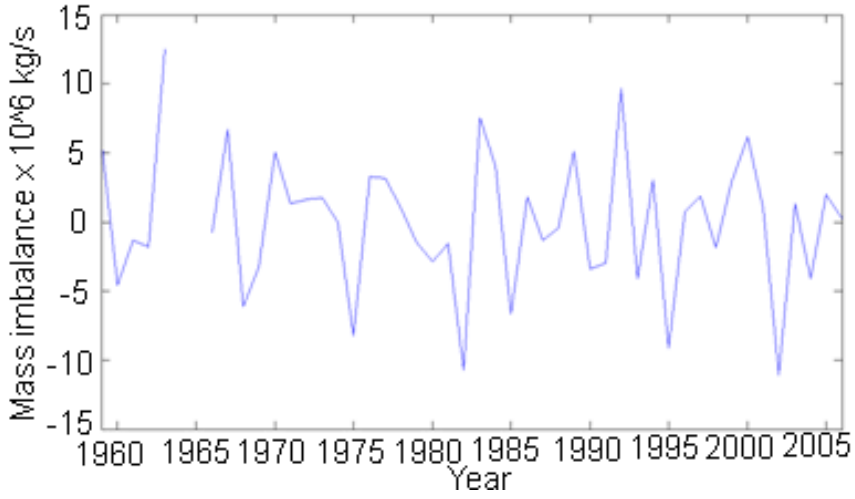

Figure 4.4 – Mass imbalances for the period January 1959 – December 2006 in the simplified Arctic region, using annual mean divergences and interpolated oceanic 5-day mean mass contents from ORCA025-N206. The gap in the line is due to a missing output data file which meant that the volume change could not be calculated between two years.

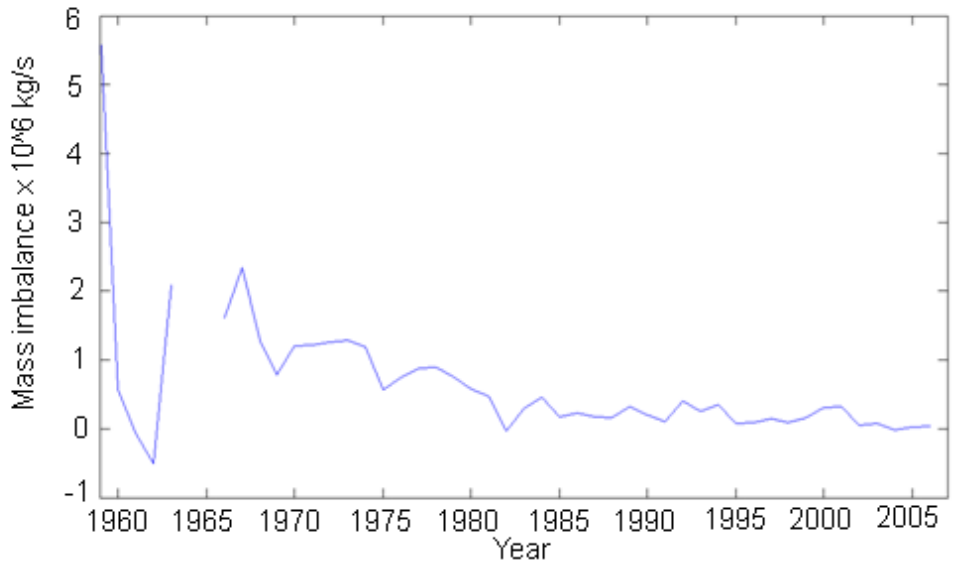

Figure 4.5 – The corresponding running average mass imbalance over the 50 year run.

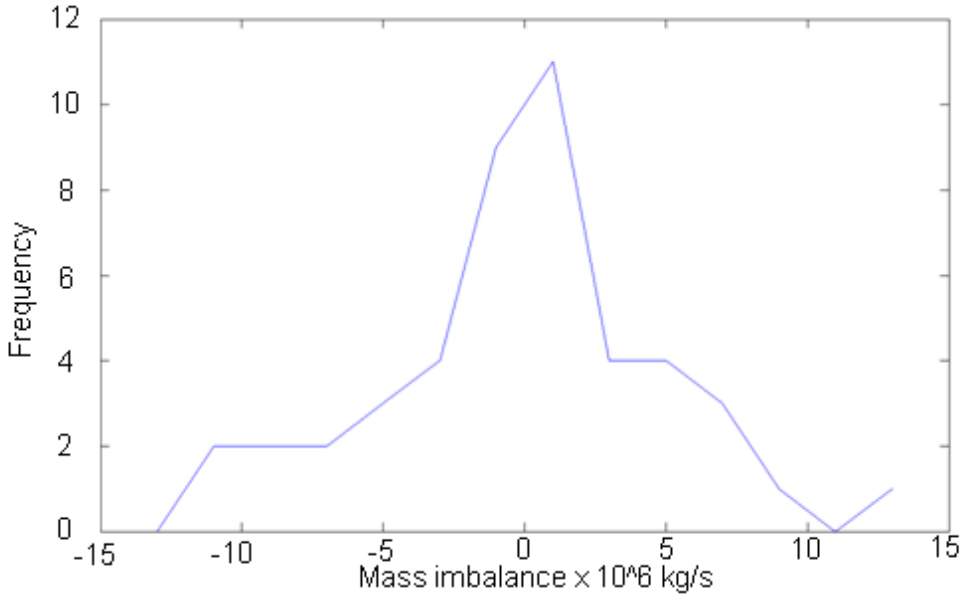

Figure 4.6 – Normal distribution of the 50 year mass imbalance, in 2 kT s^{-1} bins.

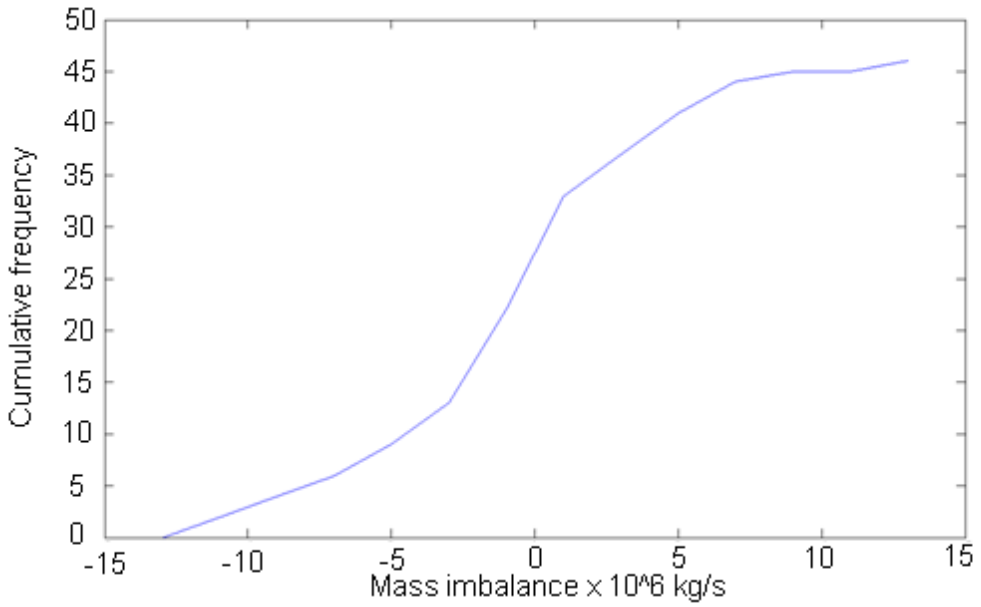

Figure 4.7 – Cumulative frequency of the 50 year mass imbalance, in 2 kT s^{-1} bins.

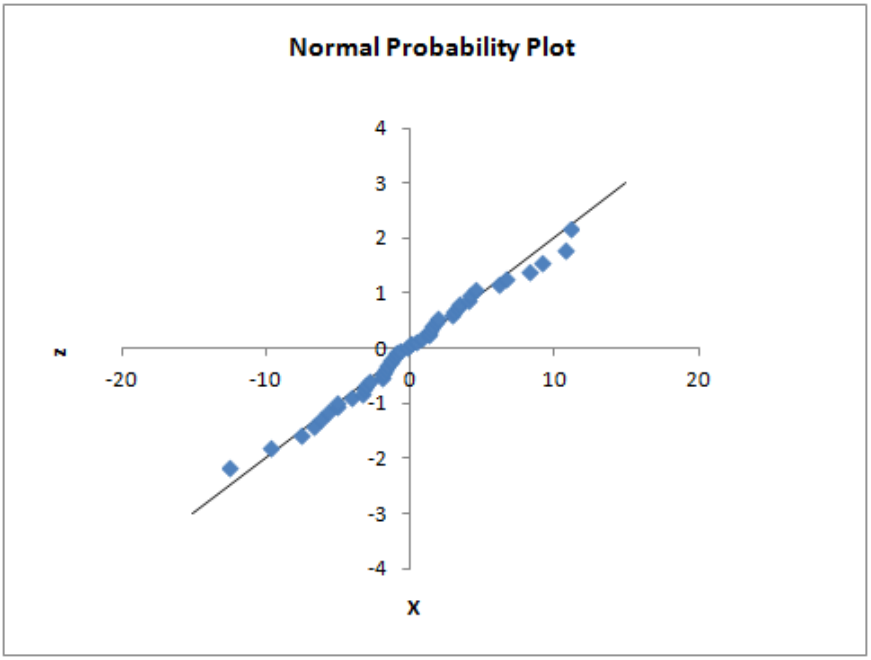

Figure 4.8 – Normal distribution plot of the Anderson-Darling test on the set of mass imbalances over 50 years. The majority of points are on the line, which shows that the data is normally distributed.

Chapter 5: **Arctic Ocean Fluxes**

This section investigates the thermodynamic fluxes that enter and leave the whole Arctic Ocean to understand its overall physical behaviour. It focuses on the heat and freshwater budgets of both the solid and liquid water components of the ocean. A comparison of different model runs shows the influence that resolution and atmospheric forcing can have on the results, while a mass conservation check determines the level of uncertainty in the calculations. It is shown that a large amount of heat is lost to the surface through radiation, while the boundary fluxes show a delayed response to the surface flux processes. The different atmospheric forcings and resolutions have a broadly similar effect except for when they are inaccurate, in which case they have a profound impact on calculations.

The data from the four runs used in this project is analysed using the same method of calculation for each. Continuous output from the model is aggregated every five days. Monthly averaged time series are used to get a sufficient level of detail to see the amount of fluctuation over each year, while the annual averaged time series is produced from these monthly averages to show interannual variability over the length of the run. This covers 1981-2007 for the comparison of resolutions and 1988-2007 for the comparison of atmospheric forcing. The monthly results are then used to create seasonal averages to show the long-term trends within years.

The principal quantity to analyse is the heat budget of the whole Arctic, which is composed of the advection of moist static energy (Overland et al., 1996). This is heat transported through the boundary flux of water and ice, the heat exchange between the surface of the ocean and the atmosphere through ice formation and radiation, and the long-term overall stored energy within the

region. The freshwater budget is also relevant as it is part of the climate system and may be representative of the ice coverage as the ice is fresher than the sea water. The amount of ice may then relate to the state of the heat balance of the region as the temperature of ice and its formation and melting contribute to the energy budget.

5.1 Region

The definition of the region for all of the calculations in this chapter is that of the whole Arctic as described in section 2.1, including the central Arctic basin and the shelf seas, bounded by model sections that are chosen to coincide with paths where observations have been made. The model grid interpretation of the boundary sections was produced by using a CDFTools program to convert all the available latitudes and longitudes of the observed sections into equivalent grid coordinates. The map of this region is Figure 5.1.

5.2 Transports

The heat and freshwater budgets of the liquid ocean are formulated in a similar way to the mass budget of Chapter 3. There is an advective transport component; the main difference in these budget calculations from the mass conservation is the use of derived quantities in the transport calculations.

5.2.1 Liquid heat component

The advective transport of heat in water F_{aT} is the product of velocity, v, temperature, T, and the cross sectional area of the cell face defined by the cell lengths e_1, e_2 and e_3, integrated over all of the faces along the boundary of the region. The tracer data is stored in the central t-point of the model grid cell

while the velocity data is stored at the faces of the cell relative to the t-grid, so interpolation of the cell temperatures is used to get the correct value of the transport at the boundary (see section 4.2.1).

NEMO is capable of producing a combined velocity x temperature (vT) measurement as the model is run but this does not exist for every available averaging period for the model runs being used. When this has not been done (such as in the ORCA0083-N001 model run), it is necessary to calculate offline the product of the velocity and the temperature of the ocean, both of which are variables that have already been averaged over the time period. The usage of the product of averages provides a source of uncertainty in the method. Equation (5.1) is zonal transport, equation (5.2) is meridional transport.

$$F_{aT} = v_u \times e_{2u} \times e_{3u} \times T \tag{5.1}$$

or

$$F_{aT} = v_v \times e_{1v} \times e_{3v} \times T \tag{5.2}$$

5.2.2 Solid sensible heat component

The solid form of water within the region is part of the energy budget of the system as it has an associated temperature that can be transported as a boundary flux and it exchanges heat with its surroundings when it forms and melts to provide both a boundary and surface flux. This can be as either snow or ice, in which the snow precipitate exists as a layer on top of the ice or is otherwise instantly converted to water if it falls on ocean. The sensible heat component is the heat stored within the ice that has an effect on temperature, and has a transport component in the system as the import and export of the solid from the region. The sensible heat transport F_{sen} is the product of the ice density ρ_{ice}, the sensible heat capacity of ice c_{ice}, the temperature of the ice

T_{ice}, the ice velocity v_{ice} which has meridional and zonal components, the fraction of the grid cell containing ice, f_{ice}, and the scale factor along the cell boundary (e_1 or e_2) as a dimension.

$$F_{sen} = \rho_{ice} \times c_{ice} \times T_{ice} \times f_{ice} \times v_{ice} \times e_{2u} \quad (5.3)$$

or

$$F_{sen} = \rho_{ice} \times c_{ice} \times T_{ice} \times f_{ice} \times v_{ice} \times e_{1v} \quad (5.4)$$

Equation (5.3) is zonal transport, equation (5.4) is meridional transport.

5.2.3 Solid latent heat component

The solid latent heat component refers to the heat from the formation and melting of ice and snow. There is also a transport component from this process, associated with the latent heat of the ice and snow that has been either imported and melted within the region, or has formed within the region and exported to then melt outside of the region, as this heat is not self-contained in the region.

The latent heat transport of ice is the product of v_{ice}, f_{ice}, ρ_{ice}, the ice thickness z_{ice} and the latent heat of ice formation l_{ice}. The latent heat transport of snow is similar, using the snow thickness z_{snow}, and snow density ρ_{snow} instead but still using the latent heat of ice formation for latent heat of snow formation as the two are similar to each other (Singh and Singh, 2001). The adding together of the transport of latent heat of ice and latent heat of snow gives the total latent heat transport F_{lat}. Equation 5.5 is zonal transport, equation 5.6 is meridional transport.

$$F_{lat} = (\rho_{ice} \times z_{ice} + \rho_{snow} \times z_{snow}) \times l_{ice} \times v_{ice} \times f_{ice} \times e_{2u} \quad (5.5)$$

or

$$F_{lat} = (\rho_{ice} \times z_{ice} + \rho_{snow} \times z_{snow}) \times l_{ice} \times v_{ice} \times f_{ice} \times e_{1v} \quad (5.6)$$

5.2.4 Freshwater

The freshwater component is determined relative to the reference salinity S of 34.8 PSU (practical salinity units), which chosen to be consistent with the model and is commonly used in studies (e.g. Aagaard & Carmack, 1989, Serreze et al., 1996, Rattan et al., 2010). For a model cell with a salinity that is different from the reference salinity by ΔS, the freshwater FW at the given point is

$$FW = 1 - \frac{\Delta S}{S} \quad (5.7)$$

The freshwater transport F_{aF} (first term on right hand side, equation 4.9) is then the value of the freshwater multiplied by the velocity anomaly v' (actual velocity v minus section mean $\bar{v}$) through the cell and surface area of the cell from the products of the cell lengths e_1, e_2 and e_3.

Equation 5.5 is zonal transport, equation 5.6 is meridional transport.

$$F_{aF} = v'_u \times e_{2u} \times e_{3u} \times FW \quad (5.8)$$

or

$$F_{aF} = v'_v \times e_{1v} \times e_{3v} \times FW \quad (5.9)$$

The value of FW is interpolated between two cells to get the value on the face of the cell where the boundary of the region lies.

5.3 Surface Fluxes

There are fluxes of heat and freshwater between the surface of the ocean, the atmosphere and sea ice that overlies the ocean, and the interface being the upper boundary of the region.

5.3.1 Liquid heat

The surface heat flux is described by the model as 'Net Downward Heat Flux' (described as emp_t), which includes the latent heat involved in evaporation and precipitation, and the heat from the water from river run off. The river run off is added at the surface layer of cells at the oceanic temperature, while evaporation and precipitation is at the near surface temperature. The liquid heat surface flux F_{sT} is calculated by multiplying emp_t by the horizontal surface area of the top layer of model cells.

$$F_{sT} = emp_{\mathrm{t}} \times e_{1t} \times e_{2t} \tag{5.10}$$

5.3.2 Latent heat

Within the calculation of the heat surface flux, the freezing and melting of sea ice produces a surface flux of latent heat that is exchanged with the ocean. The ice latent heat surface flux F_{slat} is calculated by multiplying the horizontal surface area by the latent heat capacity and the ice formation rate, r_{ice}.

$$F_{slat} = e_{1t} \times e_{2t} \times l_{ice} \times r_{ice} \tag{5.11}$$

5.3.3 Freshwater

The freshwater flux is treated by the model as a virtual salinity flux. Due to the levitating ice, there is no volume (and mass) exchanged between the water and

the ice (as previously stated in section 4.2.2), so the effect of sea ice formation is to exchange a corresponding amount of salinity according to the fixed ice salinity of 6 PSU. This salinity can be expressed as a freshwater flux. The equivalent salinity flux method improves the performance of the model by allowing observed temperatures and salinities at the surface to be reproduced but has shortcomings in the unrealistic dynamic processes that are used to implement this, which becomes an issue when observations are not available and care must be taken to correctly formulate the freshwater conservation (Huang, 1993, Tartinville et al., 2001). This is important in the context of section 2.1, as small changes in freshwater can have a significant impact on the climate.

The freshwater component also contains the evaporation, precipitation and river runoff water. The model variable containing the freshwater flux is described as the 'concentration/dilution water flux', emp_f, acting on the uppermost layer of cells and is in units of kg m^{-2} s^{-1}. The freshwater surface flux is obtained by dividing this by the density of seawater ρ_{ref} and multiplying by the surface area of the cell's interface with the atmosphere.

$$F_{sF} = \frac{emp_f}{\rho_{ref}} * e_{1t} * e_{2t} \qquad (5.12)$$

5.4 Content change of temperature and salinity

The content change is calculated as the difference of the content integrated over all of the cells in the region between the start and end of the time interval. Compared to the mass conservation method, the temperature and salinity can change in all of the cells, so it is necessary to calculate the content of the whole depth rather than just the surface layer modified by the sea surface height (SSH).

5.4.1 Heat content

There are two ways of obtaining the heat storage of the system. One way is to calculate the heat content of the entire ocean and the change of this over time is the storage.

The equations for temperature content, C_T at a depth level l are

$$C_{T\ l=1} = T \times e_{1t} \times e_{2t} \times (e_{3t} + SSH) \quad (5.13)$$

$$C_{T\ l>1} = T \times e_{1t} \times e_{2t} \times e_{3t} \quad (5.14)$$

The rate of change of temperature content is taken between the temperature content at the end and the start of the time period.

$$\Delta C_T = \frac{\sum C_{T\ end} - \sum C_{T\ initial}}{\Delta t} \quad (5.15)$$

The change in temperature content over time has the effect of being a flux that contributes to the overall heat balance.

These calculations are generally dependent on the definition of the reference temperature, however the conservation of mass in the model means that this is not an issue (Tsubouchi et al., 2012, see section 4.2.1). A reference of 0°C is used by the model and subsequent calculations associated with heat.

5.4.2 Freshwater content

There is a freshwater content relative to the reference salinity that resides within the ocean, and this can change over time. It is necessary to include this in calculations of the freshwater budget to ensure that storage within the region is accounted for.

The freshwater volume is the product of the cell volume and the freshwater content that is derived from the cell's salinity, S.

$$C_{f\ l>1} = \left(1 - \frac{S}{Sref}\right) * e_{1t} * e_{2t} * e_{3t} \quad (5.16)$$

$$C_{f\ l=1} = \left(1 - \frac{S}{Sref}\right) * e_{1t} * e_{2t} * (e_{3t} + SSH) \quad (5.17)$$

$$\Delta C_f = \frac{\sum C_{f\ end} - \sum C_{f\ initial}}{\Delta t} \quad (5.18)$$

There is a second way of obtaining freshwater content. Instead of calculating the content of the ocean for the entire length of the model run (an intensive process), it is possible to derive the content from the other known quantities that form the freshwater budget (section 5.5.2). This is an important calculation for determining the pattern of freshwater storage in the Arctic, which is related to sea ice formation, stratification of water masses and ocean circulation (section 1.2).

5.5 Total budget

These individual components combine to form the total budgets for heat and freshwater for both liquid and solid components.

5.5.1 Heat budget

The total liquid heat budget, giving the imbalance of the heat in the system C_{imb}, is the sum of equations (5.1), (5.2), (5.10) and (5.15), where F_{aT} is the sum of the meridional and zonal advections.

$$C_{T\ imb} = F_{aT} + F_{sT} + \Delta C_T \quad (5.19)$$

$C_{T\ imb}$ should add up to approximately zero over a long term average once perturbations in the system have affected the balance and have settled out to a dynamic equilibrium.

The total heat storage for the region F_{tot} is the combination of the different solid and liquid parts to form an overall budget, combining equations (5.3), (5.4), (5.5), (5.6) and (5.11). The transport components F_{lat} and F_{sen} incorporate the zonal and the meridional terms.

$$F_{tot} = F_{lat} + F_{sen} + F_{slat} \tag{5.20}$$

5.5.2 Freshwater budget

The liquid freshwater budget is the sum of equations (5.8, 5.9, 5.12 and 5.18), the advection (in both zonal and meridional directions), surface flux and content change respectively.

$$C_{f\ imb} = F_{aF} + F_{sF} + \Delta C_f \tag{5.21}$$

Calculating the storage timeseries C_f can be done directly (equations 5.16, 5.17), or it can be done indirectly. Taking equation (4.9) as a starting point,

$$F_s = \frac{\oint S'v'\partial A}{\bar{S}} - \frac{\frac{\partial}{\partial t}\oint S\,\partial V}{\bar{S}} \tag{4.9}$$

the right hand term for content change can be rewritten in terms of volume storage C_v and, freshwater storage C_S.

$$F_s = \frac{\oint S'v'\partial A}{\bar{S}} + C_s - C_v \tag{5.22}$$

This is then rearranged to obtain C_s by also using the assumption from equation 4.35 that when mass conserves, $F_s + C_v = F_a$.

$$F_a - \frac{\oint S'v'\partial A}{\bar{S}} = C_s \tag{5.23}$$

5.6 Uncertainty from mass conservation

The model has been shown to conserve mass almost perfectly as predicted (section 4.1), so it can be assumed that model calculations of heat and freshwater are independent of any defined reference values used. The non-zero value of the imbalance that we believe is due to the computing precision suggests that subsequent calculations will also have a corresponding uncertainty for this reason.

The mass components for this region are calculated in the same way as the 50-year run in Chapter 4 but for the shortened period covered by the 1/12° run. The purpose of this is to determine the significance of the mass imbalance compared to the individual components as a way of estimating the level of uncertainty in the other budget calculations. The long term average of the individual mass components is divided by the mass imbalance over this time period to obtain a fractional uncertainty. The calculation is made at this stage so that the regional areas match each other and the level of mass imbalance is representative of the whole Arctic area being defined for this part of the project, whereas the simplified region of Chapter 4 is not directly comparable for this purpose as the imbalance scales by the area. A similar sized area in another part of the global ocean should therefore produce a similar mass imbalance but this is not tested.

5.7 Results

Figure 5.2 shows the monthly SSH^2 correction for the nonlinear free surface to the boundary flux in the ORCA0083-N001 that compensates for the linearisation of the vertical scaling factor data. It varies seasonally with the greatest adjustments occurring in winter and results in a greater outflow. This

outflow averages -10 mSv in the period 1981-1990 and then gradually increases after the updated atmospheric model to -40 mSv by the end of that part of the run in 2007. This shows that this correction is non-negligible and is necessary to achieve the correct formulation of the boundary flux.

Figure 5.3 shows the monthly damping flux and Figure 5.4 shows the annual damping flux for all the atmospheric forcings used. The amount of damping is negative for a single month in the summer and returns to a positive value for the rest of the year, which helps to properly account for the freshwater removal from sea ice formation in the winter. There is little annual variation in the damping, with the winter peak freshwater removal at 150 ± 50 mSv. The main difference is in the 1/12° DFS4 run which has a significantly larger positive damping of 300 mSv between 1981 and 1991 that is then reduced to 100 mSv after an update to the atmospheric forcing in 1990. This reduced value is still greater than the 1/4° CORE II and ERA-Interim runs which have a similar pattern to each other.

Figure 5.5 is a map of the January 2007 ORCA025-N206 surface damping, while Figure 5.6 is a map of ORCA0083-N001 surface damping in the same month. These figures show how the 1/12° ORCA0083-N001 run has a much greater damping that happens at the Siberian shelf seas and in the Beaufort Sea. This happens because of an incorrect formulation of the forcing in the ORCA0083-N001 run, explained in section 5.8.1. Figures 5.7-5.13 illustrate the liquid heat balance in the different model runs. Figure 5.7 shows the monthly boundary flux while Figure 5.8 shows the monthly surface flux. The surface flux is characterised by having a greater interannual variability as the standard deviations are higher than in the boundary fluxes. The greater range of the surface flux means that it has a greater short-term affect on the change in heat content.

The different model runs show a greater correlation in the surface flux than the boundary flux, though ORCA0083-N001 has a higher average value, as shown in the seasonal average plots, Figures 5.9 and 5.10, though they show the same trends. Figure 5.9 shows that the greatest boundary inflow of heat in each run happens in October, which is discussed in section 5.8.2. Figure 5.10 shows that the surface flux is only positive (heat going into the region) between May and September, peaking in July at 400 ± 20 TW in the different runs, while the greatest loss of heat occurs in October at -500 ± 100 TW. In contrast Figure 5.9 shows the boundary flux always has a net input of heat into the region, though this fluctuates with the highest level of heat input happening in October and the lowest level happening in May, ranging from 75 ±25 to 175 ± 25 TW in the different model runs over the year.

The boundary fluxes vary more between the different runs, with the short 1/4° CORE-II run in Figure 5.7 having a lower influx, or positive boundary flux, of heat at the start of the run while the 1/12° ORCA0083-N001 run has a greater influx than the other runs. This is reflected in the annual average graph, Figure 5.11, which shows that the 1/12° run has a fairly similar pattern to the 1/4° run with a matching increase in 1990 and a reduction in 1996, but with an offset of about 25 TW like the surface flux, while the short 1/4° CORE-II run only reaches the same state as the other 1/4° runs after about 10 years, initially having a lower flux. The same behaviour is shown in the annual surface heat flux graph, Figure 5.11. The initial divergence of this run before it converges with the other 1/4° runs is discussed in section 5.8.2.

The overall heat imbalance for the four runs ranged between -2.4 TW and -3.5 TW, the negative sign meaning that there is extra heat being exported that is not completely accounted for. The 1/12° result shows a similar pattern in Figure 5.13 to the 1/4° runs except for the period 1991-1996 where it has a

significantly greater negative value. The short run CORE-II has two spikes, one in 1996 and one in 2003 that do not fit the pattern of the other runs and have a much larger excess of heat than the rest of that run. This would mean that in these years there is an increase in the amount of heat unaccounted for in the calculations. These coincide with anomalous points in the data series. Attempting to reproduce the averaged data sets for these points showed that these data points were flawed, but they have been left in the plot.

The solid component of the heat budget shows a similar pattern of peaks and trough in the timeseries between the different runs but less correlation in the absolute values. The latent heat boundary flux has large fluctuations between different months and years (Figures 5.14, 5.18) but the overall seasonal cycle (Figure 5.16) shows a maximum outflow of heat in March and a minimum in August that approaches zero as the ice around the boundary of the Arctic Ocean melts. The short CORE-II run tends to have higher values of outflow during the winter months than the other runs. The surface latent heat (Figures 5.15, 5.19) is ten times larger than the boundary flux, and has a regular annual variability, with heat input into the Arctic of decreasing on average by 1 TW each year in each run. The seasonal cycle for this (Figure 5.17) is positive in the summer with an average maximum monthly inward transfer of 700 TW, where heat is transferred to the region, and negative in the winter, with an average maximum monthly outward transfer of -350 TW. The summer positive period is shorter than the negative as it only lasts for four months but it peaks more sharply as its maximum value at July is greater than the winter minimum, which settles consistently for three months. The sensible heat component is very small relative to the other terms but is not negligible, with an average value of 4 TW during the winter (Figure 5.20). This decreases to

zero during the summer. The transport of ice results in an overall increase of heat in the system relative to the 0°C reference temperature.

Adding the solid and liquid components of the boundary flux together (Figure 5.21) results in a seasonal cycle that maintains the shape of the seasonal liquid heat boundary flux (Figure 5.9) but is flatter and ranges between 90 ± 20 and 190 ± 20 TW during the year for the different runs. The sum of the surface and boundary fluxes from equation (5.20) shows storage (Figure 5.23), as the summation of the three components of surface flux, boundary flux and content change equals zero. Figure 5.22 shows the sum of the liquid flux terms, which are the same terms as in Figure 5.13 without the estimated storage calculation included. The boundary and surface fluxes were calculated on the monthly mean datasets, so the removal of the annual storage estimation permits the creation of a seasonal cycle graph of the liquid heat storage. This shows that a large amount of heat in the order of 500 TW is stored in the summer and then removed in the winter, with the net effect being a small loss of heat in the 1/4° runs of 3 TW over the year, while the 1/12° run has a gain of 14 TW. The inclusion of the solid boundary flux into the sum of the fluxes (Figure 5.23) shows that there is a storage of heat in the ocean every year, though the amount being stored is on average gradually decreasing every year in the longer model runs (ORCA025-N206, ORCA0083-N001), though this trend is influenced by the more variable storage amounts before 1990. The seasonal cycle of the solid and liquid flux terms (Figure 5.24) looks almost identical to Figure 5.22 and shows that there is an overall increase in heat storage as it gains heat from April to September and loses heat for the rest of the year, most notably in October. The mean heat storage for the four runs is 39 TW, the implications of which are discussed in section 5.8.2.

The freshwater graphs show greater variation between the different model runs than the heat graphs. The monthly boundary flux (Figure 5.25) shows that there is a seasonal pattern but it is highly variable between months from different years. The seasonal average (Figure 5.27) shows how these variations average out, with the main peak in outflow happening in June.

The annual average freshwater boundary flux (Figure 5.30) is consistent at 90 mSv outflow in two of the runs, the long CORE-II run and the ERA-Interim run. The short CORE-II run initially has a much smaller outflow but still shows a similar pattern with the offset value, before eventually reaching a more stable value that coincides more with the other 1/4° runs. The 1/12° run has a much greater outflow of freshwater, instantly diverging from the 1/4° from a similar initial value in 1981, while showing reductions in the outflow that coincide with the 1/4° runs in 1998, 2004 and 2007.

The surface freshwater flux (Figure 5.26) is more sharply defined with a huge downward inflow that happens in the summer, before returning to a net outflow in the winter. The 1/12° DFS4 run has a summer inflow of 2500-3000 mSv and a winter outflow of -900 mSv, while the 1/4° runs are similar to each other with summer inflow of 1300-1700 mSv and winter outflow of 700 mSv, so the DFS4 forced run has a greater range. The annual graph (Figure 5.29) shows that the 1/4° runs have similar peaks and troughs and magnitude, at an average of 90-110 mSv. The 1/12° run is substantially different in terms of its magnitude and range, though it too has broadly the same timing of peaks and troughs as the 1/4° runs. The amount of the 1/12° surface flux inflow decreases after 1991 to a value that is closer to the 1/4° surface flux, but the inflow is still 50 mSv more than the 1/4° runs during this time.

The overall average FW storage (Figure 5.31) is -88 mSv, with the three 1/4° runs showing a similar pattern and similar values over the time period of the short runs, 1990-2007. The storage (Figure 5.32) has been corrected for the damping term to give the surface freshwater flux purely from evaporation, precipitation, river run off and ice melting and formation. This loss of freshwater is due to warm, salty water being imported and cold, fresher water being exported.

The graph of the monthly volume boundary flux (Figure 5.33) shows that all the runs are of a similar magnitude but they frequently fluctuate and have very sharp, erratic peaks, which shows a lack of consistency in the monthly mass boundary transport between the different runs. This is explained in section 5.8.1. The annual graph (Figure 5.37) shows that the 1/4° runs are very similar except for one anomalous peak in the short CORE-II run. The 1/12° run is similar to the freshwater graph in that the initial flux is significantly different but this reaches a state that is similar to the 1/4° runs after 1991, and it shows a similar pattern to the long CORE-II run throughout.

The monthly surface flux (Figure 5.34) and the seasonal surface flux (Figure 5.35) are noticeable by how the 1/12° run differs in behaviour from the 1/4° runs that are very similar to each other. The general trend for the runs is for there to be a sharp increase in flux during the summer and a much reduced flux in the winter, but the 1/12° run has a smaller maximum flux and then a minimum flux that does not reach as close to zero, instead settling at 200 mSv, even after 1991. The annual surface flux graph (Figure 5.38) reflects this in that the three 1/4° runs have very similar and consistent values throughout and the 1/12° run does not coincide in any way.

Despite the contrasting results between the different resolution models, the volume imbalances (Figure 5.39) are remarkably very similar, and close to zero as a long-term average. Each run shows the same peaks and troughs in the imbalance as each other. Figure 5.40 plots the long CORE-II run as a sample volume imbalance against the individual components, as the runs all had similar results. It shows that the components are fairly consistent throughout the run, though as the average value of the content change is positive, the ocean storage is increasing by 11 mSv per year.

The mass storage plot (Figure 5.41) shows that the near-zero imbalance is achieved by having some months where there is storage (May, June, July, September, balanced by some months where the content decreases (January, March). The pattern is broadly due to the increase in surface flux in the summer that is then compensated for in the winter.

5.8 Discussion

Although there may be some correlation between the results of the different properties, each is looked at in turn, starting with the mass and how that has an effect on the other calculations. This is followed by a discussion on how the different components of the heat budget interact with each other and then finally the significance of the freshwater results.

5.8.1 Mass

The value of Figure 5.40 is to show the significance of the level of mass imbalance for the region, with the long CORE-II run used as an example. The comparison of the imbalance against the dominant flux terms shows the imbalance is at an average value of 0.3% of the flux values, which is an

estimate of the level of uncertainty described in Chapter 4. This is very small relative to the major flux quantities, which means that the results can be used with confidence. This is essential for the project to be able to contribute to our understanding of the Arctic.

The main noticeable difference between the runs was in the surface flux, where the 1/12° run had a less sharp peak in downward volume flux in the summer, by being spread out more smoothly over several months instead of almost only being a feature in June, as in the 1/4° runs. The 1/12° run also had a greater surface flux during the winter months in the order of 200 mSv, compared to the near-zero value in the 1/4° runs. A corresponding pattern exists in the boundary fluxes of the different models. The reason for the general shape of the graphs is the contribution of the surface flux, which contains evaporation, precipitation, river run-off and a restoration term. In the summer the ice starts to melt, including that on the land, which causes a large input of river water into the Arctic Ocean. During the winter when the rivers freeze over, the volume flux is significantly reduced to the small contribution from evaporation and precipitation. Although the Arctic circulation contains inflow from the West Spitzbergen Current, the Barents Sea Opening and Bering Strait, the overall transport is on the long term average always negative as the circulation has to remove the river input. Figure 5.33 shows that there were some months where the boundary flux was positive, at an average rate of once every two years and there was a net input into the Arctic. This means that there are occasions when the boundary flux increases the volume of the Arctic rather than pumping out the surface flux input.

The shape of the 1/12° surface flux can be explained by the damping restoration term. The restoration term is a virtual salinity flux that has the effect of adding freshwater to the system as a correction factor based on

climatology. In this case, the correction has resulted in the unusual behaviour where there is a greater surface flux in winter than expected from evaporation and precipitation, as run-off is small at this point. The correction takes place at the shelf seas (Figures 5.4, 5.5) as this is where the river outflows enter the ocean, so the damping is a method to correctly account for the large freshwater input that the rivers provide. It increases the surface flux by an extra 100 mSv in the version used in the 1/12° run compared to the 1/4° damping (Figure 5.3). This additional 100 mSv of water is then exported which causes the corresponding increase in the boundary flux. The effect of damping is most noticeable in the early period of the run, while it is reduced in strength post-1991 when the model atmospheric forcing was updated.

This run takes initial salinity and temperature values of the World Ocean Atlas (WOA) (Levitus et al., 1988), merged with the Polar Hydrographic Climatology PHC2.1 database (Steele et al., 2001) for greater accuracy at high latitudes, and damping is done by relaxing the sea surface salinity to the WOA monthly mean value. However this was inaccurate for the high latitudes, and it wasn't until this was corrected that a realistic damping was achieved by the forcing.

The correction for the boundary fluxes for the 1/12° run by equation (4.18) was found to have an average value of 25 mSv of additional outflow, which proved to be necessary to get the correct volume imbalance that matches the 1/4° run. The correction has a seasonal pattern in that it is greater during winter, and the value of the correction gradually increases over the duration of the 1/12° run, which suggests that the error perpetuates over time and the accuracy of calculations using the vertical scaling factor drifts. This calculated correction can be used as a basis to estimate the correction required for the heat and freshwater boundary fluxes.

The monthly boundary fluxes were more variable between the different runs than the surface fluxes (Figure 5.33). This is because the surface fluxes are governed by the atmospheric forcings, which maintain a relatively consistent annual forcing. The boundary fluxes depend on the interactions between the different cells at the boundaries however, and the calculated velocities between the cells are able to fluctuate more freely which means that over time the different runs will have different fluxes, while following the basic dynamics and maintaining sensible values.

5.8.2 Heat

The liquid heat component has its maximum inward surface flux in July (Figure 5.22), and its maximum outward surface flux in October. This means that the ocean is heated in the summer and cools in the winter, which is the expected result due to solar insolation. As the Arctic is at the high latitudes of the northern hemisphere, this seasonal effect is amplified as there is much less sunlight in the winter. The strongest cooling happens in October because the cooling causes ice to form, which acts as a barrier insulating the ocean from the atmosphere and after a certain amount of ice is formed the effect of the cold weather is mitigated. The overall mean surface flux of the four runs is a heat loss of 121 TW (Table 5.3), which as a net loss shows that as well as the response to the heat input by solar insolation, heat from other sources such as Atlantic Water is lost in the Arctic.

The annual surface flux is similar to the annual boundary flux, but the graphs of the seasonal cycle do not line up with each other like the volume flux seasonal cycles do. Also, on the monthly timescale there is a much greater standard deviation in the surface flux than there is in the boundary flux. The surface flux consistently varies between ± 450 TW while the boundary flux

only ranges from 200 TW to 400 TW. This shows that much of the input surface heat only remains at the surface and does not reach the deeper waters as it has little effect on the boundary flux. This would be due to the stratification of the Arctic Ocean inhibiting the transfer of heat, creating a warm surface mixed layer that is relatively shallow.

The boundary heat flux is greatest in October and lowest in April. October is when there is the greatest amount of cooling through the surface, so it might be that more heat is being lost through the surface rather than being exported through the boundary. It may be that there is a relaxation timescale in which the effect of the solar radiation takes time to have an effect on the boundary flux, as the net inward transport gradually reduces during the winter.

There is also a smaller heat signal on the maps from Bering Strait which brings a Pacific inflow all year round due to the greater sea surface height of the Pacific Ocean, though its influence is limited as the strait is narrow and has a cross-sectional area of 4×10^6 m^2 (Overland and Roach, 1987). It provides 10-20% of the oceanic heat input to the Arctic Ocean (Woodgate et al., 2012). The Bering Strait inflow is independent of any remnant Atlantic Water that has circulated past the Siberian shelves and towards the Beaufort Sea as the Atlantic layer in the Canada Basin is lower, fresher and colder than the Pacific originating middle halocline water (McLaughin et al., 2004).

All four runs were broadly similar to each other in regard to the liquid heat components, with the 1/12° run having greater boundary and surface fluxes and content change, though there was a greater disparity between the 1/12° and 1/4° boundary fluxes than the surface flux. A possible explanation could be the correction required for the 1/12° boundary flux due to the vertical

scaling of the model cells. As an estimation of the maximum contribution of the correction, the heat contribution C_{heat} is given by

$$C_{heat} = \rho\, C_p\, \Delta T\, C_v \qquad (5.24)$$

where density ρ = 1035 kg m^{-3}, specific heat capacity of water C_p = 4000 J kg^{-1}, ΔT is the temperature change, which is approximated to be the difference between an inflow of 4°C and an outflow of 0°C, and C_v is 30 mSv of outflow. This results in a boundary flux correction of 0.5 TW which is small relative to the 38.5 TW of heat storage (Figure 5.24). The result of Tsubouchi et al. (2012) from the inverse modelling of observed data shows a summer 2005 liquid contribution of 170 ± 25 TW to the overall heat boundary flux, which is in line with the average boundary flux of Figure 5.7. The observation-based latent and sensible heat boundary flux is 19 ± 5 TW, which matches with the latent boundary flux of Figure 5.14 (after a reversed sign convention).

The solid latent heat flux is the removal of heat by ice formation from the surroundings, including the ocean. It must be noted that since the ice is colder than the reference temperature of 0°C, the sign of this would be positive for ice formation but in order to maintain the same sign convention as the liquid components where a positive surface flux is input into the system, the surface latent heat flux is negative during ice formation.

Sea ice is formed in the Arctic and then exported through the boundaries. The export is a consequence of the transfer of heat to the atmosphere, so in keeping with the convention for negative boundary fluxes being outflow, export of the ice is a positive boundary flux for latent heat. Also, as the ice is colder than the ocean the export represents a warming and is therefore also a positive sensible heat boundary flux.

The latent heat surface flux (Figure 5.17) has a strong seasonal cycle that regularly occurs over the duration of the model runs (Figure 5.15), and the different runs all have very similar results. There is a peak of positive flux during the summer when ice melts which reaches a maximum in July, while there is a negative flux during the winter from September to May as ice formation happens. The value remains consistently around -300 TW between October and March. The boundary latent heat flux approximately balances with the surface latent heat flux over the annual cycle, but the boundary transport has a greater interannual variability. Like the liquid heat components, the surface latent heat peaks for a small part of the year with more extreme values than the boundary latent flux but the boundary flux has a smoother seasonal curve that reduces to close to zero at August. The boundary flux reaches its minimum in March, though the estimations vary between 40 TW in the ERA-Int run to 80 TW in the short CORE-II run. This is a much smaller magnitude than the 700 TW surface latent heat maximum. The different runs show the similar patterns in the annual timeseries but at different levels of offset. The two runs of CORE-II are almost exactly the same as each other after the spin up period of the short run, but have an offset from the ERA-Int run while showing almost exactly the same pattern. The 1/12° run does not have exactly the same pattern but is close and has a value between the two different atmospheric forcings of the 1/4° runs.

The latent heat boundary flux is generally never positive over the long averaging period as ice is only exported from the Arctic, not imported. The consistent but small boundary flux through winter and the almost zero value in summer shows that the ice export rate remains at a fixed rate during winter but not all of it is exported and the vast majority of formed sea ice remains in the Arctic Ocean, where it melts in the summer.

This study does not investigate the ice residence timescale, as it is not necessarily the case that the ice that has just been formed is the same ice that melts or is exported over the course of a year. This is evident from the interannual variability of the monthly boundary latent heat flux being much greater than that of the surface latent heat flux.

The sensible heat boundary flux is a small quantity that is close to zero but non-negligible. The export only has much of a signal at 4 TW between January and March once the ice has formed and is being exported, while it is zero from June to September. The latent heat boundary flux has a very small export during summer, but this must be too small to have a corresponding sensible heat boundary flux at this time.

Adding the solid and liquid components of the boundary flux together (Figure 5.21) creates a seasonal cycle that maintains the shape of the seasonal liquid heat boundary flux (Figure 5.9). This is because the latent heat boundary flux comes from ice export and occurs in the winter when there is ice formation, while the liquid heat boundary flux occurs in the summer and autumn when there is less ice and more liquid transport (Figure 5.34).

The adding together of the solid and liquid heat components gives the total heat storage of the system. Figure 5.23 is the annual trend and there is a gain of stored heat in the ocean every year, though the amount of heat being stored steadily decreases every year. The seasonal cycle of the solid and liquid fluxes (Figure 5.24) looks almost identical to the liquid flux sum. The similar shape of the graph is due to the dominance of the surface flux magnitude compared to the boundary fluxes. The mean storage of the four runs is 39 TW per year which means the Arctic Ocean is warming up. Using equation (5.24) to obtain ΔT, and taking an estimate of the Arctic Ocean volume of 18.75×10^6 km^3

(Eakins and Sharman, 2010), this corresponds to a heat storage distributed over the whole Arctic of 0.06°C per year.

5.8.3 Freshwater

The freshwater surface fluxes are generally defined by a large peak in July (Figure 5.28) and is positive from May to September, though in the CORE-II forced runs this peak is smaller and flattens between June and July. This peak is between 1500 mSv in the CORE-II runs and 2500 mSv in the 1/12° run. During winter the flux is a consistent 600 mSv, but over the course of the year the average surface flux is 200 mSv. As well as having a higher peak flux, the 1/12° run has a larger negative flux than the other runs in the post-1991 period. The positive summer flux is from ice melt, which has a lower salinity than the ocean, and river runoff, which is fresh, while the winter negative flux results from the freezing of ice.

The boundary fluxes are much less variable over the course of the year, though there is a greater interannual variability. The 1/4° runs have a good agreement of 65 mSv of outflow, though the short CORE-II run is impacted by the spin-up period and only matches up well after 2000. The 1/12° run is substantially different with a much greater outflow of 170 mSv. The estimation of the correction required for the freshwater advection is

$$C_{fw} = \left(1 - \frac{\Delta S}{S}\right) C_v \qquad (5.25)$$

where ΔS is the difference in salinity between the cell value S and the reference value of 34.8, and C_v is the imbalance. As the ΔS term is relatively small it is necessary to calculate the correction for the salinity of each individual boundary section and add the total together. This gave a result of approximately 30 mSv of outflow, which is to be expected since that was the

mass correction, though it does have some variability across different years. Applying this methodology did not lead towards a more reasonable calculation of the imbalance.

The surface flux (Figure 5.28) in the summer is a huge amount of freshwater above the background level of the precipitation and evaporation that is being added to the system, because it is predominantly through river runoff (section 2.1). This water will be added to the ocean at the river mouths on the coast and may cause a local increase in sea surface height due to the rate at which it is added. This could then lead to a geostrophic response which will cause the water to turn to the right and circulate over a period of time. This time would result in a delayed response from the boundary fluxes to be able to export this freshwater. As the seasonal cycle shows that this happens within the year, the ocean has a fast barotropic response to the river runoff, while the long term trend of content accumulation and storage is more of a baroclinic response. The effect of the river run off is to create a charge cycle that gains mass from May to September and eventually discharges as a boundary flux from January to March. As an estimation of the water being built up between May and September, a 4 month period with approximately 10^5 m^3 s^{-1} of inflow, this is a build up of 10^{12} m^3 or 1000 km^3 of water from the Siberian rivers. The water that is transported out within the year is not necessarily purely the water that has been added by the rivers; it is that the rivers have increased the overall local volume of water. The mean residence time of the river run-off on the Siberian shelf sea is 3.5 years (Schlosser et al., 1994). The small October peak is the marking of a reduction in the freshwater boundary flux as some of the freshwater starts to go towards forming ice.

By purely adding the seasonal cycles of the boundary and surface fluxes and ignoring the content accumulation, the sum should create an approximately

flat line if the two quantities instantly compensated each other. The freshwater balance should have some similarities with the mass balance because they have the same surface flux aside from the damping, but the effect of the salinity on the boundary fluxes might cause the freshwater balance to be out of phase as there is the lag time between the large surface freshwater flux reaching the boundaries from the rivers.

The sum of the mass seasonal cycles is close to zero, but is generally positive in the summer between May and September and negative in the winter which shows that it takes some time for the summer river flux to spread across the ocean and reach the boundaries. The freshwater flux sum (Figure 5.32) shows that once damping is corrected for, the 1/12° graph is substantially different from the 1/4° graphs, with some small similarities in the trend but the magnitudes are different which suggests that something is missing from this formulation, especially with the summer peak input of freshwater. The 1/4° runs show yearly freshwater loss while the 1/12° run suggests that freshwater is being added to the Arctic; however Rabe et al. (2014) and Giles et al (2012) found that storage was increasing since 2000 years while there was decline previously. None of the graphs show this change in system, suggesting that something has been missed in the execution of this calculation. Rabe et al. obtained a value for the increase of 600 $\pm$ 300 $km^3\,yr^{-1}$ which is 19 mSv. This is a lower change than the estimate from the runs in Figure 5.31, which had an average of 88 mSv loss.

This chapter has investigated the heat, freshwater and mass of the model definition of the Arctic Ocean. It has shown that there is a large amount of heat brought in through advection that is lost via surface radiation to leave a small net warming of the ocean. The main variability occurs at the surface but these processes have an effect deeper into the ocean as they penetrate into

deeper layers to produce a diluted response from boundary transports. The large input of surface freshwater from ice melt in the summer results in a delayed response in the boundary fluxes. Different atmospheric forcings and resolutions have been tested and these have produced broadly similar results except for the first part of the DFS4 run, which was adversely affected by an incorrect forcing field. This shows that the choice of field can have a significant effect on results if it is inaccurate. The next chapter will investigate the surface heat loss in greater detail to examine where in the Arctic Ocean this takes place.

5.9 Tables and figures

Table 5.1: Mean oceanic heat budget for the whole Arctic in different model runs. Values are in TW, sign is positive into the region. Fluxes are monthly averages and content change and imbalance are annual averages.

Model Run	Liquid heat boundary flux	Liquid heat surface flux	Liquid heat content change	Liquid heat imbalance
ORCA025-N206	121.2 ± 44.0	-122.7 ± 271.7	2.1 ± 13.0	-3.5 ± 1.2
ORCA025-N206 Valor	101.3 ± 45.4	-105.0 ± 260.5	-0.4 ± 13.7	-2.4 ± 2.1
ORCA025-N206 ValorERA	113.4 ± 37.2	-120.3 ± 312.2	-3.9 ± 9.0	-2.9 ± 1.2
ORCA0083-N001	149.5 ± 40.9	-135.2 ± 340.2	17.6 ± 14.9	-3.3 ± 2.0

Table 5.2: Mean solid heat budget components for the whole Arctic in different model runs. Values are in TW, sign is positive into the region. Advection and flux are monthly averages and content change and imbalance are annual averages.

Model Run	Solid latent heat boundary flux	Solid sensible heat boundary flux	Solid latent heat surface flux
ORCA025-N206	40.5 ± 26.9	1.7 ± 1.8	-39.6 ± 319.5
ORCA025-N206 Valor	41.6 ± 29.9	1.3 ± 1.3	-35.2 ± 321.8
ORCA025-N206 ValorERA	26.4 ± 18.8	1.7 ± 1.8	-21.9 ± 384.7
ORCA0083-N001	34.9 ± 21.4	1.7 ± 1.8	-35.1 ± 360.0

Table 5.3: Totals of monthly average surface and boundary flux components. Values are in TW, sign is positive into the region.

Model Run	Boundary fluxes	Surface fluxes	Total storage (+ve is gain in storage)
ORCA025-N206	163.5 ± 38.8	-122.7 ± 271.7	40.8 ± 246.9
ORCA025-N206 Valor	142.4 ± 40.0	-105.0 ± 260.5	42.4 ± 226.5
ORCA025-N206 ValorERA	141.0± 24.1	-120.3 ± 312.2	20.8 ± 305.6
ORCA0083-N001	186.1 ± 31.9	-135.2 ± 340.2	50.9 ± 324.3

Table 5.4: Mean freshwater (FW) budget for the whole Arctic in different model runs. Values are in mSv, sign is positive into the region. Fluxes are monthly average and content change and imbalance are annual average.

Model Run	Liquid FW boundary flux	FW surface flux	Liquid FW storage
ORCA025-N206	145.4 ± 278.4	90.9 ± 783.7	-214.1 ± 277.4
ORCA025-N206 Valor	184.9 ± 301.0	86.6 ± 785.7	-210.6 ± 300.5
ORCA025-N206 ValorERA	164.6 ± 224.2	112.6 ± 883.1	-230.0 ± 224.5
ORCA0083-N001	153.3± 280.3	202.5 ± 1072.6	-322.4 ± 271.1

Table 5.5: Mean volume budget for the whole Arctic in different model runs. Values are in mSv, sign is positive into the region. Fluxes are monthly averages and content change and imbalance are annual averages.

Model Run	Boundary flux	Surface flux	Content change	Imbalance
ORCA025-N206	-167.5 ± 217.0	177.9 ± 182.0	11.0 ± 17.3	-0.5 ± 12.8
ORCA025-N206 Valor	-162.7 ± 234.7	164.6 ± 179.1	3.5 ± 20.9	-0.9 ± 13.3
ORCA025-N206 ValorERA	-179.9 ± 175.6	164.7 ± 138.7	-13.8 ± 12.9	-1.4 ± 10.6
ORCA0083-N001	-283.8 ± 204.7	283.6 ± 127.7	1.5 ± 16.7	-1.7 ± 15.4

Table 5.6: Mass equivalent volume budget for the whole Arctic in different model runs. Values are in kT s^{-1}, sign is positive into the region. Fluxes are monthly averages and content change and imbalance are annual averages.

Model Run	Boundary flux	Surface flux	Content change	Imbalance
ORCA025-N206	−173.2 ± 224.4	183.9 ± 188.2	11.4 ± 17.9	−0.5 ± 13.2
ORCA025-N206 Valor	−168.2 ± 242.7	170.2 ± 185.2	3.6 ± 21.6	−0.9 ± 13.8
ORCA025-N206 ValorERA	−186.0 ± 181.6	170.3 ± 143.4	−14.3 ± 13.3	−1.4 ± 11.0
ORCA0083-N001	−293.4 ± 211.7	293.2 ± 132.1	1.6 ± 17.3	−1.8 ± 15.9

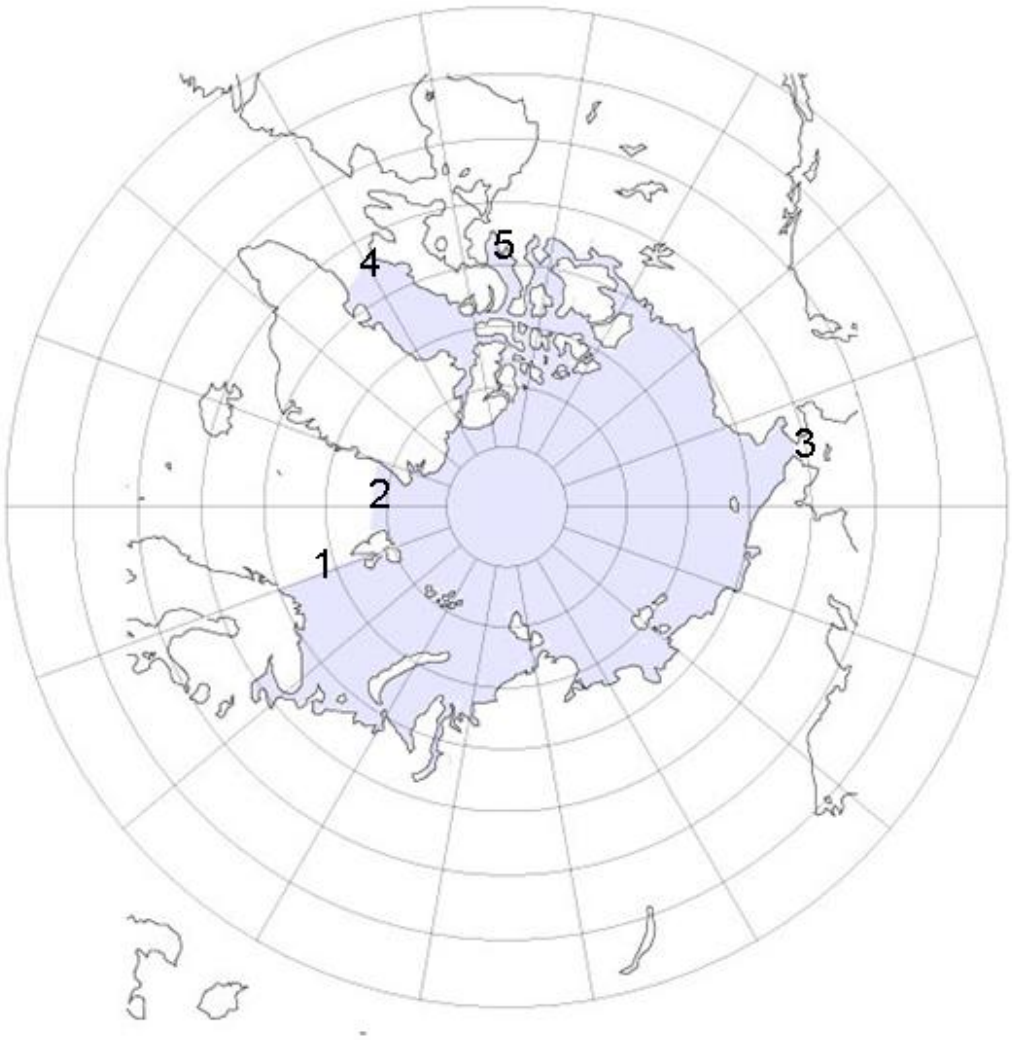

Figure 5.1 – Map of model detailed Arctic Ocean area (grey), with entrances at 1) Barents Sea Opening, 2) Fram Strait, 3) Bering Strait, 4) Davis Strait and 5) Fury/Hecla Straits.

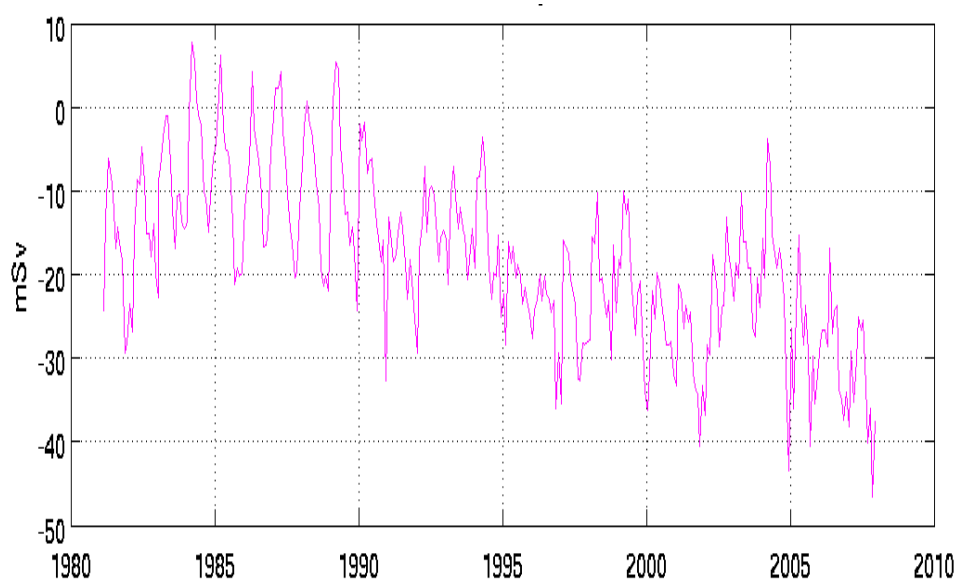

Figure 5.2 – Monthly ORCA0083-N001 sections SSH^2 graph for vertical scaling correction.

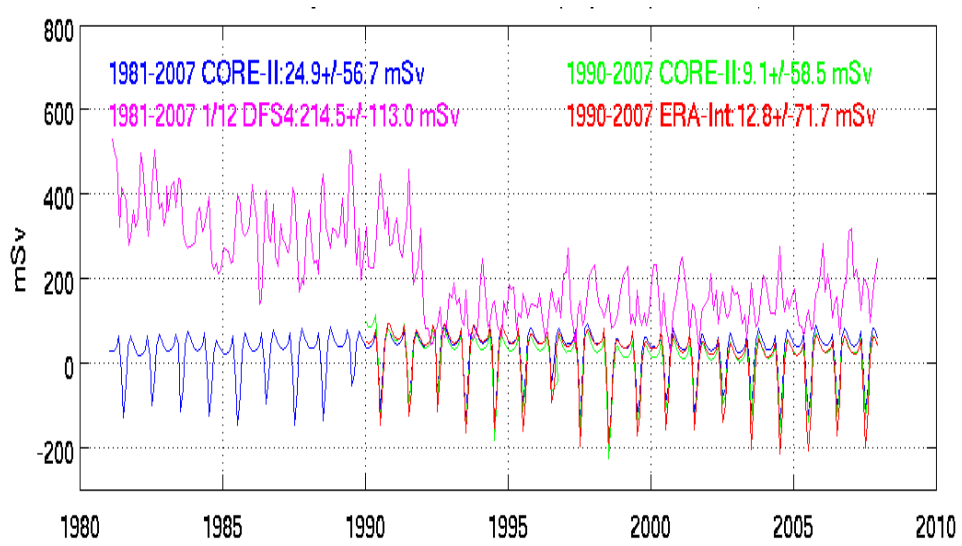

Figure 5.3 – Monthly Arctic Ocean damping graph. The discontinuity in the DFS4 plot is where the climatology was changed.

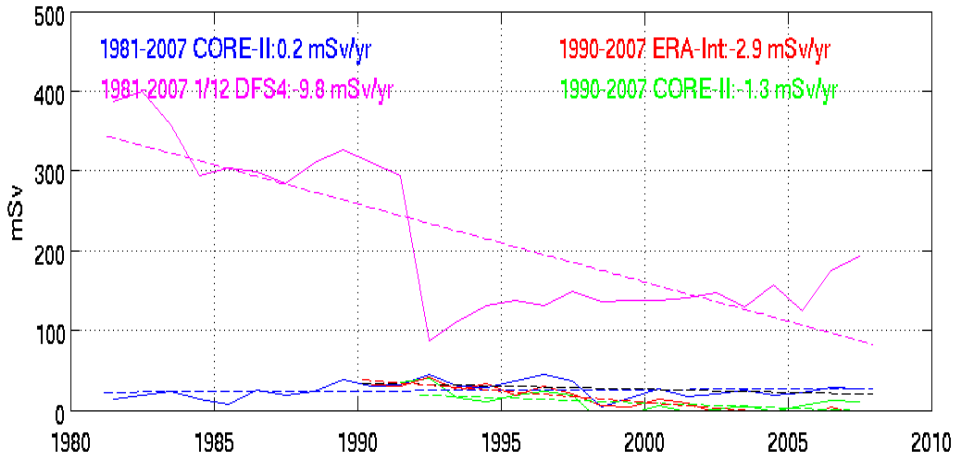

Figure 5.4 – Annual Arctic Ocean damping graph. The dashed line is a linear regression line and the values shown represent the annual trend. This shows the sharp drop in the damping of the DFS4 forcing field once the more accurate climatology is used.

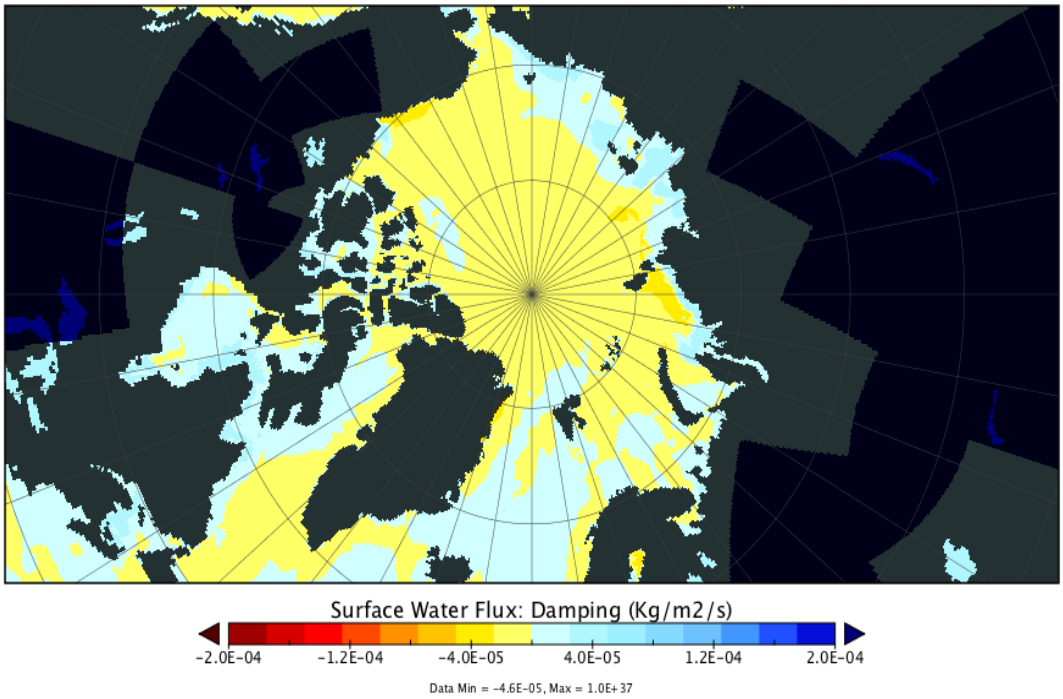

Figure 5.5 – CORE-II damping surface flux map (red is downward flux, input).

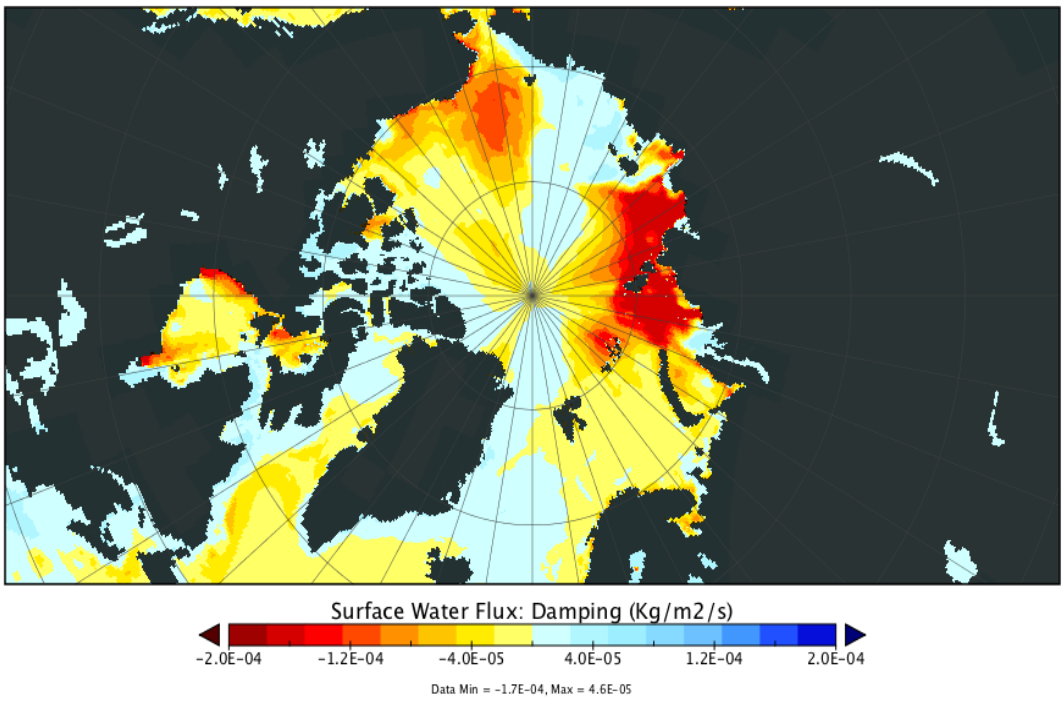

Figure 5.6 – DFS4 damping surface flux map (red is downward flux, input). The damping is over-represented at the shelf seas to compensate for sea ice formation.

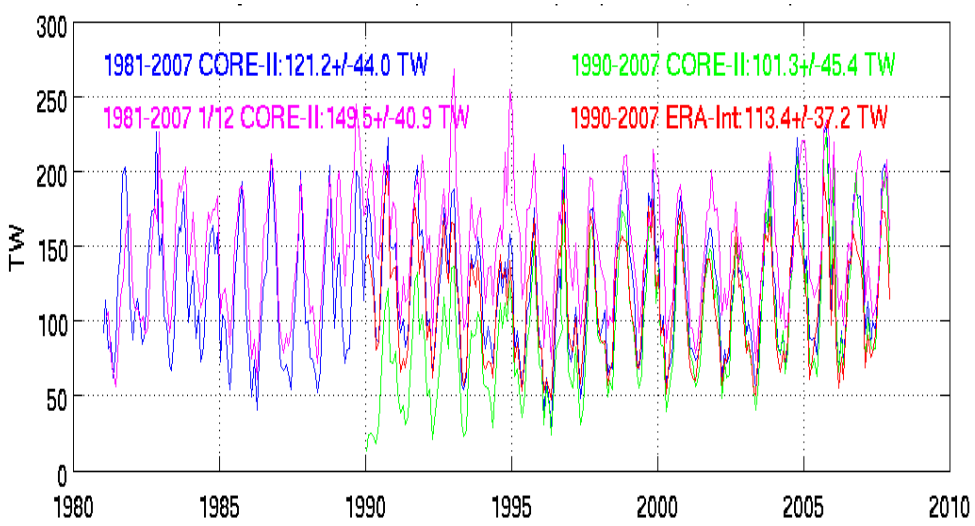

Figure 5.7 – Monthly Arctic Ocean oceanic heat flux boundary graph (+ve is inflow, warming), reference temperature 0°C.

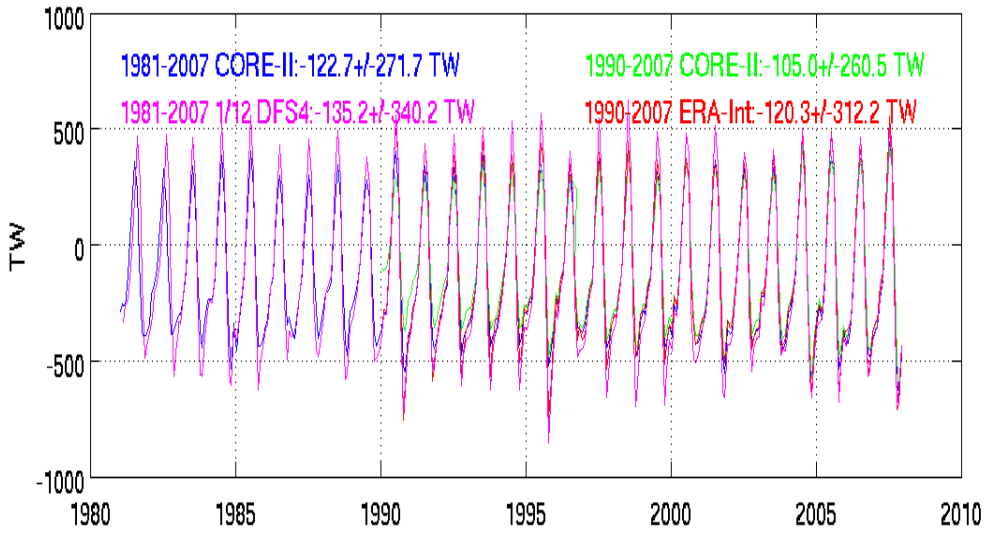

Figure 5.8 – Monthly Arctic Ocean heat surface flux graph (–ve is cooling, upwards), reference temperature 0°C. The surface fluxes have a greater range than the boundary flux, and the DFS4 ranges are greater than the other runs.

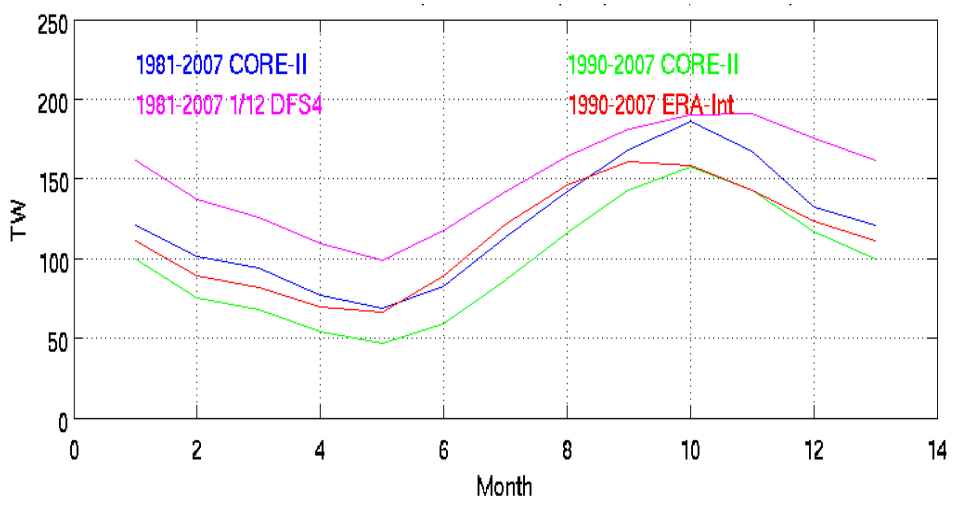

Figure 5.9 – Seasonal Arctic Ocean oceanic heat flux boundary graph (+ve is inflow, warming), reference temperature 0°C. Warm water is always on average advecting into the Arctic Ocean, peaking in October and at a minimum in May.

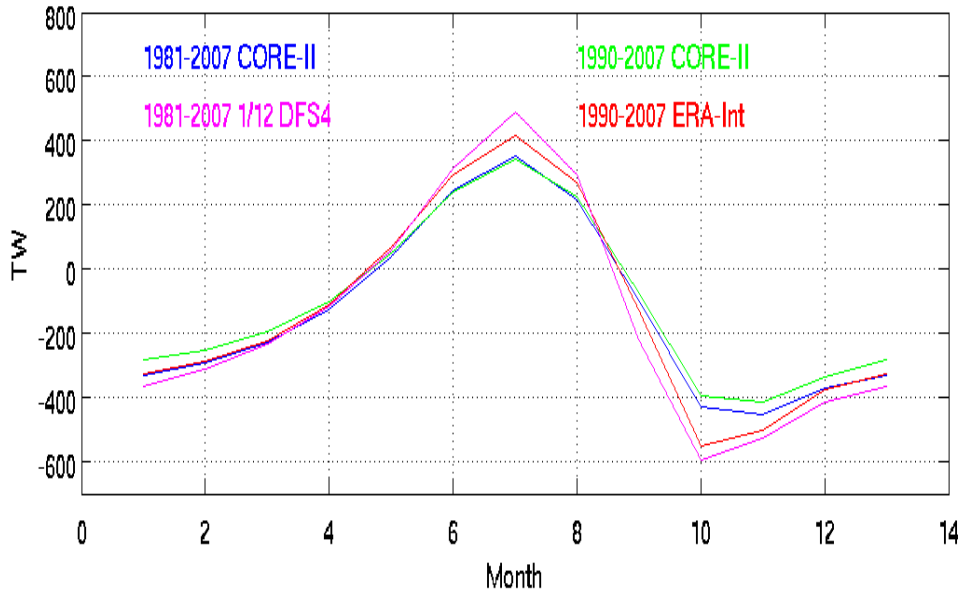

Figure 5.10 – Seasonal Arctic Ocean heat surface flux graph (–ve is upwards, cooling), reference temperature 0°C. Heat inflow is at a maximum in July due to greater solar insolation and at a minimum in October because sea ice eventually forms a shield against upward radiation in the colder winter months.

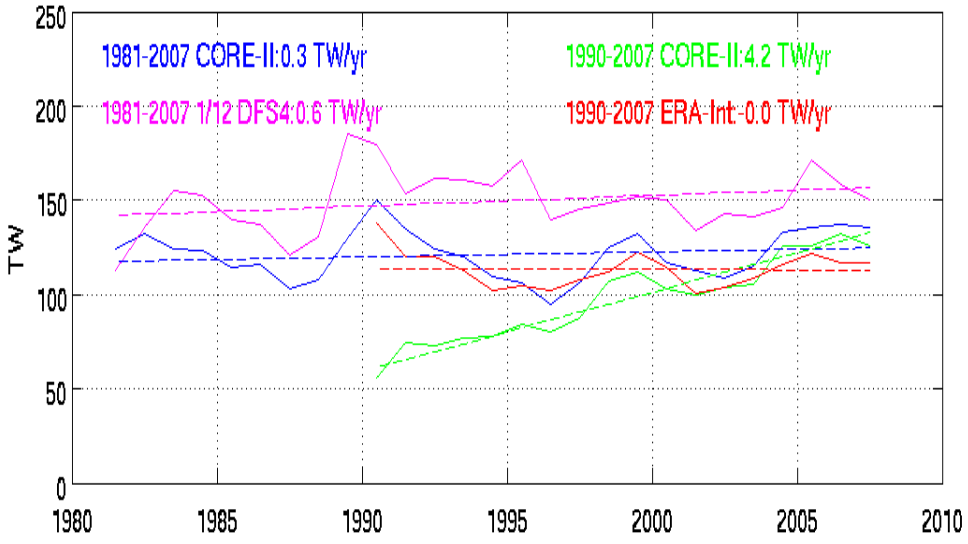

Figure 5.11 – Annual Arctic Ocean boundary oceanic heat flux graph (–ve is out, cooling), reference temperature 0°C. The dashed line is a linear regression line which shows that the average value does not change much over time, except for the short CORE-II run which has a low starting value that takes time to spin up.

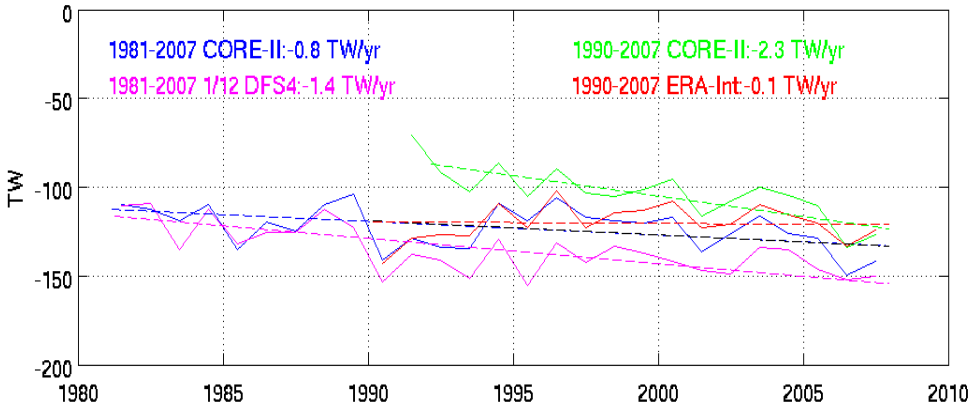

Figure 5.12 – Annual Arctic Ocean heat surface flux graph (–ve is upwards, warming), reference temperature 0°C. The dashed regression line shows that there is a small increase in heat being radiated out over time, generally greater than the increase in incoming heat from advection.

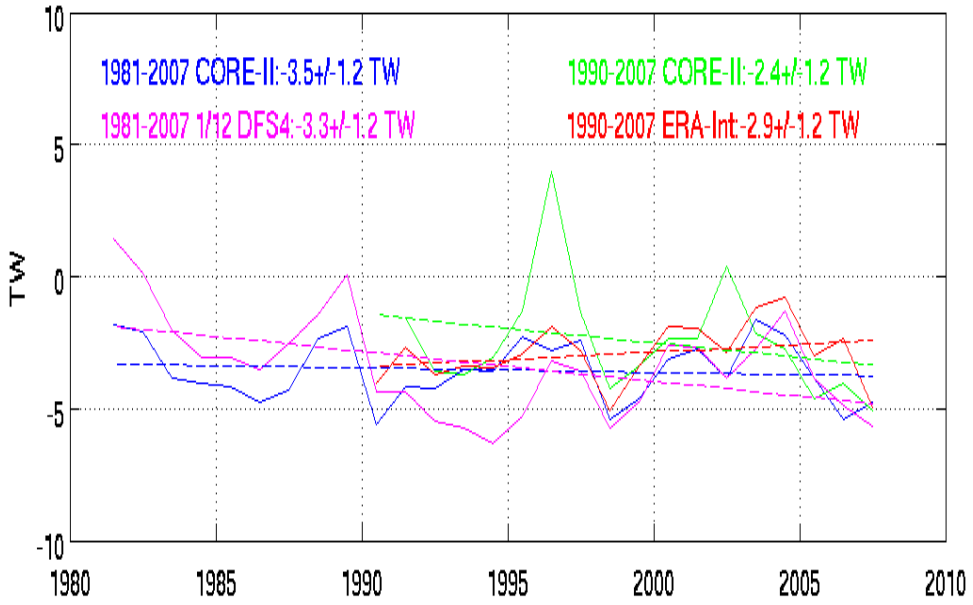

Figure 5.13 – Annual Arctic Ocean heat imbalance graph from liquid sources (+ve is excess). This shows that there is a shortfall of incoming heat in the budget as there is a net heat loss. Three of the runs (both CORE-II and DFS 4 show a trend of increasing shortfall.

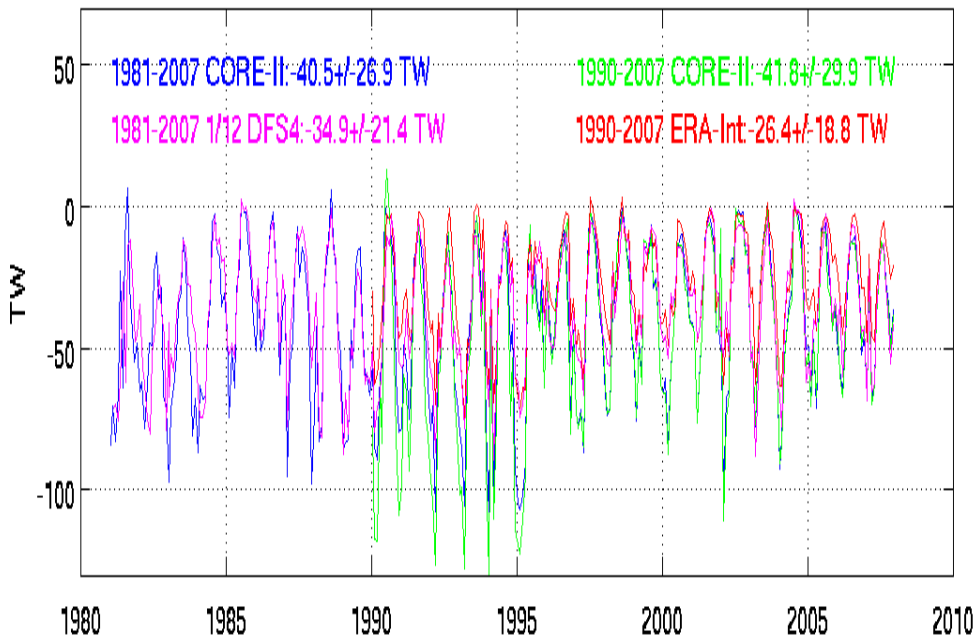

Figure 5.14 – Monthly Arctic Ocean ice and snow latent heat boundary flux graph (+ve is outwards, cooling), reference temperature 0°C.

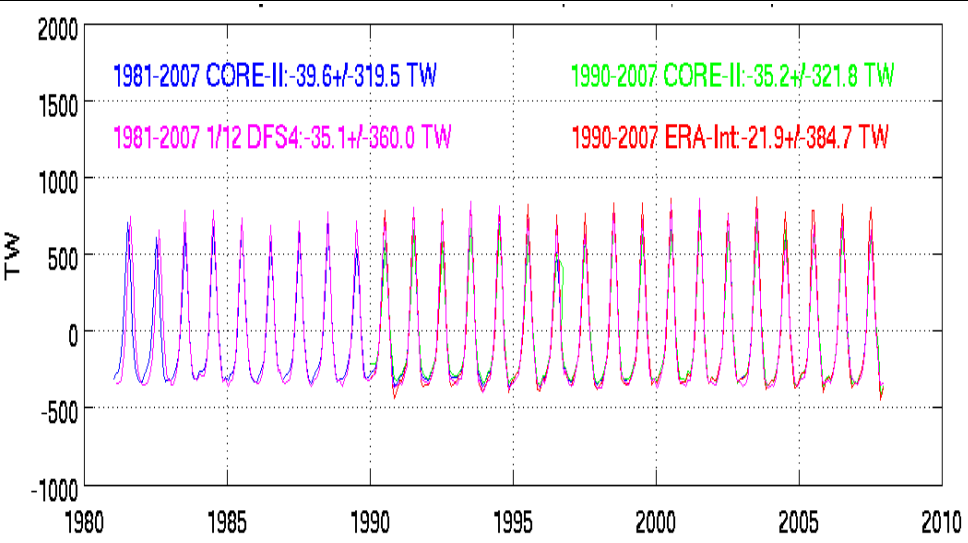

Figure 5.15 – Monthly Arctic Ocean latent heat surface flux graph (+ve is down, warming), reference temperature 0°C.

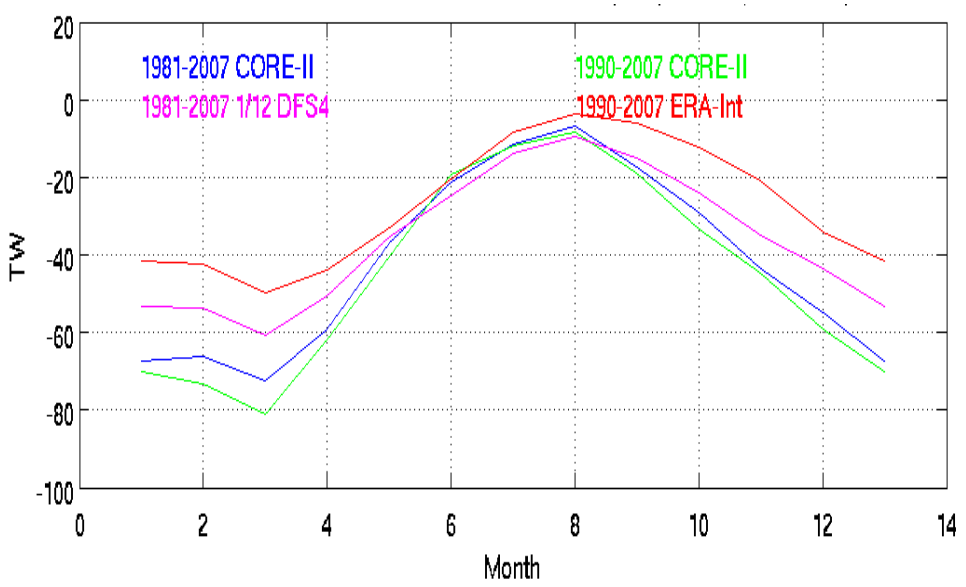

Figure 5.16 – Seasonal Arctic Ocean ice and snow latent heat boundary flux graph (–ve is outwards, cooling). Winter export of ice is a loss of heat as heat from the Arctic has contributed to ice formation.

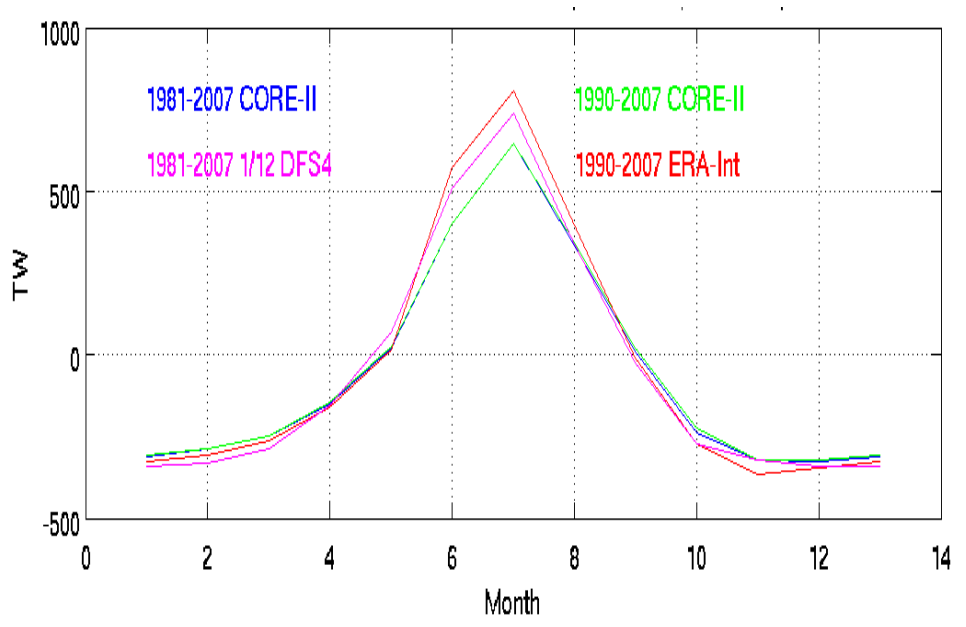

Figure 5.17 – Seasonal Arctic latent heat surface flux graph (+ve is down, warming), reference temperature 0°C. Flux is most positive in summer due to ice melting, peaking in July at 700 ± 50 TW, while it is most negative in winter, but at a more consistent value of –350 TW ± 20 TW over four months.

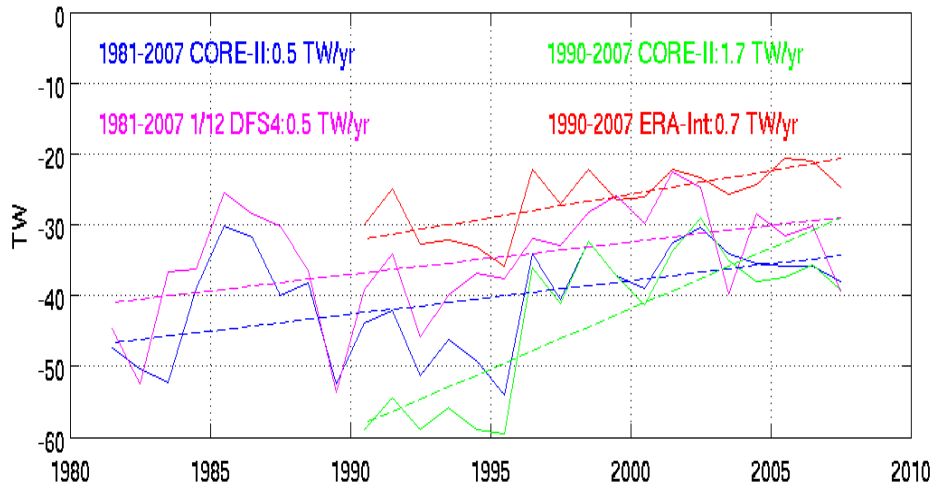

Figure 5.18 – Annual Arctic Ocean ice and snow latent heat boundary flux graph (–ve is outwards, warming), reference temperature 0°C. There is an offset between the different forcings but they show similar peaks and troughs, and the regression line shows that over time the flux is decreasing in magnitude.

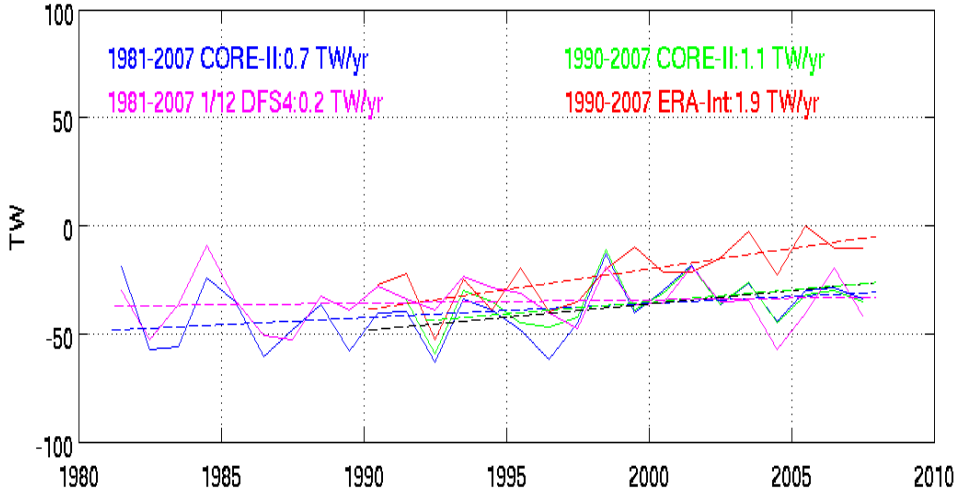

Figure 5.19 – Annual Arctic Ocean latent heat surface flux graph (–ve is upward flux, cooling), reference temperature 0°C. The trend is that less heat is being radiated over time.

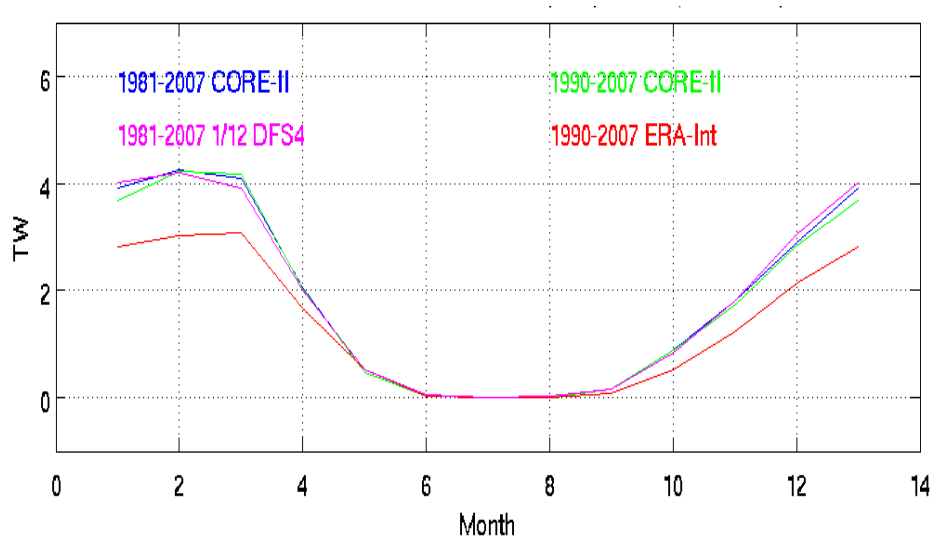

Figure 5.20 – Seasonal Arctic Ocean sensible heat flux boundary graph (-ve is outwards, warming), reference temperature 0°C. Heat is imported as cold ice below the reference temperature is exported. In the summer there is no ice export as the ice around the boundaries has melted.

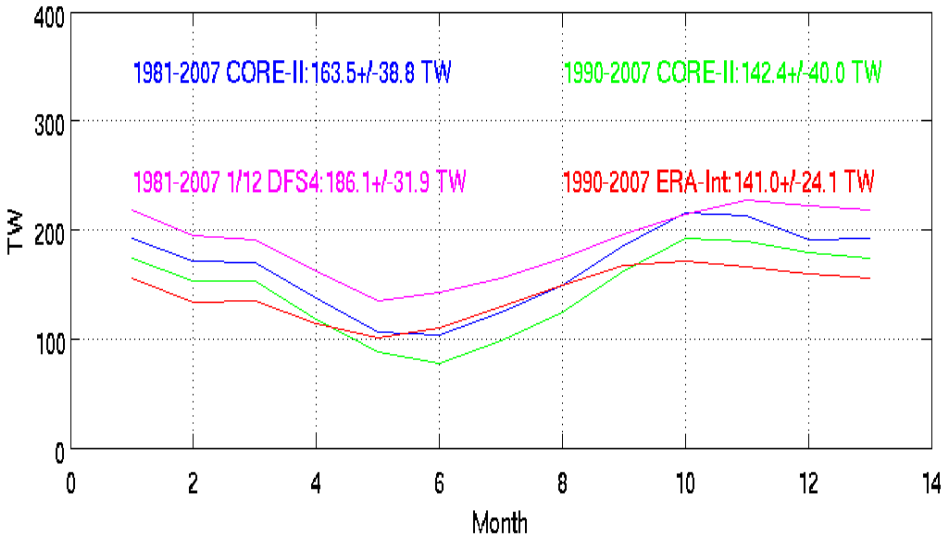

Figure 5.21 – Sum seasonal Arctic Ocean solid and liquid heat boundary flux graph (-ve is outward, cooling), reference temperature 0°C. This shows that heat is on average always being advected into the Arctic Ocean.

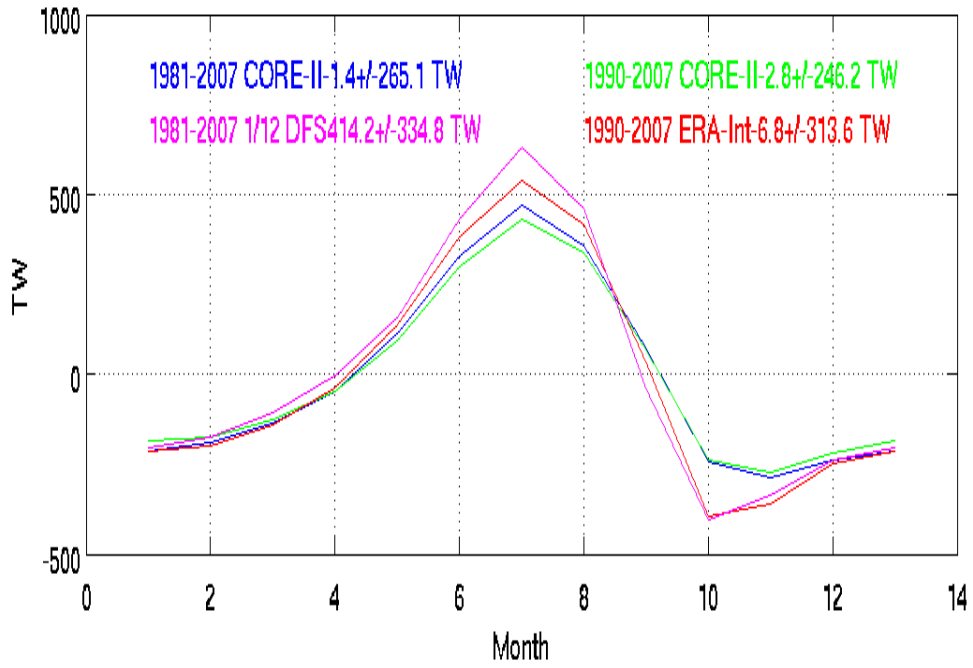

Figure 5.22 – Sum seasonal Arctic Ocean liquid heat boundary and surface flux graph (+ve is storage), ref. temp. 0°C. This shows that heat is stored in the summer and lost in the winter, principally due to surface fluxes. In the three 1/4° runs, there is net heat loss, while in the 1/12° DFS4 run, there is a net increase in heat stored in the Arctic.

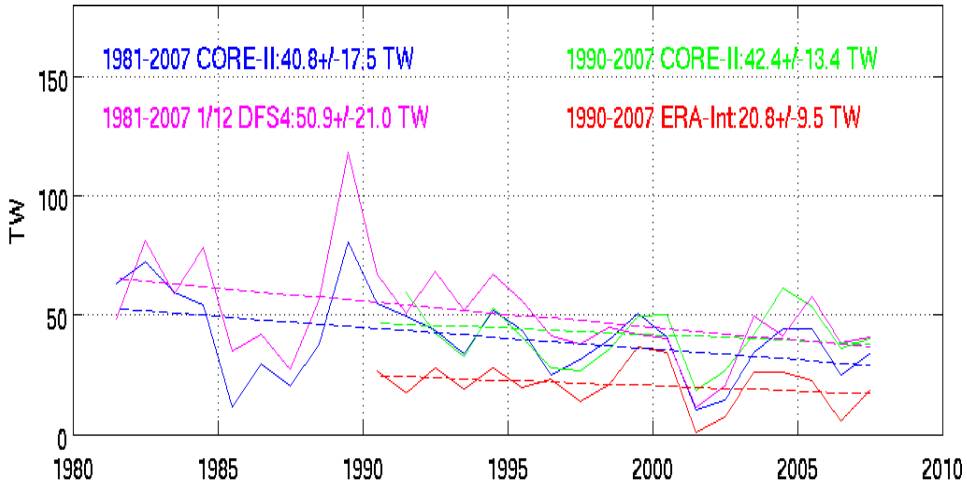

Figure 5.23 – Sum annual Arctic Ocean solid and liquid heat boundary and surface flux graph (+ve is storage), ref. temp. 0°C. This shows that when ice is included, there is a net increase of heat in the Arctic Ocean, though the trend is decreasing.

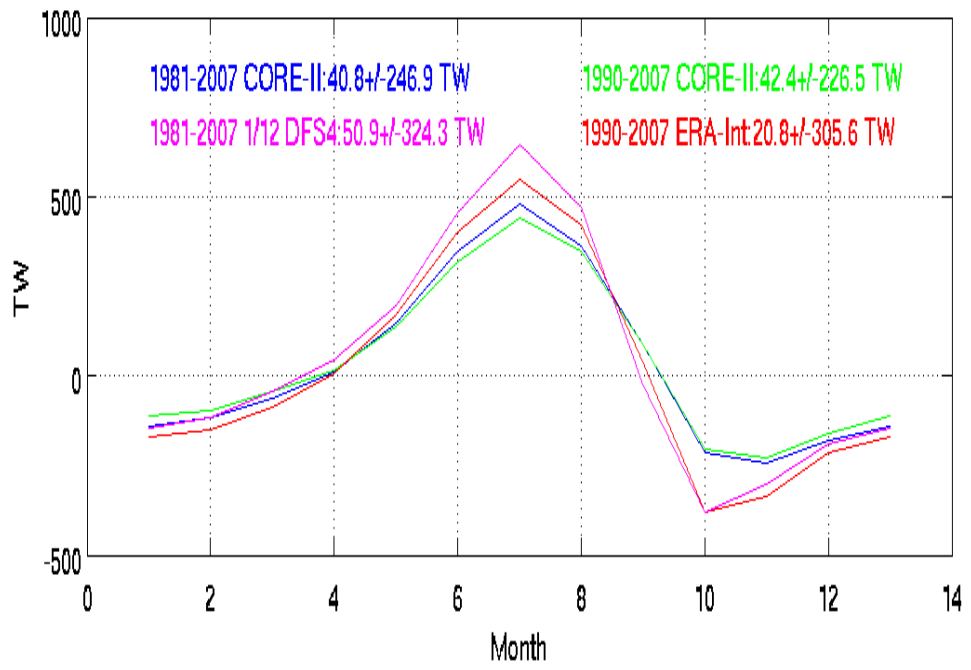

Figure 5.24 – Sum seasonal Arctic Ocean solid and liquid heat boundary and surface flux graph (+ve is storage), ref. temp. 0°C. The heat stored between April and September is greater than the heat lost between October and March.

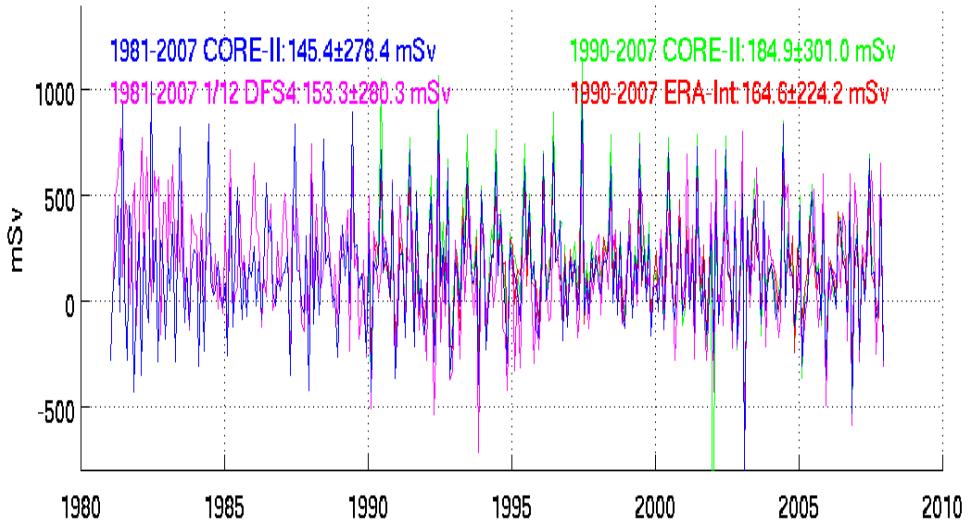

Figure 5.25 – Monthly Arctic Ocean liquid freshwater boundary flux graph (-ve is outward flow), reference salinity 34.8. This is highly variable over time as it responds to changes in rainfall which is variable and river output which produces large fluxes.

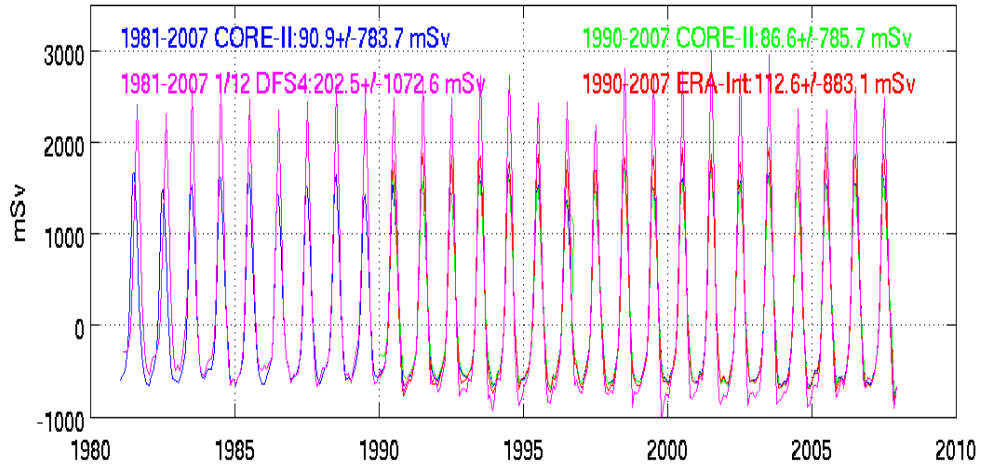

Figure 5.26 – Monthly Arctic Ocean liquid freshwater surface flux graph (+ve is down, inflow), reference salinity 34.8.

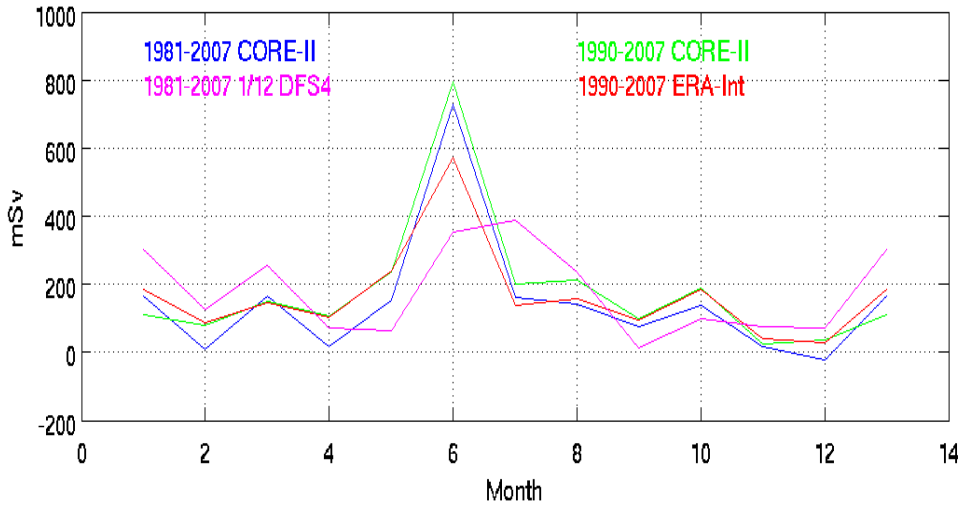

Figure 5.27 – Seasonal Arctic Ocean liquid freshwater boundary flux graph (+ve is outflow), reference salinity 34.8. There is a peak in June due to the removal of freshwater from sea ice melting. The DFS4 is more staggered in its flow as the damping affects how the freshwater from sea ice is added to the system.

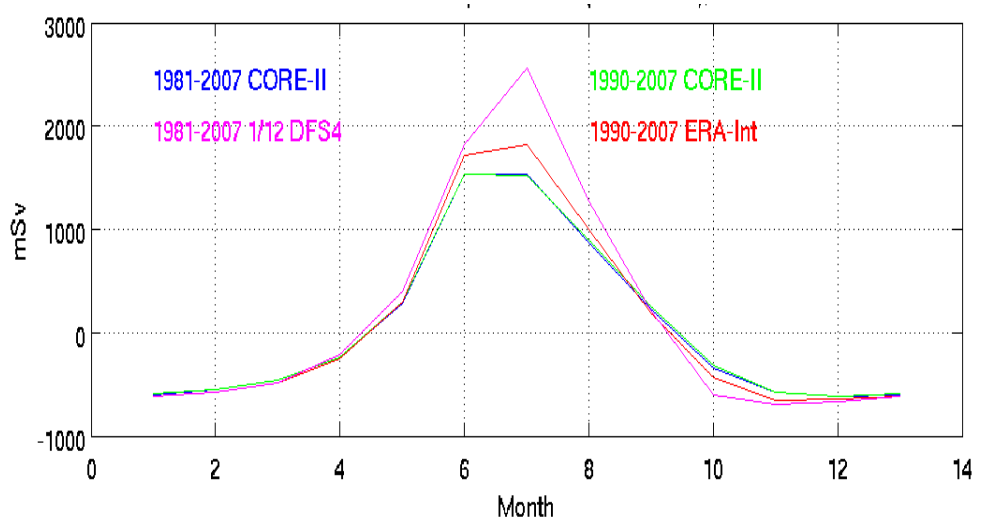

Figure 5.28 – Seasonal Arctic Ocean liquid freshwater surface flux graph (+ve is downward, inflow), reference salinity 34.8. The large peak relative to the boundary fluxes (2000 ± 500 mSv) is due to river run off from the melting of continental ice.

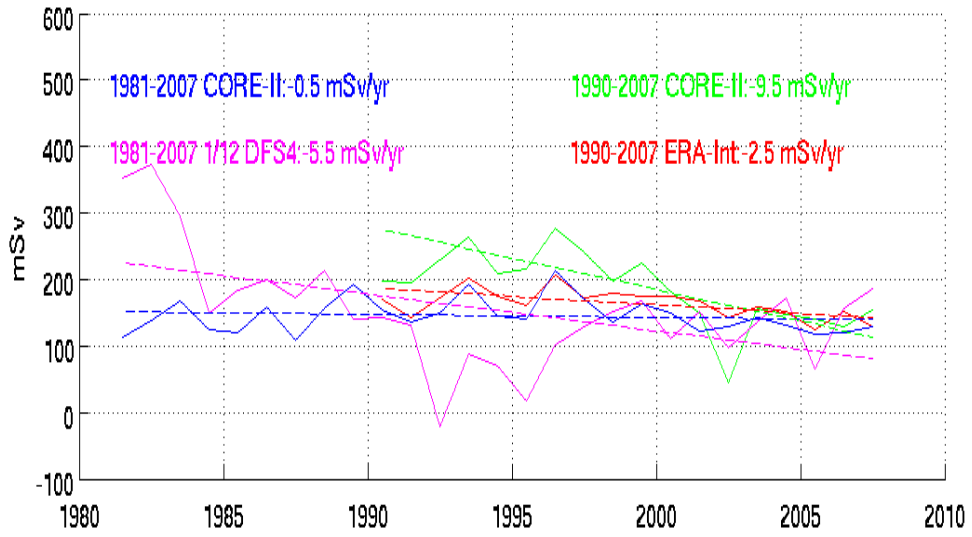

Figure 5.29 – Annual Arctic Ocean liquid freshwater boundary flux graph (+ve is outflow), reference salinity 34.8. The trend is that the amount of export is gradually reducing.

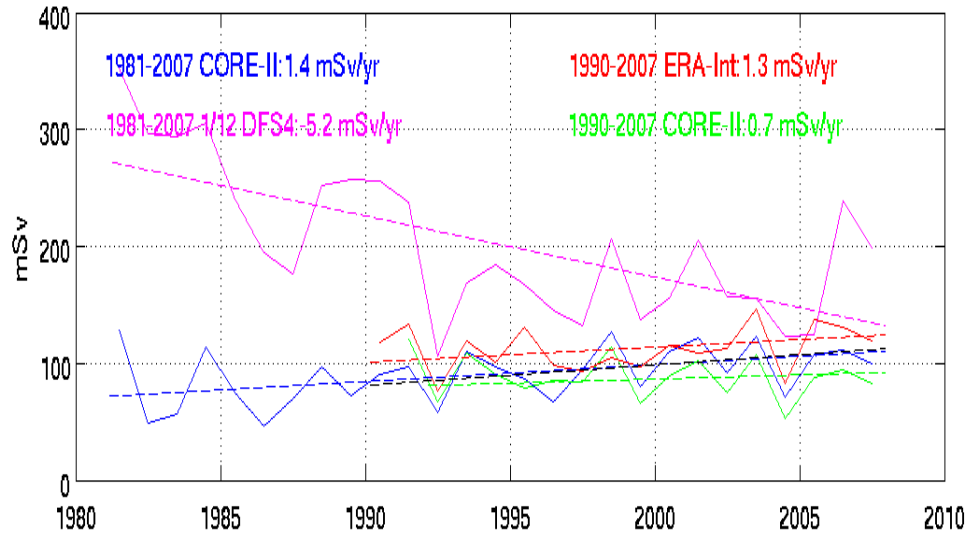

Figure 5.30 – Annual Arctic Ocean freshwater surface flux graph (+ve is downward, inflow), reference salinity 34.8. The trend is that in three of the model runs, freshwater flux is increasing, while the DFS4 run is affected by the choice of climatology.

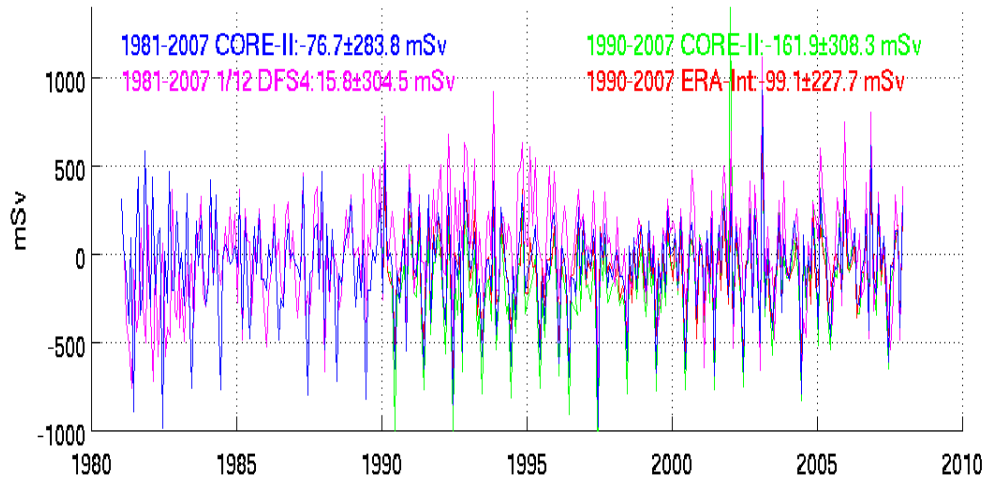

Figure 5.31 – Monthly Arctic Ocean freshwater storage graph (+ve is storage), corrected for damping, reference salinity 34.8. The average loss of freshwater of all four runs is 88.4 mSv.

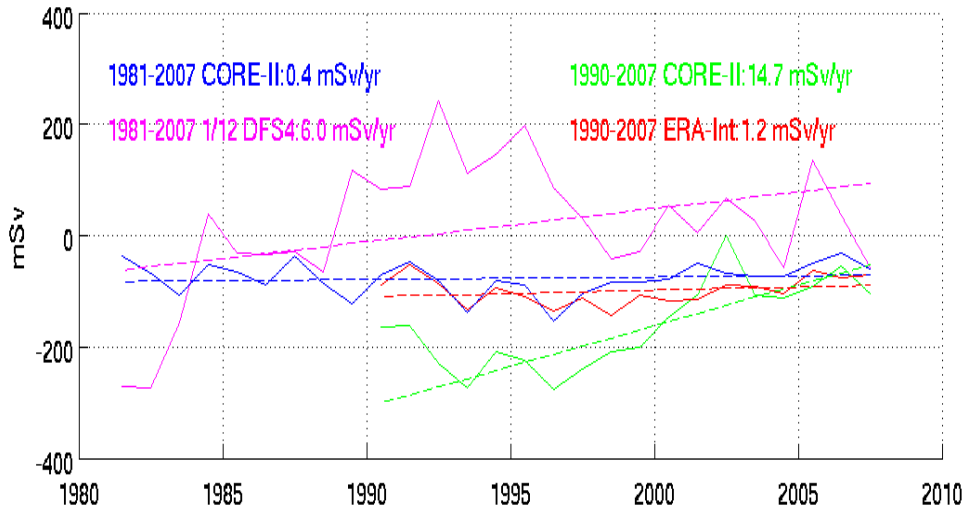

Figure 5.32 – Annual Arctic Ocean freshwater storage graph (+ve is storage), corrected for damping, reference salinity 34.8. The trend is that the amount of freshwater being lost is gradually reducing.

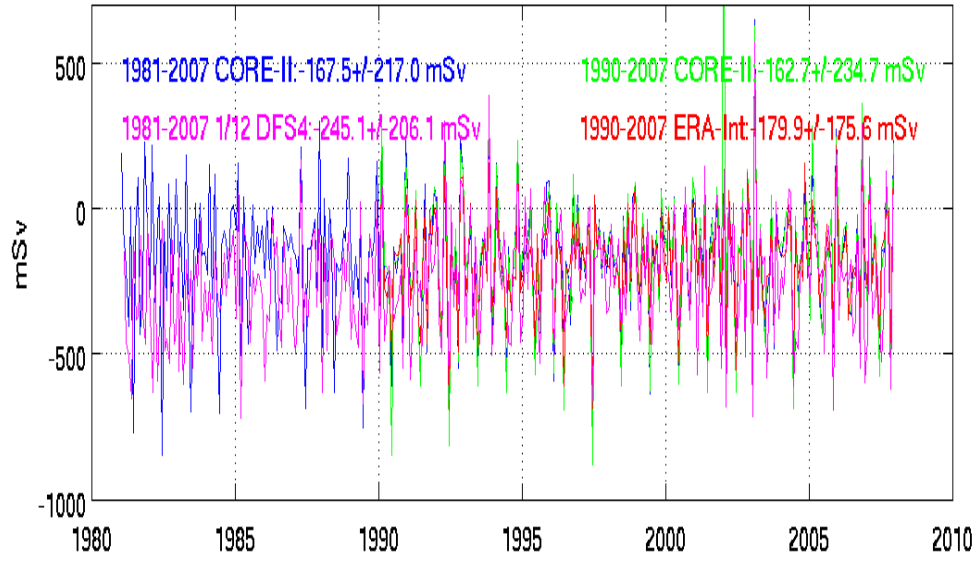

Figure 5.33 – Monthly Arctic Ocean liquid boundary flux graph (–ve is out, outflow). Boundary flux is much greater in the DFS4 forced run.

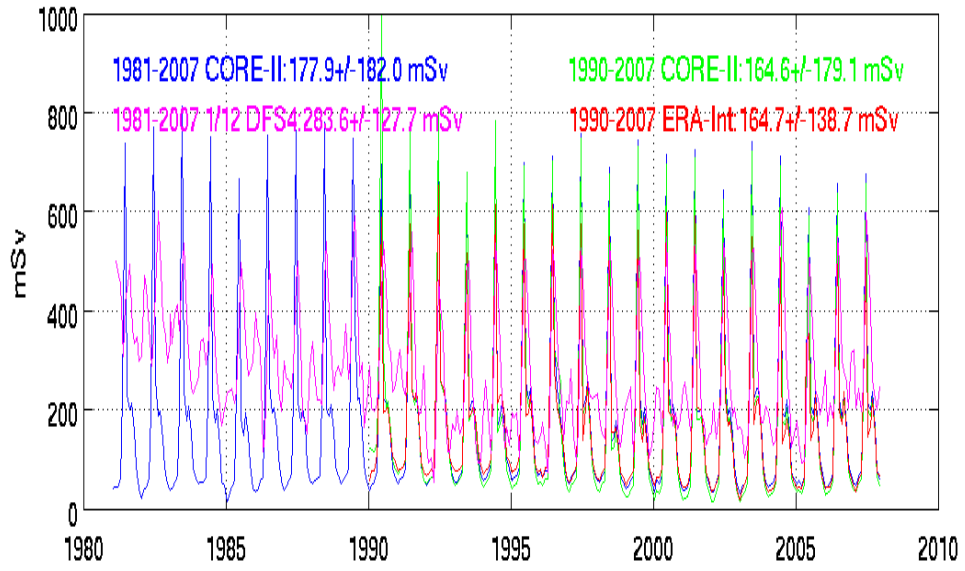

Figure 5.34 – Monthly Arctic Ocean liquid surface flux graph (+ve is down, inflow). The DFS4 run is significantly different in its shape due to the damping acting on all the months of the year.

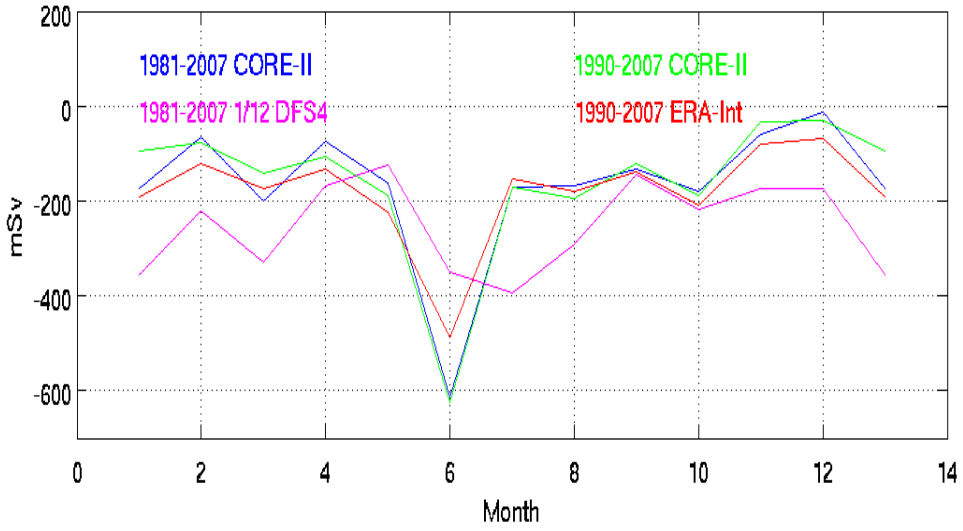

Figure 5.35 – Seasonal Arctic Ocean liquid boundary flux graph (-ve is outflow). This shows that the greatest mass loss occurs directly as a consequence of the input from melting ice.

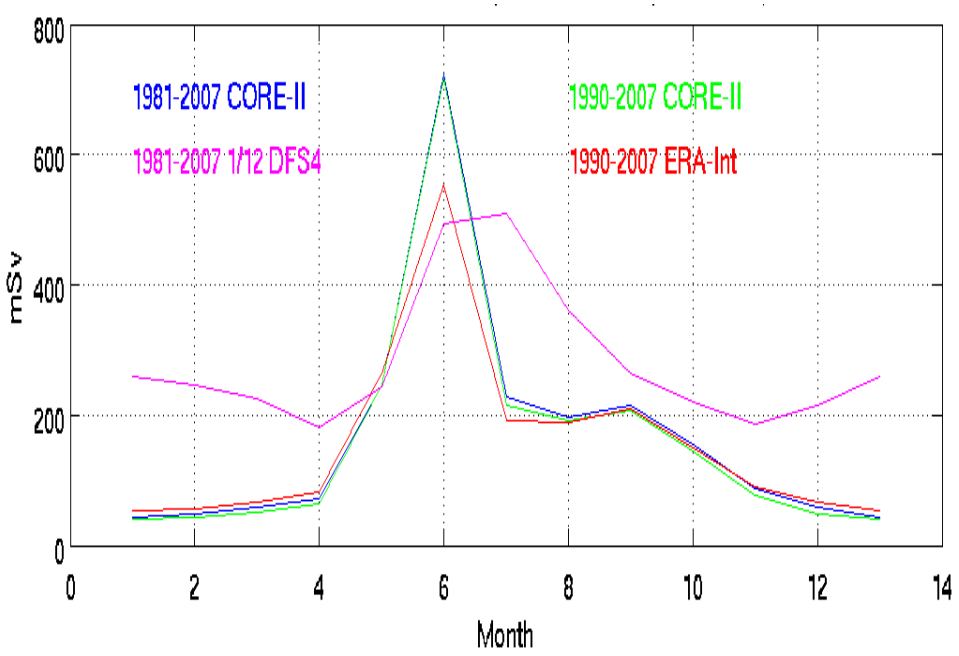

Figure 5.36 – Seasonal Arctic Ocean liquid surface flux graph (+ve is down), forming a directly opposite pattern to the boundary fluxes.

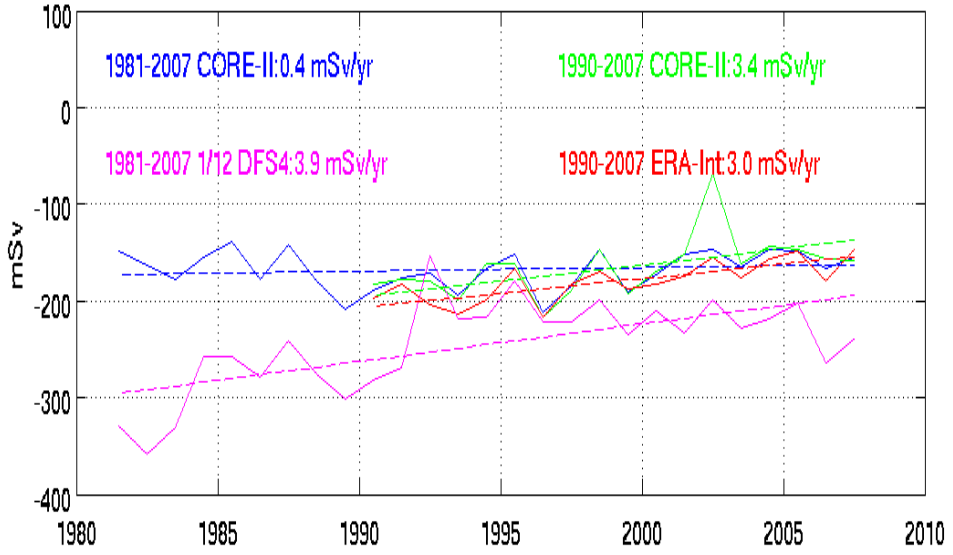

Figure 5.37 – Annual Arctic Ocean liquid boundary flux graph (-ve is outflow). The trend is that the amount of outflow is gradually reducing.

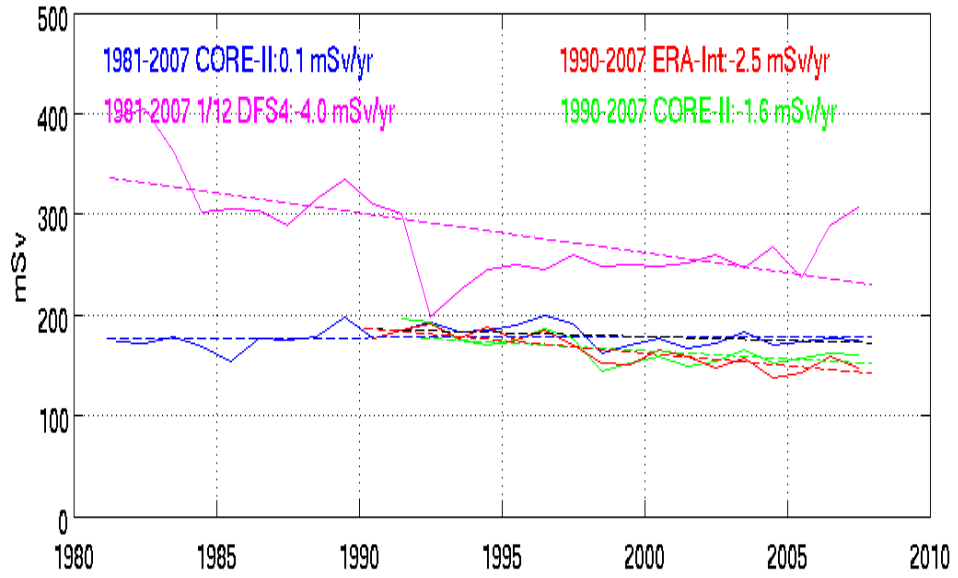

Figure 5.38 – Annual Arctic Ocean liquid volume surface flux graph (+ve is down, inflow). The trend is that there is a small reduction in input over time.

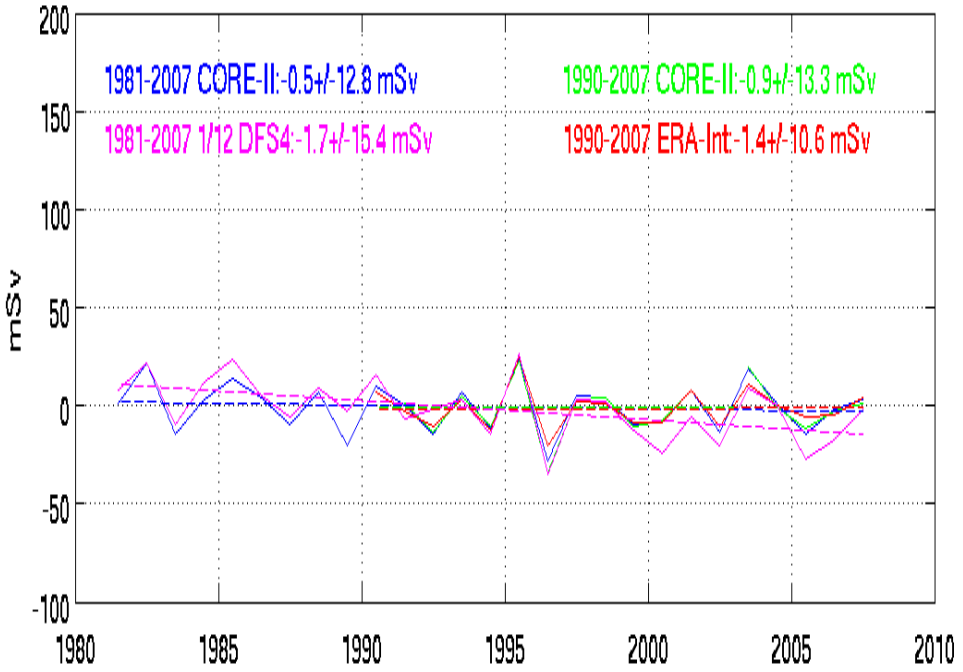

Figure 5.39 – Annual Arctic Ocean volume imbalance graph (+ve is excess). The average imbalance of 1.0 mSv for the entire region is negligible.

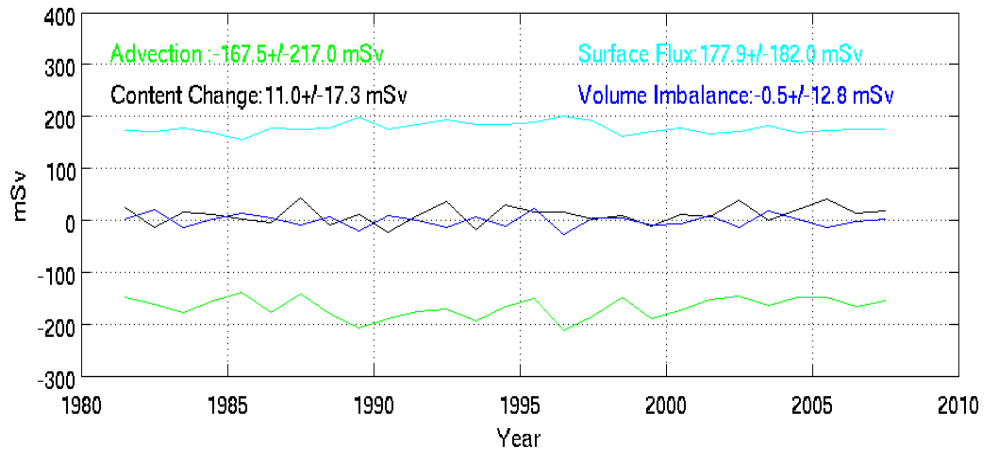

Figure 5.40 – Annual Arctic Ocean liquid volume balance components and sum imbalance for ORCA025-N206. The advection and surface flux terms are the largest contributors to the balance, while the result is a small increase of 11 mSv to the volume.

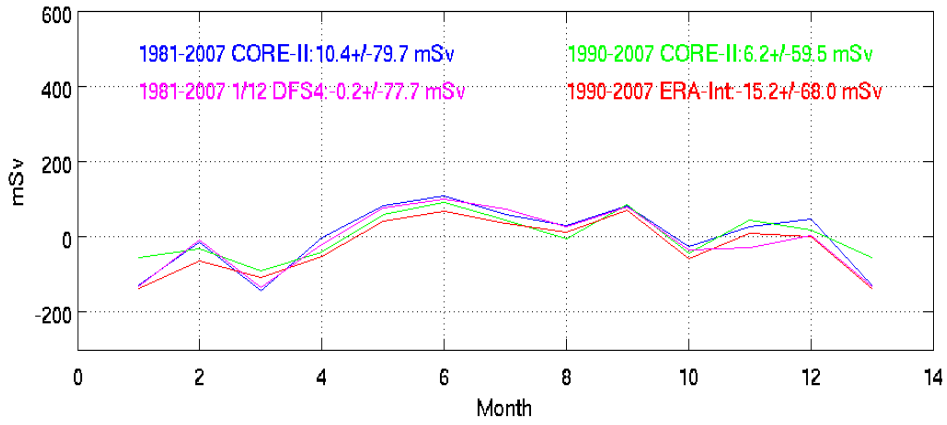

Figure 5.41 – Seasonal mass storage plot; the sum of volume surface flux and boundary flux, showing that between May and July, and then in September there is an increase in volume, while the volume decreases in January and March.

Chapter 6: Barents and Kara Seas Fluxes

This section follows on from the study of the Arctic fluxes by investigating how the thermodynamical properties are distributed within the Arctic Ocean. The Barents and Kara Seas are examined as a sub-regional case study as this is the entrance point of the Atlantic Water, which is the principal source of heat flux into the Arctic. This work is used to show how much of the total heat loss in the Arctic Ocean occurs in the region and if there is a link between model heat flow and trends in shelf sea ice formation and the Arctic Oscillation.

6.1 Region

The main source of heat being transported into the Arctic is from the Atlantic layer, and heat is lost as the water progresses through the Arctic circulation, so this section primarily focuses on the Arctic inflow sub-region. This region is the Barents Sea, with water entering through the Barents Sea Opening (BSO) and from the West Spitsbergen Current which is initially through Fram Strait but then drifts eastwards around Svalbard. The water in the Barents Sea eventually flows further east past Novaya Zemlya into the Kara Sea, before it goes through the St. Anna Trough and into the High Arctic. The definitions of the Barents and Kara Seas in the context of the wider Arctic Ocean are illustrated in Figure 6.1, while Figure 6.2 is a closer view of this sub-region with the topographical features marked.

The Kara Sea is expected to have a lesser impact on heat loss because it is further along the circulation path, but it is worth consideration in the same sub-region as the Barents Sea as it receives 1/3 of the total freshwater in the

Arctic Ocean and has a high vertical heat flux (Hanzlick and Aagaard, 1980), before the water leaves through St. Anna Trough and has undergone a substantial transformation.

This combined region is principally defined along convenient model grid boundary lines that enclose the seas within the previously defined Arctic Ocean as these either match observed sections or are suitable approximations where the definition is not fixed. This means that the same BSO section is used as in Chapter 5, while the other boundaries are lines between Svalbard and Franz Josef Land, Franz Josef Land to Severnaya Zemlya, and the Vilkitsky Strait and Shokalsky Strait which are within Severnaya Zemlya. The Barents Sea is separated from the Kara Sea by a line from Franz Josef Land to Novaya Zemlya and the Kara Gates that separate Novaya Zemlya from the model mainland Siberia (Figure 6.2).

6.2 Method

The same method of calculating boundary and surface fluxes of heat is used as in Chapter 5, but over the new sub-region area and boundary sections. The maps of the surface heat flux are also plotted to present the distribution of the heat in the different Arctic seas at different months of the year. A Hovmöller diagram of heat content of the Barents Sea is drawn using ORCA025-N206 data for the most recent ten years of the model, 1997 to 2007, to show how the heat changes within this region. This takes the sub-region area one model j-coordinate row at a time for all the layers of depth, k and all the i-coordinates in the defined row to calculate the average heat content per unit volume J. To obtain the average correctly, each row consists of the sum of the heat content and the sum of the volume of its constituent cells. T is the temperature of the cell and $e_{1,}e_2$ and e_3 are the scaling factors of each cell.

$$J = \frac{\sum_{i,k} (T \times e_1 \times e_2 \times e_3)}{\sum_{i,k} (e_1 \times e_2 \times e_3)} \quad (6.1)$$

The plot takes constant j- values for each line so the distribution is effectively how the heat content varies from south to north. The ideal shape would be for the lines to be in the same orientation as the Barents Sea Opening as this would show the heat advance in a parallel direction to the inflow but the BSO is at about a 50° angle to the (i,j) coordinates in the model. The constant j- values are chosen for convenience and to ensure that the lines are defined correctly as it is difficult to create a program that calculates volumes and correctly creates the diagonal section like the advection program does. The advection program that calculates boundary fluxes is able to calculate the optimum sequence of (i,j) coordinates that forms the straightest possible zigzag between the defined start and end of the section.

The freshwater budget is reasonably well understood on the regional scale as the Barents and Kara seas are the outflow points of most of the major Siberian rivers responsible for the heavy summer inflow found in Chapter 5 (Peterson et al., 2002, MacDonald et al., 2007, Cooper et al., 2008) and is not investigated further here.

6.3 Results

Figures 6.3-6.14 show the Arctic Ocean average monthly heat surface flux from January to December, taking the means of the monthly averages of the ORCA025-N206 data between 1997 and 2007. Blue represents an upward flux, or heat being transferred from the ocean to the atmosphere, while red represents a downward flux. The scale is chosen to reasonably show the whole range of fluxes rather than the fine structural detail within the sub-regions as the winter (December-February, Figures 6.3, 6.4, 6.14) heat loss is as much as

300 W m^{-2} in the while the summer heat input (June-August) is of the order of 100 W m^{-2} in July (Figure 6.9). Heat is mainly lost in the winter and gained in the summer, and this is mainly in the Barents and Kara Seas, as the colour scale shows surface fluxes are approximately zero for much of the rest of the Arctic throughout the year. In spring (March-May, Figures 6.5, 6.6, 6.7) and autumn (September-November, Figures 6.8, 6.9, 6.10) there is a transition between the maximum outward surface heat flux in winter and the maximum inward surface heat flux in summer. In spring, net heat gain happens gradually northwards towards the North Pole, while in autumn the transition to heat loss is patchier with the September heat gain occurring in blotches of the shelf seas. These figures show the significance of the Barents and Kara Seas in surface heat flux compared to the rest of the Arctic Ocean.

Outside of this sub-region the contributions to the Arctic Ocean are shown to come from some summer heat gain in the Bering Strait and in August some heat loss over the west coast of Svalbard (Figure 6.10). The strongest autumn heat loss also occurs to the west of Svalbard, with the effect only becoming particularly strong in the Barents Sea by the start of winter in December. Some of the strongest heat loss is shown to occur to the south of Fram Strait but this is outside the region of interest in this project.

Figures 6.15-6.25 are graphs of the different components of the heat budget in the Barents and Kara Seas. Figure 6.15 shows the monthly oceanic heat boundary flux and Figure 6.16 shows the monthly heat surface flux. Figure 6.18, the seasonal heat surface flux summarises the pattern of heat flux shown in Figures 6.3-6.14 in the Barents and Kara Seas. Like the whole Arctic, there is a greater range in the surface flux, as Figure 6.17, the seasonal average heat boundary flux goes from 50 $\pm$ 20 to 100 $\pm$ 20 TW while Figure 6.18 shows the surface flux goes from -400 TW to 200 TW while the boundary flux goes from

−220 ± 20 TW to 200 ± 20 TW in the different model runs. The mean values of the fluxes are similar to each other though, with the mean surface flux of the ensemble of runs being 79 TW. The seasonal heat fluxes show that while the surface heat gain is in the summer and the loss is in the winter, a greater boundary flux gain happens in the winter and is at its lowest in spring and early summer. The boundary flux is always positive over the course of the year, so more heat is being imported than exported through advection. Figures 6.19 and 6.20 show the annual average fluxes and show that all four models runs have the same trends but with different offsets apart from the first year of the short CORE-II run, which has been previously explained in Chapter 5 as a result of initial parameters and spin-up. Aside from its first year, 1990, the short CORE-II forced run consistently differs from the DFS4 forced run by 40 TW, which is large given that the average of all four runs is 79 TW. This could be associated with the different temperature of the atmospheric forcing, described in section 3.1. There is generally a small negative trend in the surface flux which means that more heat is being radiated to the atmosphere and a small positive trend in the boundary flux means that more heat has been imported in recent years, which is discussed in section 6.4. Figure 6.21 shows the heat imbalance from the surface flux, boundary flux and heat content change and shows that more heat is being exported than imported by an average of 1.7 TW across the different model runs.

Figure 6.22 shows the monthly ice and snow latent heat boundary flux, Figure 6.23 shows the annual latent heat boundary flux and Figure 6.24 shows the seasonal latent heat boundary flux. These figures show that 5 TW month^{-1} of latent heat is being transported out of the sub-region between April and August while it is imported between October and April, reaching an import of

40 TW in January. Compared with Figure 5.16, the latent heat boundary flux in the whole Arctic, the curve of the change in boundary flux is flatter, showing a steadier rate of sea ice being exported to the rest of the Arctic Ocean than the sea ice being exported from the whole Arctic Ocean to its surrounding seas and oceans. This is to do with the region being a source of sea ice formation, which mitigates latent heat flux of the sea ice that is being exported. Figure 6.25 shows the seasonal sensible heat boundary flux. There is a small dip below zero either side of the zero value during the summer that does not appear in Figure 5.15 of the whole Arctic sensible heat boundary flux, which suggests that in this time there is a net import of sea ice at this time. The maximum heat export value of 2.5 ± 0.5 TW is a significant proportion of the total sensible heat exported from the Arctic Ocean (Figure 5.20) which shows that the Barents and Kara seas are a major source of the ice that is exported.

Figure 6.25 is a Hövmoller plot of the Barents Sea heat content from 1997-2007, extending from the White Sea in the south to the Franz Josef Land-Novaya Zemlya boundary in the north-east, as the model grid lines are curved with respect to the lines of latitude towards the Arctic. Figure 6.26 is a Hövmoller plot of the Barents Sea heat content starting from the edge of the White Sea entrance into the Barents Sea, and finishing 1000 km further north to show the structure of the heat content distribution more clearly and how it varies over several years. These show that the average temperature of the Barents Sea drops from 6°C at the BSO to -1°C by the entrance to the Kara Sea between Franz Josef Land and Novaya Zemlya (Strait 6 on Figure 6.1). The monthly variability is shown, which shows how the water temperature is warmer further into the sea in the summer. There is also some annual variability with the average water above 2°C being 400 km further into the Barents Sea in 2001 and 2002 than in 2003 and 2004. The close up Figure

6.26 shows the entrance of the BSO in more detail, showing that the penetration of warm water into the Barents Sea varies each year.

6.4 Discussion

The mean surface flux (Table 6.1) in the Barents and Kara seas is -78 TW, with a mass imbalance of 1% of the fluxes. This is comparable to the 70 TW heat loss from the study by Smedsrud et. al., (2010). The mean surface heat flux for the whole Arctic in the model runs is -121 TW (Table 5.1). This value of heat loss for the region is comparable to other model runs of the Barents Sea (Smedsrud et al., 2013). This means that the Barents and Kara Seas have 65% of the total surface heat loss for a much smaller 14% fraction of the total surface area. The heat surface flux maps show this to be the case too as the heat loss is shown to be largely concentrated in the Barents Sea. This happens because it is the entry point of the warm Atlantic Water, which radiates heat due to the temperature difference between the water and the atmosphere to produce deep water that contributes to the global circulation. The formation of sea ice in the region increases the salinity of the water and forms a halocline that inhibits the further upward transfer of heat (Tverberg et al., 2014).

Although it is outside of the Barents and Kara Seas, the maps showed a greater concentration of ocean heat loss to the west of Svalbard, where there is heat loss even in summer when the air is warmest (Figures 6.10, 6.11) while the rest of the Arctic Ocean gains heat. The extra heat loss in this area is attributed to high levels of potential vorticity and eddy diffusion that keeps the surface of the supplied with warmer water (Teigen et al., 2014). This region is less significant though for the total heat loss of the Arctic Ocean than the Barents and Kara Seas, which have the majority of the heat loss.

The maps show some structure to the pattern of ocean heat loss in the Barents Sea. There are concentrations of heat loss that can be attributed to topography and how the Arctic circulates. Within the sea there is greater heat ocean loss where the deeper waters are, in the Bear Island Trough and Central Deep, where depths are around 400 m (Rudels et al., 1991, Gataullin et al., 1993). A lesser loss happens at the sills where the depth is closer to 200 m. This is attributable to the circulation which goes through the deeper waters and which carries the warm Atlantic Water in the currents.

The sensible heat flux showed a small inward boundary flux either side of the summer months (Figure 6.24) when there was no ice to transport. This means that ice would have been imported into the sea, even though the Barents and Kara seas are generally areas of ice formation. There is an inflow of sea ice into the Barents Sea from the high Arctic through the Svalbard-Franz Josef Land passage, especially when the ice is thick and there are strong northerly winds (Kwok et al., 2005), which has a net effect in the summer when the shelf seas are not forming ice.

The Hövmuller plot of the average temperature of the whole of Barents Sea (Figure 6.26) shows that the water progressively decreases in temperature as it enters from the south and leaves through the north. There is a seasonal cycle, shown by the furthest extent of warm water occurring in the summer and autumn, while it is at its lowest in spring. This matches with the pattern of the seasonal oceanic heat boundary flux graph (Figure 6.17) where the greatest inflow of water (including Atlantic Water) occurs from late summer and through autumn.

The whole picture is somewhat distorted by the inclusion of the White Sea, a body of water that is contained within the defined boundaries of the Barents

Sea from the Arctic Ocean but is a separate body of water that is strongly influenced from being enclosed by land other than its small Barents Sea entrance. The temperature of this small area of water is much higher that the Barents Sea as it has a more continental climate, but it does not interact much with the Barents Sea. The temperature of the Barents Sea water has also dropped below 4°C after travelling 800 km northwards, though it has not necessarily flowed straight in this direction as it may reside for some years and recirculate around the sea (Skagseth, 2008).

The Hövmoller plot of the first 1000 km beyond the entrance to the White Sea (Figure 6.26) shows interannual variability of the extent that the warm tongue penetrates into the Barents Sea. In 2002 and 2003 the tongue of water that is on average greater than 0°C only reaches as far as 600 km, while in the four years after that, the water is still above 1°C. The maximum heat boundary flux input increased in this time (Figure 6.15), as did the overall annual input of heat (Figure 6.16). This increase could eventually have implications for ice formation in the area as an albedo-feedback scenario may develop (McPhee et al, 1998). Increasing the heat input from any source reduces the ice formation, which then allows a greater solar flux to heat the surface water in summer as the water is less insulated by relatively reflective ice. The overall trend is an increase of 0.6 TW/year, which is 0.7% of the average boundary flux. The warm peak occurs sharply and then trails off more gradually, which suggests a link to the summer solar insolation heating the water and the heat is then slowly lost in subsequent months.

The intrusion of the Atlantic Water affects the temperature of the Barents Sea, which means it could be related to sea ice formation and the Arctic Oscillation (AO). The connection between sea ice formation and the AO has already been made by Rigor et al. (2002), which is that positive AO (cyclonic phase, Figure

2.4) increases the advection of sea ice away from the region, enhancing the production of new sea ice, even though this helps to circulate the Atlantic Water further into the Arctic Ocean (section 2.1.3). Figure 6.28 shows the Arctic Oscillation Index, which represents the amount of pressure anomaly against the mean, poleward of 20°N. Comparing Figure 6.28 against Figure 6.27, which shows the intrusion of warm water into the Barents Sea, there does not appear to be a correlation between the two, even when considering that there might be a time delay in the signal between the atmospheric forcing and ocean circulation. The prediction was that the stronger circulation should coincide with positive AO years. The annual average AO index (Table 6.4) does not match up with the pattern in the Hövmoller plot either. Figures 6.26 and 6.27 suggest that there are three years of weaker circulation from 1997, followed by two years of stronger circulation in 2000 and 2001, another two years of weaker circulation, then four years of stronger circulation. Some possible reasons for the lack of correlation between the AO and the intrusion of heat are that the two quantities are not linked, that there are other processes influencing the flow in the Barents Sea, or that the relationship between the two is not direct and instantaneous.

This chapter has taken a case study approach to a key sub-region of the Arctic Ocean and provide a comprehensive picture of the heat fluxes, which has not been possible from observations. For a sub-region that is a 14% of the total area of the Arctic Ocean, the Barents and Kara Seas contribute 65% of the total surface heat loss, making it an important area for the transformation of warm Atlantic Water that contributes to the global circulation. The possible link between heat flow in the Barents Sea and the Arctic Oscillation is unproven by this work however.

6.5 Tables and figures

Table 6.1: Mean oceanic heat budget for the Barents and Kara Seas in different model runs. Values are in TW, sign is positive into the region. Fluxes are monthly averages and content change and imbalance are annual averages.

Model Run	Liquid heat boundary flux	Liquid heat surface flux	Liquid heat content change	Liquid heat imbalance
ORCA025-N206	76.6 ± 32.4	-76.3 ± 153.9	2.0 ± 10.2	-1.7 ± 1.0
ORCA025-N206 Valor	65.9 ± 30.2	-64.1 ± 142.8	3.2 ± 12.0	-1.4 ± 1.0
ORCA025-N206 ValorERA	78.8 ± 23.4	-79.5 ± 173.9	0.7 ± 8.5	-1.4 ± 1.0
ORCA0083-N001	93.7 ± 26.3	-94.3 ± 192.9	1.7 ± 9.0	-2.3 ± 1.0

Table 6.2: Monthly mean solid heat budget components for the Barents and Kara Seas in different model runs. Values are in TW, sign is positive into the region.

Model Run	Solid latent heat boundary flux	Solid sensible heat boundary flux
ORCA025-N206	6.4 ± 19.9	0.5 ± 1.2
ORCA025-N206 Valor	6.2 ± 22.4	0.5 ± 1.2
ORCA025-N206 ValorERA	5.8 ± 14.8	0.6 ± 1.2
ORCA0083-N001	9.1 ± 17.2	0.9 ± 1.5

Table 6.3: Totals of monthly average Barents and Kara Seas heat budget components. Values are in TW, sign is positive into the region.

Model Run	Boundary fluxes	Surface flux	Total heat storage
ORCA025-N206	83.5	-76.3	7.2
ORCA025-N206 Valor	72.6	-64.1	8.5
ORCA025-N206 ValorERA	85.2	-79.5	5.7
ORCA0083-N001	103.7	-94.3	9.4

Table 6.4 – Annual average Arctic Oscillation Index from 1997–2007. Data obtained from National Oceanic and Atmospheric Administration, USA.

Year	Arctic Oscillation Index
1997	-0.04
1998	-0.27
1999	0.11
2000	-0.05
2001	-0.16
2002	0.07
2003	0.15
2004	-0.19
2005	-0.38
2006	0.14
2007	0.27

Figure 6.1 – Map of the Arctic Ocean, with enclosing straits of the Barents and Kara Seas (black lines) as follows: 1) Barents Sea Opening, 2) Spitzbergen-Franz Josef Land, 3) Franz Josef Land-Severnaya Zemlya, 4) Vilkitsky Strait, 5) Shokalsky Strait. Red lines divide the Barents and Kara Seas by the following straits: 6) Franz Josef Land-Novaya Zemlya, 7) Kara Gates. Adapted from Ahlenius, 2008.

Figure 6.2 – Enlarged map of the Arctic Ocean, centred on the Barents and Kara Seas. The purple area is the Arctic model region.

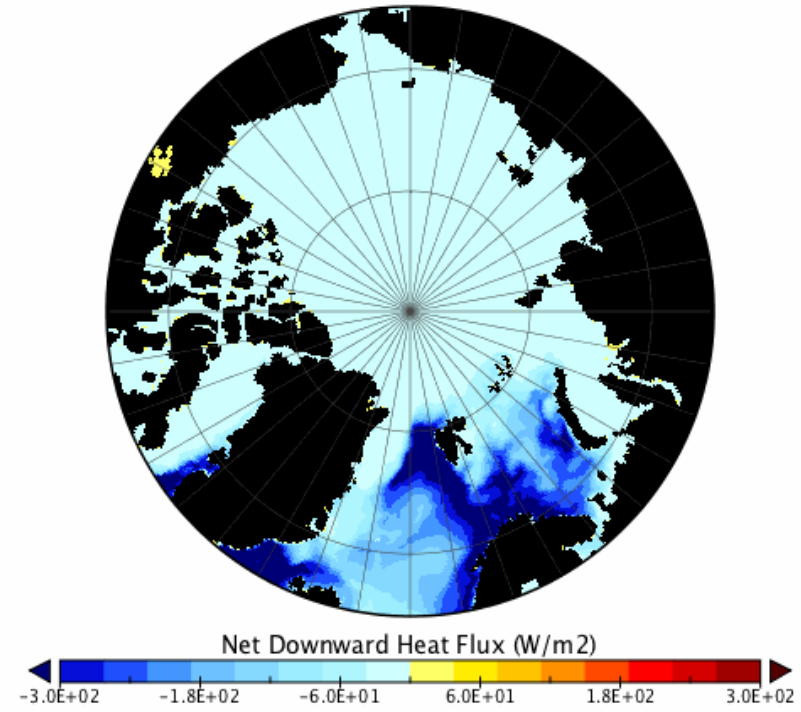

Figure 6.3 – Mean January Arctic heat surface flux between 1997 and 2007.

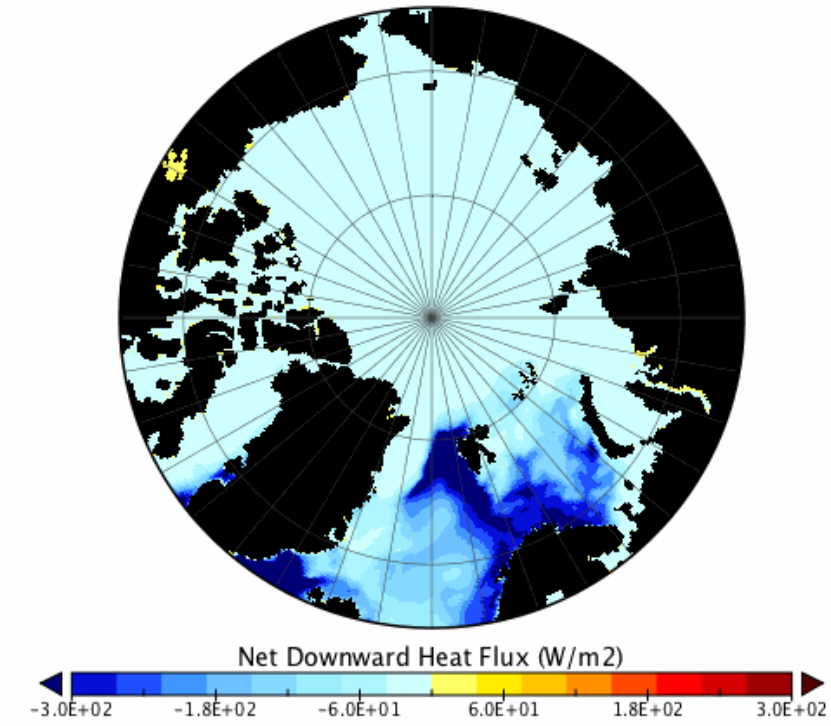

Figure 6.4 – Mean February Arctic heat surface flux between 1997 and 2007.

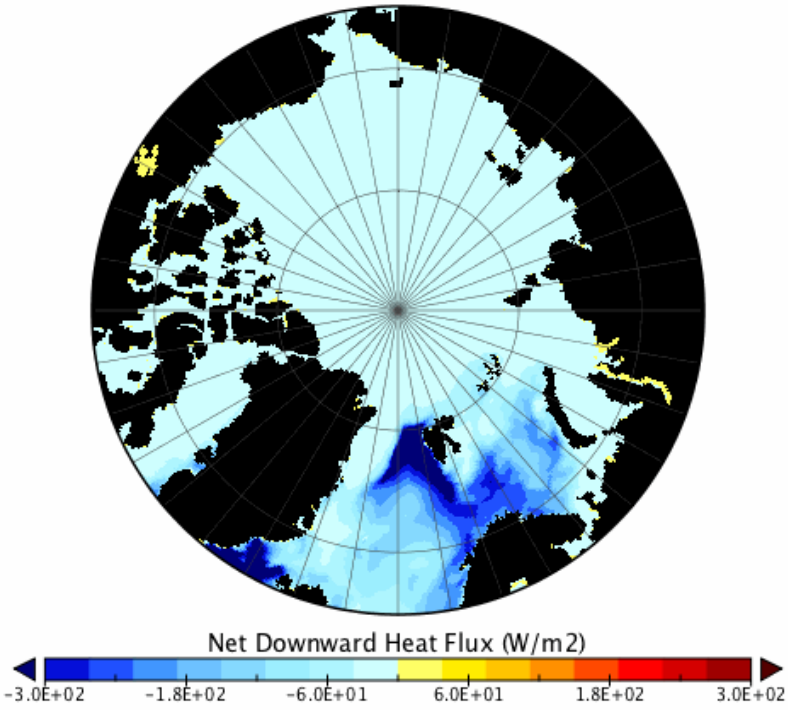

Figure 6.5 – Mean March Arctic heat surface flux between 1997 and 2007.

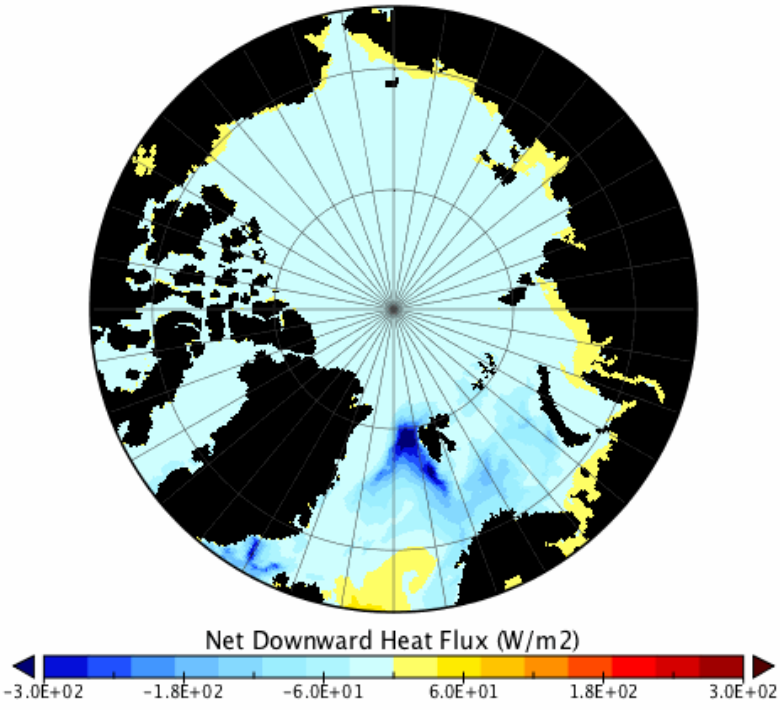

Figure 6.6 – Mean April Arctic heat surface flux between 1997 and 2007.

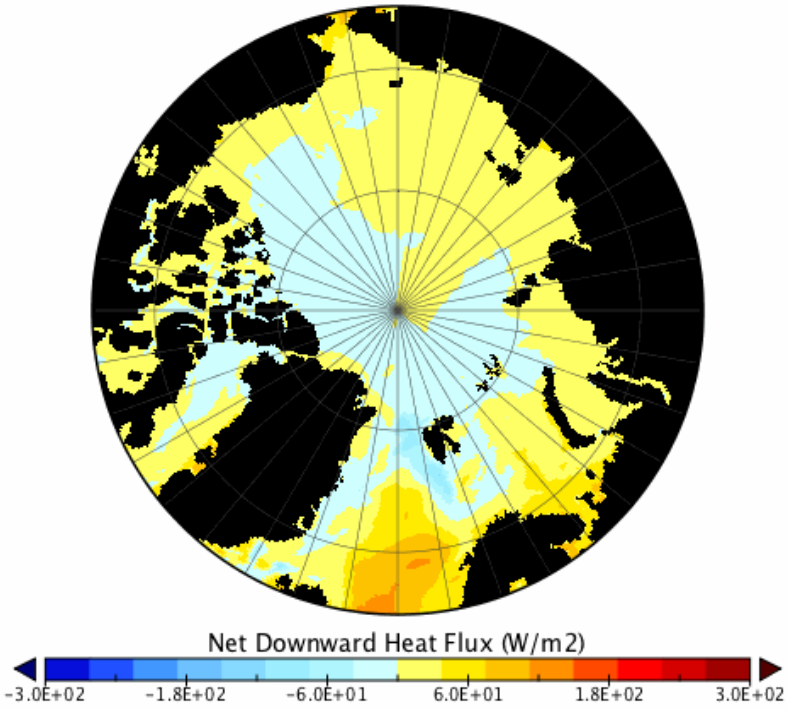

Figure 6.7– Mean May Arctic heat surface flux between 1997 and 2007.

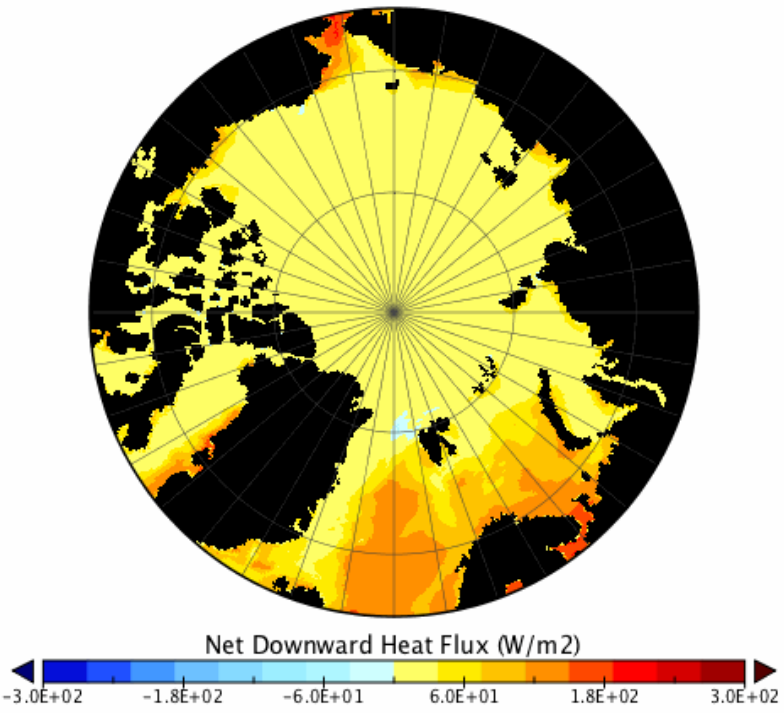

Figure 6.8 – Mean June Arctic heat surface flux between 1997 and 2007.

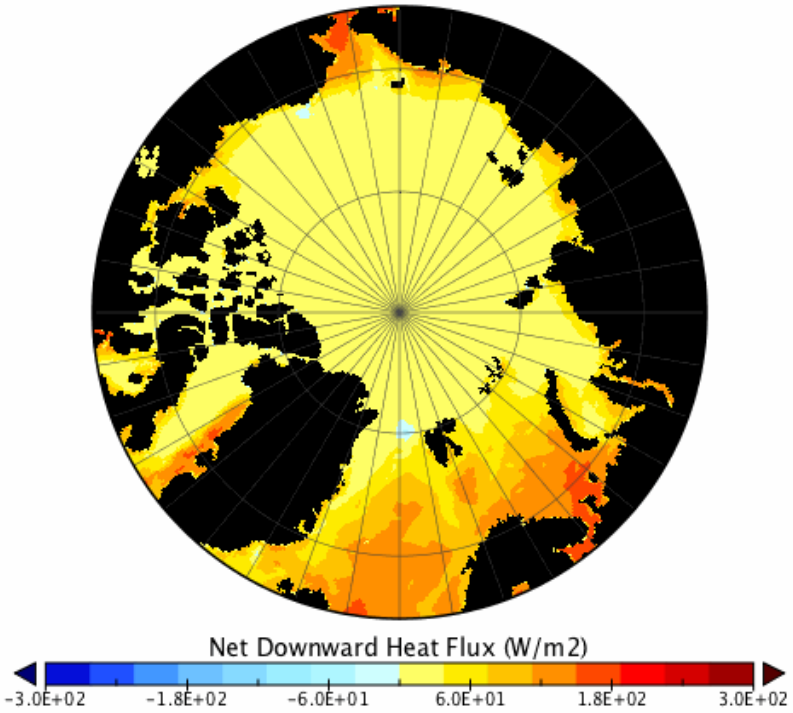

Figure 6.9 – Mean July Arctic heat surface flux between 1997 and 2007.

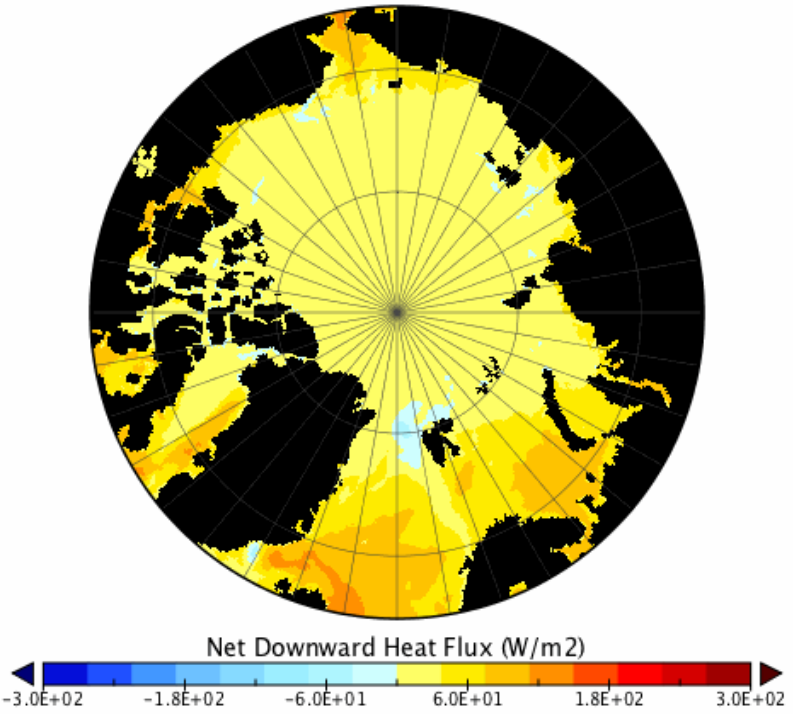

Figure 6.10 – Mean August Arctic heat surface flux between 1997 and 2007.

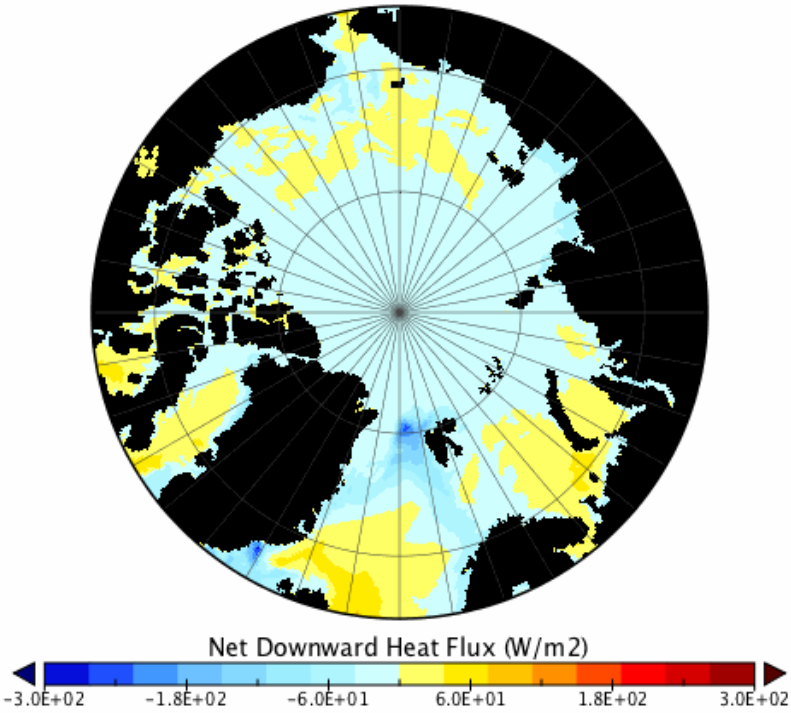

Figure 6.11 – Mean Sept. Arctic heat surface flux between 1997 and 2007.

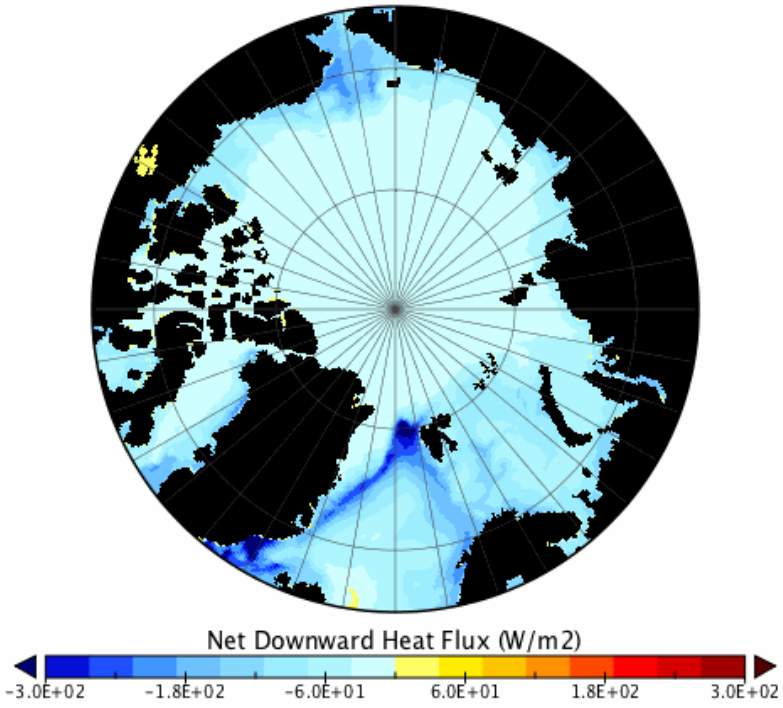

Figure 6.12 – Mean Oct. Arctic heat surface flux between 1997 and 2007.

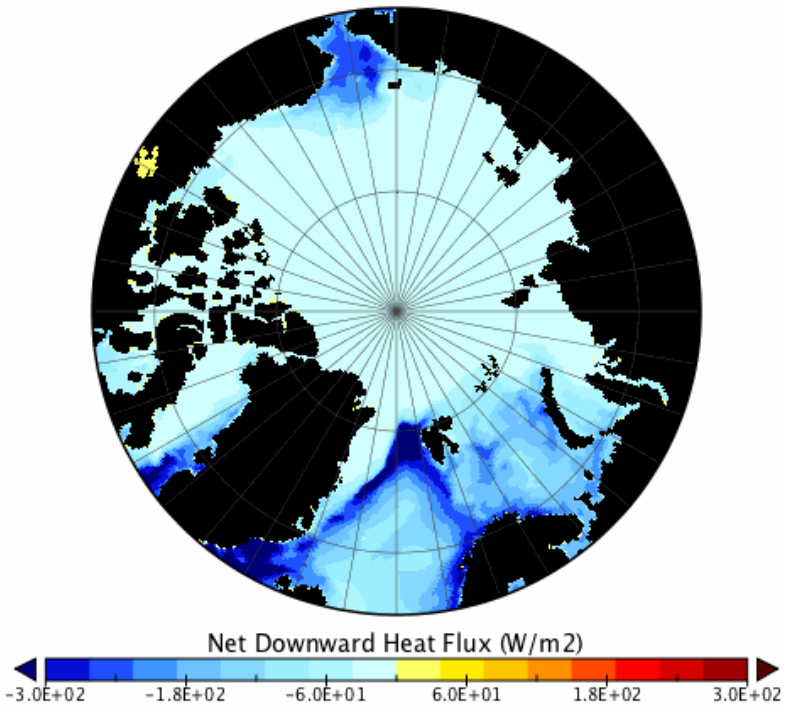

Figure 6.13 – Mean Nov. Arctic heat surface flux between 1997 and 2007.

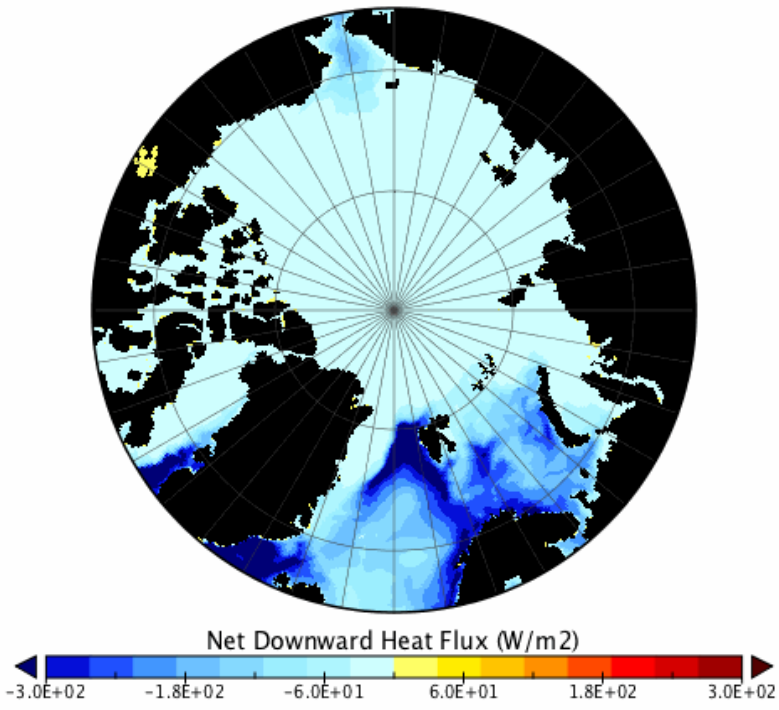

Figure 6.14 – Mean Dec. Arctic heat surface flux between 1997 and 2007.

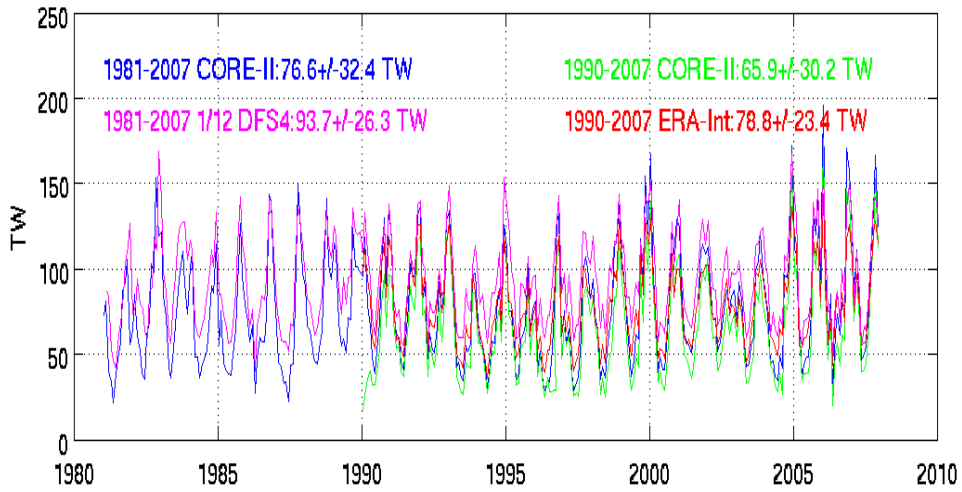

Figure 6.15 – Monthly Barents and Kara Seas oceanic heat boundary flux graph (–ve is out), reference temperature 0°C.

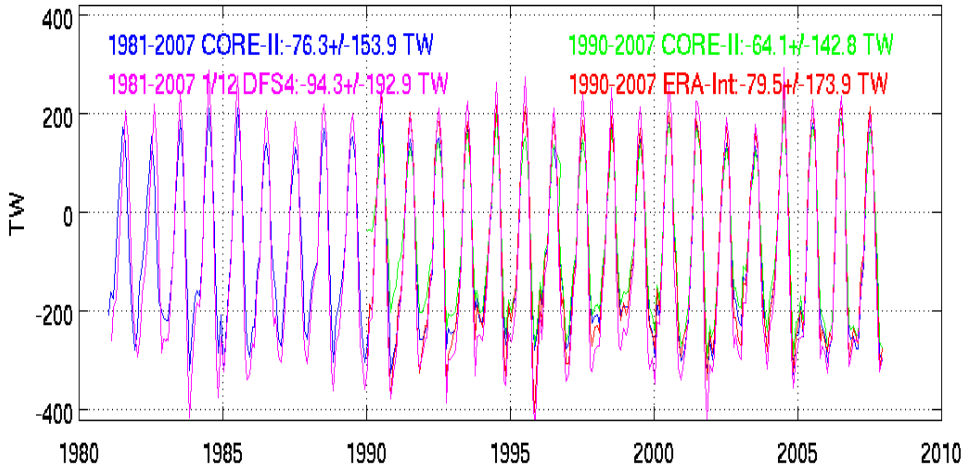

Figure 6.16– Monthly Barents and Kara Seas heat surface flux graph (+ve is down), reference temperature 0°C.

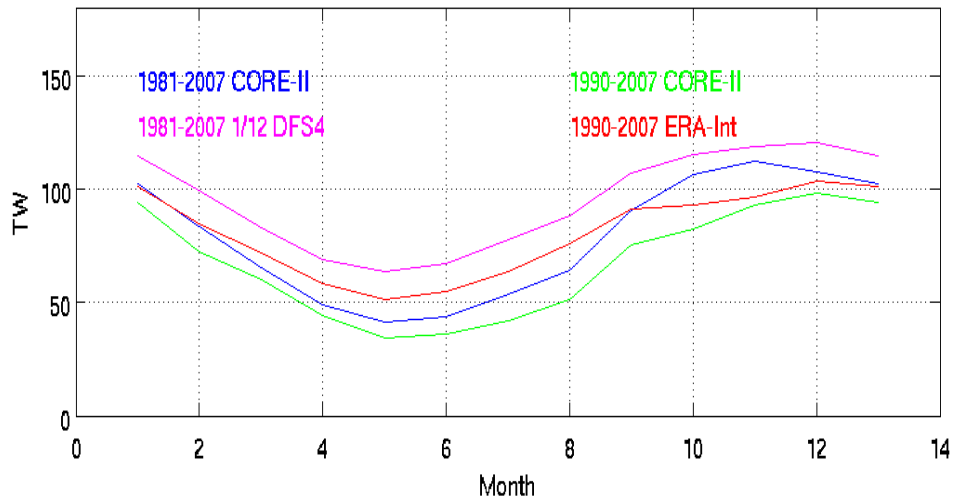

Figure 6.17 – Seasonal Barents and Kara Seas oceanic heat boundary flux graph (–ve is out), ref. temp. 0°C.

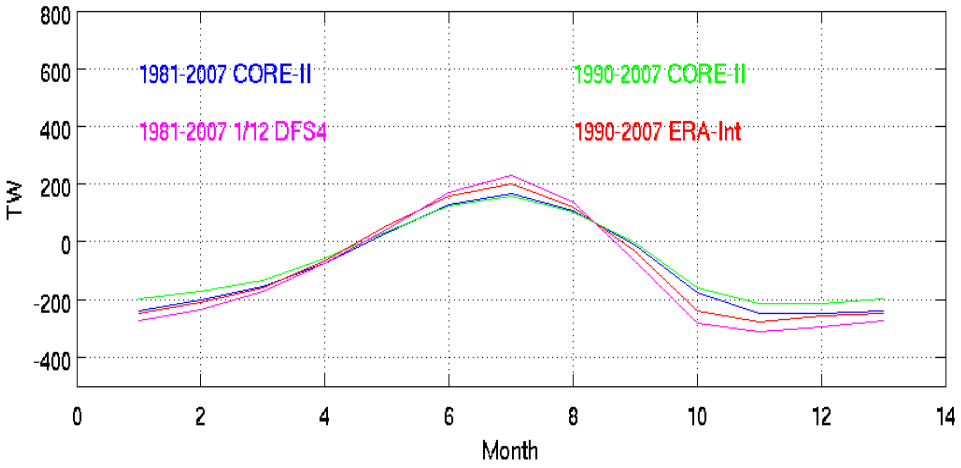

Figure 6.18 – Seasonal Barents and Kara Seas heat surface flux graph (+ve is down), ref. temp. 0°C.

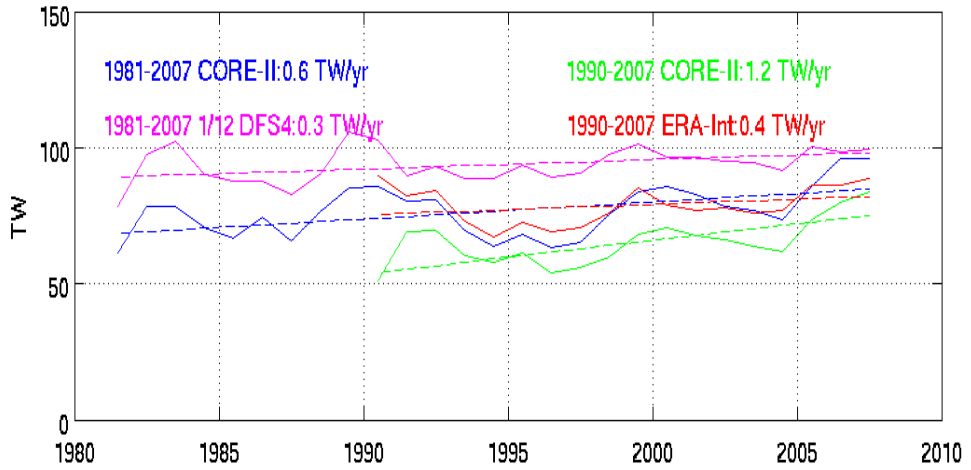

Figure 6.19 – Annual Barents and Kara Seas oceanic heat boundary flux graph (–ve is out), reference temperature 0°C.

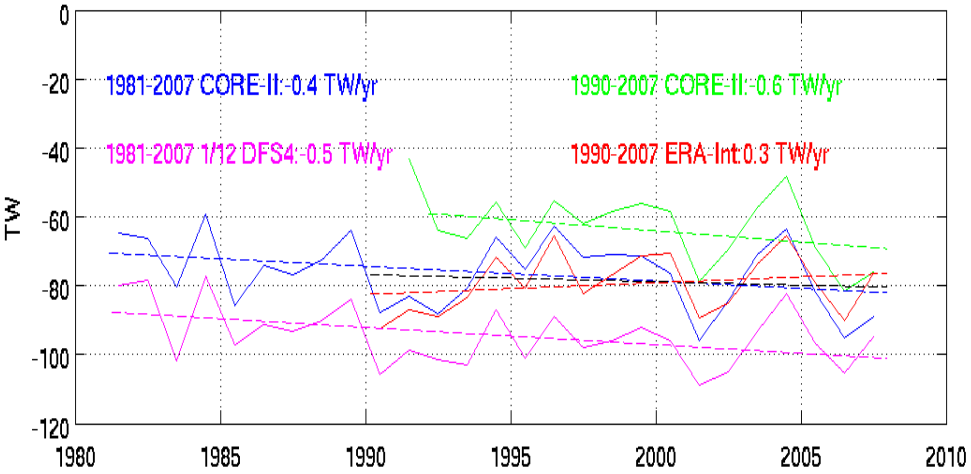

Figure 6.20 – Annual Barents and Kara Seas oceanic heat surface flux graph (+ve is down), reference temperature 0°C.

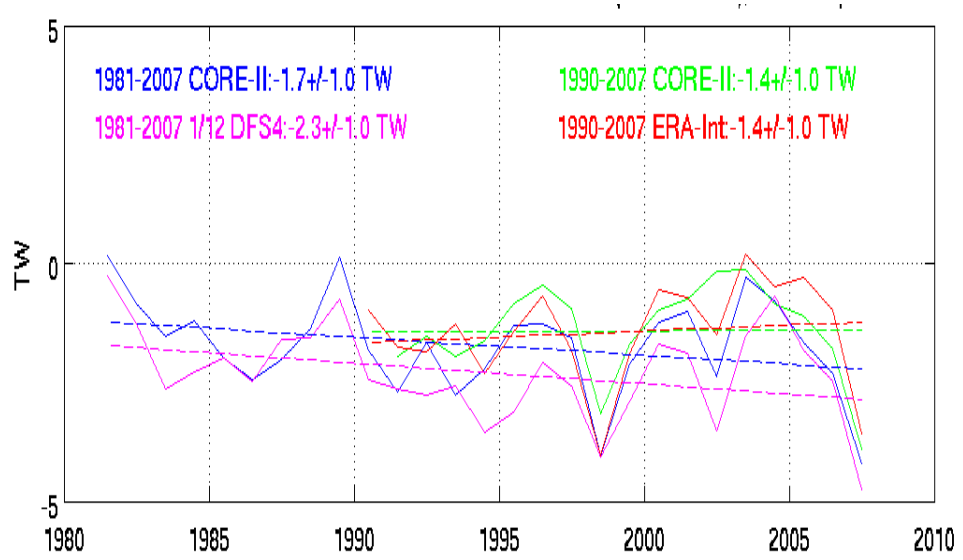

Figure 6.21 – Annual Barents and Kara Seas heat imbalance, reference temperature 0°C.

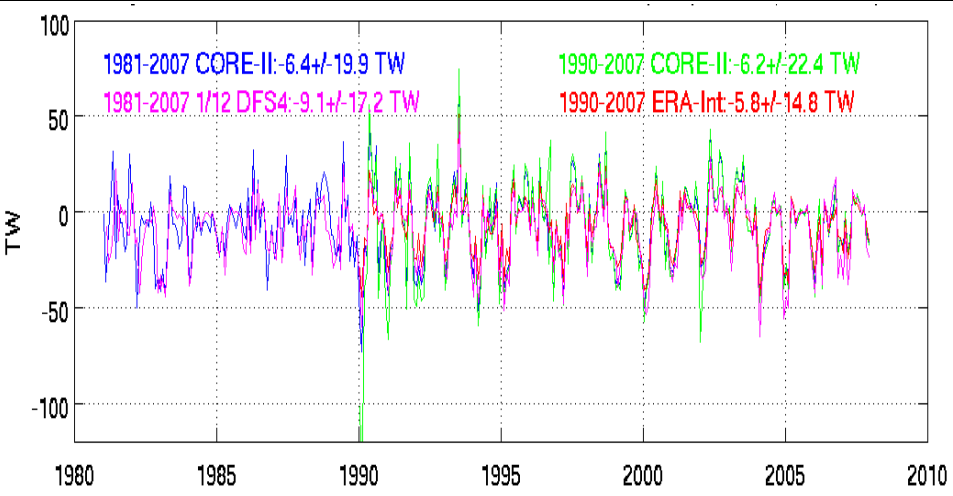

Figure 6.22 – Monthly Barents and Kara Seas ice and snow latent heat boundary flux graph (+ve is out), reference temperature 0°C.

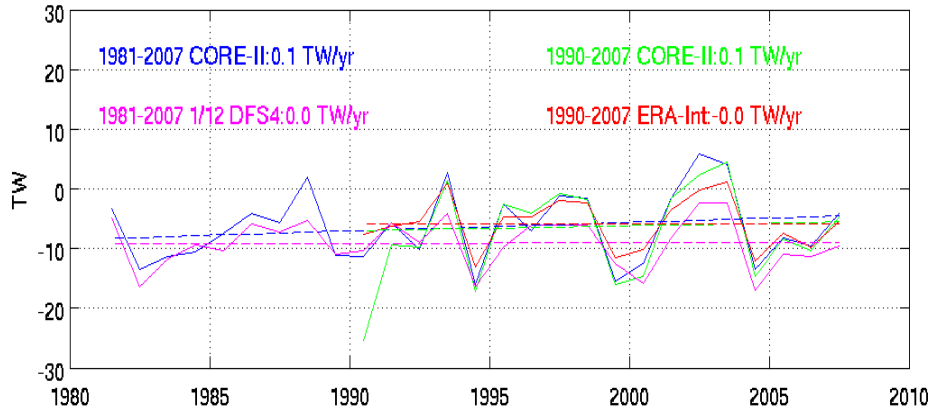

Figure 6.23 – Annual Barents and Kara Seas ice and snow latent heat boundary flux graph (–ve is out), reference temperature 0°C.

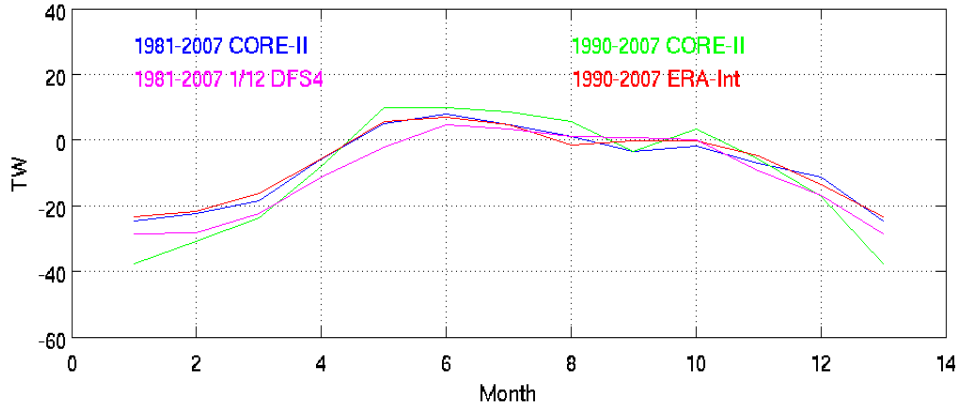

Figure 6.24 – Seasonal Barents and Kara Seas ice and snow latent heat boundary flux graph, ref. temp. 0°C.

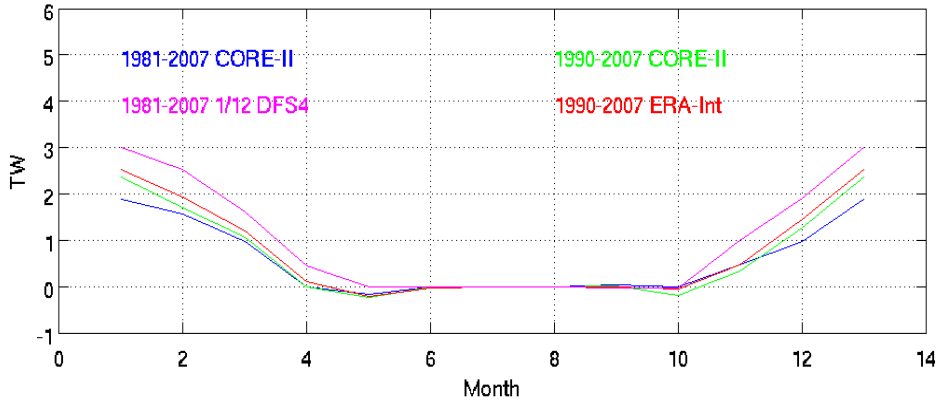

Figure 6.25 – Seasonal Barents and Kara Seas ice sensible heat boundary flux graph (+ve is out), ref. temp. 0°C.

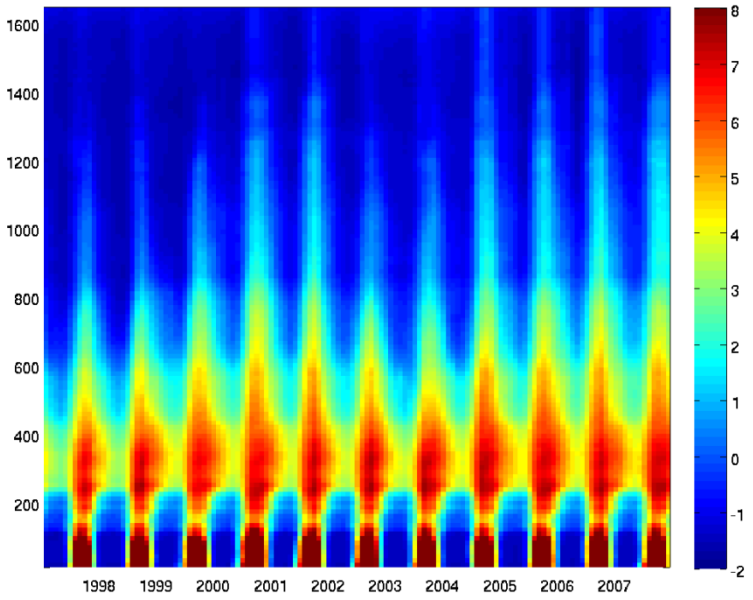

Figure 6.26 – Hövmoller plot of Barents Sea temperature.

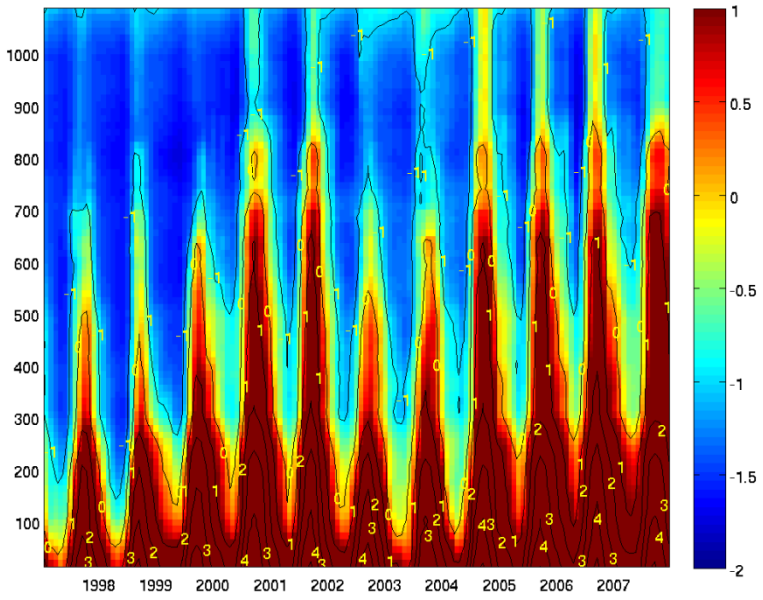

Figure 6.27 – Hövmoller plot of of Barents Sea temperature between the Barents Sea Opening and 1100 km into the sea.

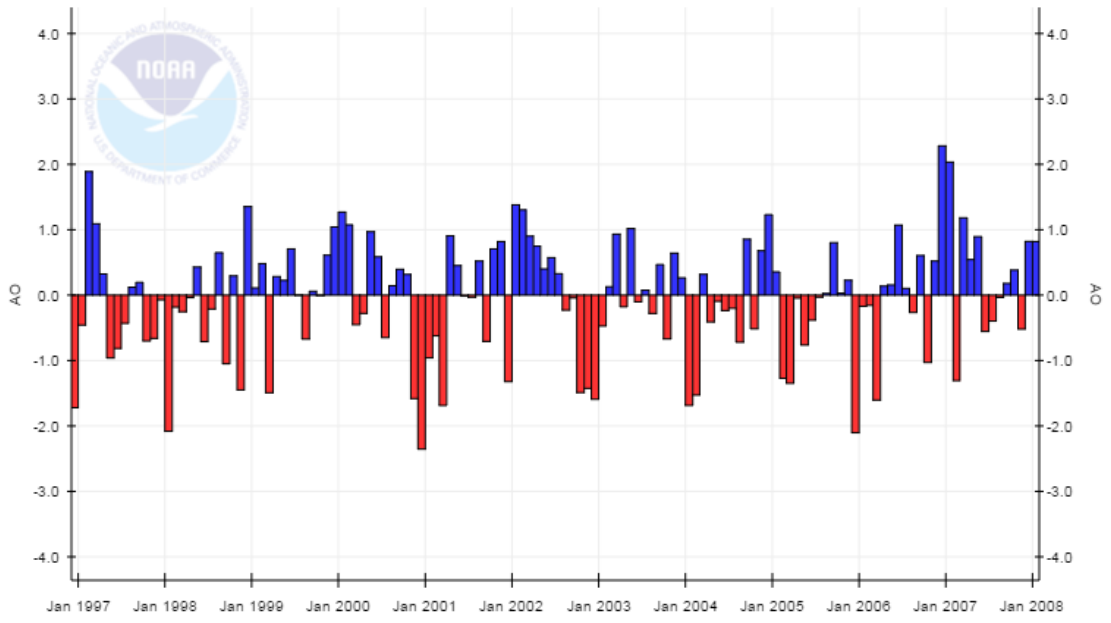

Figure 6.28 – Arctic Oscillation index between 1997 and 2007, blue bars are positive index (cyclonic regime) where low pressure is above the North Pole, red bars are negative index (anti-cyclonic regime) where high pressure is above the North Pole. Data from from National Oceanic and Atmospheric Administration, USA.

Chapter 7: Discussion and Further Work

This section brings together the main conclusions from the previous chapters and discusses how the work could be extended in the future to answer unresolved questions. The ability of the project to have studied the whole Arctic Ocean and the sub-region of the Barents and Kara Seas will contribute to our understanding of the physics of the region, especially since as a whole region it is not well observed and understood despite its importance.

7.1 Mass conservation

The study has shown that NEMO conserves volume within a well-defined self-containing region over the duration of a model run. The study's definition of the 'true' Arctic Ocean had a mass imbalance of 0.3% of the fluxes. This still applies when taking annual and monthly averaged data from output at the model time step of five days. The level of volume non-conservation is within the tolerable limit of the computer precision for results to be considered reliable. Within a shorter period of time of the model run, fluctuations in the conservation are possible. This is possibly due to the size of the region as perfect conservation can only be expected at the scale of an individual cell, and there may be a response time required for an alteration in one of the fluxes to propagate and even out in the system.

Due to the Boussinesq approximation used by the model, the volume conservation translates into mass being conserved. This validates the use of the model for calculating heat and freshwater fluxes, since the change in temperature and salinity of the system is from a well-defined amount of water,

which makes the calculations independent of any reference temperature and salinity used.

This project has improved the utility of the diagnostic CDFTools software, as we designed new programs to be able to create regional areas of any shape in the model and programs that correctly calculate boundary fluxes, surface fluxes and content change of mass, freshwater, and heat.

7.2 Arctic Ocean fluxes

The damping in the 1/4° runs was different from the 1/12° damping. The 1/12° damping has an unrealistic value, as it uses an outdated climatology to attempt to achieve the correct river run off. The effect of the incorrect values manifested itself most significantly at the shelf seas where rivers flow into. This does not affect the mass conservation as the effects of the incorrect damping propagate into the fluxes, which account for the extra volume of water that is provided. A suggestion would be that the 1/12° model run should only be used from 1993 onwards to provide meaningful results for individual components of the volume balances.

The liquid heat and freshwater flux budgets reasonably conserve, with the 1/4° conservations not expected to be perfect due to the linear free surface setting. The different runs align with each other relatively closely for the different thermodynamic quantities, suggesting that there is not a major dependence on the resolution or the atmospheric forcing, as long as the PHC climatology is used in the polar regions (section 5.8.1).

There is a strong seasonal cycle of freshwater storage, where 2 Sv of water from river run-off is added to the ocean in the summer and the rest of the year is spent removing this water, mainly through the formation of sea ice in the

winter and an element of boundary flux transport. There is a delay for the water to circulate around the ocean and leave through the boundary fluxes which shows a short-term residency period before it is removed, though over the course of the year there is storage of 30 mSv of freshwater.

The heat cycle also has a seasonal pattern, though less dramatic than the freshwater seasonal cycle. This cycle is mainly due to solar insolation and the insulating effect of sea ice. In both cases, the surface fluxes are greater than the boundary fluxes, which shows that a large proportion of the thermodynamic inputs never go far below the surface layer of the water to reside for a long time and circulate around the ocean. There is 3.7 TW of heat storage.

Observations of the Arctic Ocean tend to be made in late summer, which happens to be a period where the storage of water and heat is nearly zero (Figures 5.22, 5.41). This possibly stands to reason as the most favourable conditions for conducting observations are when they are at their mildest and the lack of extreme levels of fluxes means that less compensation and a shorter timescale is required for everything to balance. This coincidental occurrence means that reconstructions and inferences for periods of times and regions where observations do not take place are unbiased by storage, which would otherwise impact on the reliability of studies. This is particularly important in the Arctic as it is an inaccessible region that has a dearth of sampling relative to most of the rest of the world and is therefore prone to bias (Cowtan and Way, 2014). Especially in the central Arctic, the atmospheric models are based on reanalysis of as much observational data as is available, which has its limitations (Trenberth et al., 2008). This project shows that in the absence of real measurements the NEMO model is able to successfully reproduce some existing results though it does still have its own limitations

such as being able to correctly model the behaviour when shallow water transforms to dense water and sinks (Aksenov et al., 2010).

7.3 Barents and Kara Seas fluxes

Of the heat that is lost in the Arctic Ocean through surface fluxes, 65% of it is lost in the Barents and Kara Seas. This is a very large proportion for a 14% fraction of the total area of the Arctic (Smedsrud et al, 2010). This proportion is dependent on how the Arctic is defined, but the definition of the region used in this project is broadly similar to most other studies of the Arctic, in both model and observational work.

The heat balance also has a seasonal cycle and some interannual variability in heat loss as the water flows through the Barents Sea to be much cooler by the time it leaves. This shows the large amount of heat that is brought to the Arctic Ocean by Atlantic Water.

It is possible for the inflowing Atlantic Water from the Norwegian Coastal Current to recirculate without ever properly residing in the Arctic Ocean, which means that not all of the surface heat transfer of the Atlantic Water is lost in the Barents and Kara Seas. If this water was to reside for longer in the Arctic Ocean, this would increase the local heat loss near the entrance gateways, which would affect the stratification of the different water masses in the Arctic due to the cooling that would take place.

7.4 Future work

A possible line of future research would be to continue the study of heat fluxes beyond the present region and sub-region examined in this project. The existing work has shown that the Barents and Kara Seas is a major source of Arctic Ocean heat transfer at the sea surface due to the amount of heat introduced by the Atlantic Water, and the cooled water sinks below the surface into a deeper intermediate layer where it continues to circulate around the Arctic. This water still has some of the heat that has been introduced from the Atlantic, albeit a much reduced amount, and a future project would be to study the processes involved in the heat transfer here as the water is no longer at the surface due to it sinking and following topography. This investigation would look at other sub-regions of the Arctic Ocean that the Atlantic Water circulation flows into, which would be determined by using a particle tracking program. The main part of the experiment would be to calculate the amount of vertical heat diffusion that happens between layers and map how the water temperature changes with depth along the path of the circulation. It would then be possible to trace the full fate of the Atlantic Water as it circulates around the Arctic Ocean.

There is however a large amount of heat shown to be lost in the Nordic Seas, outside of the defined Arctic Ocean. The Nordic Seas is a transitional region between the Arctic Ocean and the Atlantic Ocean that show traits of both. It contains inflow from the West Spitzbergen Current that is of Atlantic origin, and also contains polar outflow from the Arctic from the East Greenland Current. Since the majority of Arctic heat is lost before the water leaves the Kara Sea, the heat lost in the Nordic Seas is Atlantic Water that has recirculated, a behaviour that is due to the outflow of the East Greenland

Current pushing back against the inflow (Mauritzen et al., 2011). Atlantic Water mixes isopynically with Upper Arctic Intermediate Water to create overflow water that returns through the East Greenland Current, over the Greenland-Scotland Ridge and back into the Atlantic Ocean (Meincke et al., 1997, Strass et al., 1993). As the heat loss here appears to be substantial, it would be valuable to further investigate its proportion relative to the rest of the Arctic.

Also, further research into the performance of higher resolution models such as NEMO is of interest due to their ability to increasingly resolve small scale features such as the Rossby radius in the deep sea, though 1 km resolution is needed for the shelf seas and this is unattainable as of yet (Nurser and Bacon, 2014). There is a question of whether models being able to resolve these features will subsequently produce more realistic outputs, as horizontal diffusion and isopycnal mixing may be improved but vertical mixing might not necessarily benefit.

An alternative direction would be to increase the scope of the model overview of the Arctic Ocean that has been conducted in this project, rather than probe deeper into the thermodynamic quantities already investigated. This project has covered two of the three main systems in the Arctic Ocean, in heat and freshwater, but has not explored the carbon cycle. The study of marine ecosystems is hindered due to the lack of observations, and given the trends in heat and freshwater, a change in climate may have an impact on organisms (Wassmann et al., (2011). Models exist for combining physics and biology, including NEMO, but they disagree over whether light or the availability of nutrients is the biggest limiting factor in the Arctic for the production of organic carbon from marine phytoplankton, otherwise known as primary production (Popova et al., 2012). A decrease in ice coverage would permit

more light to reach the ocean, which would increase the primary production (Vancoppenelle et al., 2013). The carbon cycle also incorporates carbon dioxide and ocean acidification, for which the freshwater effects from ice retreat and the stability of the Arctic stratification are significant (Popova et al., 2014). For these simulations to be improved there needs to be a better understanding of sea ice coverage and how the thermodynamic properties studied in this project influence this seasonal cycle and long-term trend, which could be achieved using NEMO.

List of References

Aagaard, K., Coachman, L.K., & Carmack, E. (1981). On the halocline of the Arctic Ocean. *Deep Sea Research Part A. Oceanographic Research Papers, 28*(6), 529-545.

Aagaard, K., & Carmack, E.C. (1989). The role of sea ice and other fresh water in the Arctic circulation. *Journal of Geophysical Research: Oceans (1978-2012), 94* (C10), 14485-14498.

Adcroft, A., & Campin, J.M. (2004). Rescaled height coordinates for accurate representation of free-surface flows in ocean circulation models. *Ocean Modelling 7*(3-4), 269-284. doi:10.1016/j.ocemod.2003.09.003

Ahlenius, H. (2008). Arctic, topography and bathymetry (topographic map). UNEP/GRID-Arendal.[Online]. Available at http://www.grida.no/graphicslib/detail/arctic-topography-and-bathymetry-topographic-map_d003.

Aksenov, Y., Ivanov, V.V., Nurser, A. J. G., Bacon, S., Polyakov, I. V., Coward, A. C., Naveira-Garabato, A.C., & Beszczynska-Möller, A. (2011). The Arctic circumpolar boundary current. *Journal of Geophysical Research*: Oceans (1978-2012), *116* (C9). doi:10.1029/2010JC006637.

Allen, J. T., Smeed, D. A., Nurser, A. J. G., Zhang, J. W., & Rixen, M. (2001). Diagnosis of vertical velocities with the QG omega equation: an examination of the errors due to sampling strategy. *Deep Sea Research Part I: Oceanographic Research Papers*, *48*(2), 315-346.

Arakawa, A., & Lamb, V. R. (1977). Computational design of the basic dynamical processes of the UCLA general circulation model. *Methods in computational physics, 17,* 173-265.

List of References

Årthun, M., Eldevik, T., Smedsrud, L.H., Skagseth, Ø., & Ingvaldsen, R.B. (2012). Quantifying the Influence of Atlantic Heat on Barents Sea Ice Variability and Retreat. *Journal of Climate, 25* (13), 4736–4743. doi:10.1175/JCLI-D-11-00466.1.

Barnier, B., Madec, G., Penduff, T., Molines, J.–M., Treguier, A.–M., Le Sommer, J., Beckmann, A., Biastoch, A,. Böning, C., Dengg, J., Derval, C., Durand, E., Gulev, S., Remy, E., Talandier, C., Theetten, S., Maltrud, M., McClean, J., & De Cuevas, B. (2006). Impact of partial steps and momentum advection schemes in a global circulation model at eddy permitting resolution. *Ocean Dynamics, 56* (5–6), 543–567. doi: 10.1007/s10236-006-0082-1.

Bouillon, S., Fichefet, T., Legat, V., & Madec. G. (2013). The elastic–viscous–plastic method revisited. *Ocean Modelling, 71,* 2–12. doi:10.1016/j.ocemod.2013.05.013.

Bryan, K., (1969). A numerical method for the study of the circulation of the world ocean. *Journal of Computational Physics,* 4 (3), 347–376.

Brodeau, L., Barnier, B., Treguier, A.–M., Penduff, T., & Gulev, S. (2010). An ERA40–based atmospheric forcing for global ocean circulation models. *Ocean Modelling, 31*(3), 88–104. doi:10.1016/j.ocemod.2009.10.005.

Campin, J. M., Adcroft, A., Hill, C., & Marshall, J. (2004). Conservation of properties in a free–surface model. *Ocean Modelling, 6* (3), 221–244. doi:10.1016/S1463-5003(03)00009-X.

Cooper, L.W., McClelland, J.W., Holmes, R.M., Raymond, P.A., Gibson, J.J., Guay, C.K., & Peterson, B.J., (2008). Flow–weighted values of runoff tracers ($\delta^{18}O$, DOC, Ba, alkalinity) from the six largest Arctic rivers. *Geophysical Research Letters, 35* (18). doi:10.1029/2008GL035007.

Cowtan, K., & Way, R.G., (2014). Coverage bias in the HadCRUT4 temperature series and its impact on recent temperature trends. *Quarterly Journal of the Royal Meteorological Society 140* (683), 1935-1955, doi:10.1002/qj.2297.

Dee, D.P., Uppala, S.M., Simmons, A.J., Berrisford, P., Poli, P., Kobayashi, S., Andrae, U., Balmaseda, M.A., Balsamo, G., Bauer, P., Bechtold, P., Beljaars, A.C.M., van de Berg, L., Bidlot, J., Bormann, N., Delsol, C., Dragani, R., Fuentes, M., Geer, A.J., Haimberger, L., Healy, B., Hersbach, H., Holm, E.V., Isaksen, L, Kållberg, P., Köller, M., Matricardi, M., McNally, A.P., Monge-Sanz, B.M., Morcrette, J.-J., Park, B.-K., Peubey, C., de Rosnay, P., Tavolato, C., Thépaut, N. & Vitart, F. (2011). The ERA-Interim reanalysis: configuration and performance of the data assimilation system. *Quarterly Journal of the Royal Meteorological Society 137*, 553-597. doi: 10.1002/qj.828

Dickson, R., Rudels, B., Dye, S., Karcher, M., Meincke, J., & Yashayaev, I. (2007). Current estimates of freshwater flux through Arctic and subarctic seas. *Progress in Oceanography 73* (3), 210-230. doi:10.1016/j.pocean.2006.12.003.

Eakins B.W., & Sharman, G.F. (2010). Volumes of the World's Oceans from ETOPO1*, NOAA National Geophysical Data Center, Boulder, CO*. Available at www.ndgc.noaa/gov/mgg/global/etopo1_ocean_volumes.shtml.

Fichefet, T., & Morales Maqueda, M.A. (1997). Sensitivity of a global sea ice model to the treatment of ice thermodynamics and dynamics. *Journal of Geophysical Research 102* (C6), 12609-12646.

List of References

Fichot, C.G., Kaiser, K., Hooker, S.B., Amon, R.M.W., Babin, M., Belanger, S., Walker, S.A., & Benner, R. (2013). Pan-Arctic distributions of continental runoff in the Arctic Ocean. *Scientific Reports 3*, 1053. doi:10.1038/srep01053.

Gataullin, V., Polyak, L., Epstein, O., & Romanyuk, B. (1993). Glaciegenic deposits of the Central Deep: a key to the Late Quaternary evolution of the eastern Barents Sea. *Boreas, 22* (1), 47-58.

Giles, K.A., Laxon, S.W., Ridout, A.L., Wingham, D.J., & Bacon, S. (2012). Western Arctic Ocean freshwater storage increased by wind-driven spin-up of the Beaufort Gyre. *Nature Geoscience, 5* (3), 194-197. doi:10.1038/ngeo1379.

Hansen, B., & Østerhus, S. (2000). North Atlantic-Nordic Seas exchanges. *Progress in Oceanography 45* (2),109-208.

Hanzlick, D., & Aagaard, K. (1980). Freshwater and Atlantic Water in the Kara Sea. *Journal of Geophysical Research: Oceans (1978-2012)* 85 (C9), 4937-4942.

Hartmann, D.L. (1994). Global Physical Climatology. Academic Press, San Diego, CA.

Hibler, W.D. (1979). A Dynamic Thermodynamic Sea Ice Model. *Journal of Physical Oceanography, 9* (4), 815-846.

Holland, M.M., Bitz, C.M., & Tremblay, B (2006). Future abrupt reductions in the summer Arctic sea ice. *Geophysical Research Letters, 33*(23), doi: 10.1029/2006GL028024.

Huang, R.X. (1993). Real freshwater flux as a natural boundary Condition for the salinity balance and thermohaline circulation forced by evaporation and precipitation. *Journal of Physical Oceanography, 23* (11), 2428-2446.

Huerta-Casas, A. M., & Webb, D. J. (2012). High frequency fluctuations in the heat content of an ocean general circulation model. *Ocean Science 8* (5), 813-825. doi:10.5194/os-8-813-2012.

Hunke, E., & Dukowicz, J., (1997). An Elastic-Viscous-Plastic Model for Sea Ice Dynamics. *Journal of Physical Oceanography 27* (9), 1849-1867.

Ikawa, M., & Saito, K., (1991). Description of a non-hydrostatic model developed at the Forecast Research Department of the MRI. *MRI Technical Report 28,* 238pp.

Jackett, D. R., & McDougall, T. J. (1995). Minimal adjustment of hydrographic profiles to achieve static stability. *Journal of Atmospheric and Oceanic Technology*, *12* (2), 381-389.

Jakobsson, M., Mayer, L., Coakley, B., Dowdeswell, J.A., Forbes, S., Fridman, B., Hodnesdal, H, Noormets, R, Pedersen, R, Rebesco, M, Schenke, H.W., Zarayskaya, Y., Accettella, D., Armstrong, A., Anderson, R.M., Bienhoff, P., Camerlenghi, A., Church, I., Edwards, M., Gardner, J.V., Hall, J.K., Hell, B., Hestvik, O., Kristoffersen, Y., Marcussen, C., Mohammad, R., Mosher, D., Nghiem, S.V., Pedrosa, M.T., Travaglini, P.G., & Weatherall, P. (2012). The International Bathymetric Chart of the Arctic Ocean (IBCAO) Version 3.0. *Geophysical Research Letters 39*, L12609. doi: 10.1029/2012GL052219.

Jones, E.P. (2001). Circulation in the Arctic Ocean. *Polar Research*, *20* (2), 139-146.

Jungclaus, J. H., Haak, H., Latif, M., & Mikolajewicz, U. (2005). Arctic–North Atlantic interactions and multidecadal variability of the meridional overturning circulation. *Journal of Climate*, *18* (19), 4013–4031. doi:10.1175/JCLI3462.1.

Karcher, M., Kauker, F., Gerdes, R,. Hunke. E,. & Zhang, J. (2007). On the dynamics of Atlantic Water Circulation in the Arctic Ocean. *Journal of Geophysical Research: Oceans (1978–2012), 112* (C4). doi:01.1029/2006JC003630.

Kwok, R., Maslowski, W., & Laxon, S. (2005). On large outflows of Arctic sea ice into the Barents Sea. *Geophysical Research Letters, 32* (22). doi:10.1029/2005GL024485.

Kwok, R., & Rothrock, D.A. (2009), Decline in Arctic sea ice thickness from submarine and ICESat records: 1958–2008. *Geophysical Research Letters, 36* (5). doi:20.1029/2009JC005312.

Langehaug, H.R., Geyer, F., Smedsrud, L.H., & Gao, Y. (2013). Arctic sea ice decline and ice export in the CMIP5 historical simulations. *Ocean Modelling 71*, 114–126, doi: 10.1016/j.ocemod.2012.12.006.

Large, W.G., & Yeager, S.G. (2009). The global climatology of an interannually varying air–sea flux data set. *Climate Dynamics, 33*(2–3), 341–364. doi 10.1007/s00382–008–0331–3

Lenn, Y.D., Wiles, P.J., Torres–Valdes, S., Abrahamsen, E.P., Rippeth, T.P., Simpson, J.H., Bacon, S., Laxon, S.W., Polyakov, I., Ivanov, V., & Kirilov, S. (2009). Vertical mixing at intermediate depths in the Arctic boundary current. *Geophysical Research Letters, 36* (5), doi: 10.1029/2008GL036792.

Levier, B., Tréguier, A. M., Madec, G., & Garnier, V. (2007). Free surface and variable volume in the NEMO code. *MERSEA IP report WP09–CNRS–STR03–1A*,

47pp. Available at www.nemo-ocean.eu/content/download/258/1661/file/NEMO_vvl_report.pdf.

Levitus, S., Boyer, T., Conkright, M., O'Brien, T., Antonov, J., Stephens, C., Stathoplos, L., Johnson, D., & Gelfield, R. (1998). *NOAA Atlas NESDIS 18, World Ocean Database 1998*, Introduction, vol. 1, U.S. Government Printing Office, Washington D.C.

Lewis, E. L., & Jones, E. P. (Eds.). (2000). *The freshwater budget of the Arctic Ocean* (Vol. 70). Springer.

Macdonald, R.W., Barrie, L.A., Bidleman, T.F., Diamond, M.L., Gregor, D.J., Semkin, R.G., Strachan, W.M.J., Li, Y.F., Alaee, M., Alexeeva, L.B., Backus, S.M., Bailey, R., Bewers, J.M., Gobeil, C., Halsall, C.J., Harner, T., Hoff, J.T., Jantunen, L.M.M., Lockhart, W.L., Mackay, D., Muir, D.C.G, Pudykeiwicz, J., Reimer, K.J., Smith, J.N., Stern, G.A., Schroeder, W.H., Wagemann, R., & Yunker, M.B. (1999). Contaminants in the Canadian Arctic: 5 years of progress in understanding sources, occurrence and pathways. *Science of The Total Environment 254*(2-3), 93-234.

Madec, G. (2008). NEMO ocean engine*. Note du Pole de modélisation, Institut Pierre-Simon Laplace (IPSL), France,* No. 27 ISSN No 1288-1619.

Madec, G., & Delecluse, P. (1997), The opa/arpege and opa/lmd global ocean-atmosphere coupled model. *Int. WOCE Newsletter, 26*, 12-15.

MacDonald, G.M., Kremenetski, K.V., Smith, L.C., & Hidalgo, H.G. (2007). Recent Eurasian river discharge to the Arctic Ocean in the context of longer-term dendrohydrological records. *Journal of Geophysical Research: Biogeosciences (2005-2012), 112* (G4). doi:10.1029/2006JG000333.

McLaughlin, F.A,. Carmack, E.C., Macdonald, R.W., Melling, H., Swift, J.H., Wheeler, P.A., Sherr, B.F., & Sherr, E.B. (2004). The joint roles of Pacific and Atlantic-origin waters in the Canada Basin, 1997-1998. *Deep-Sea Research Part I, 51(1)*, 107-128. doi: 10.1016/j.dsr.2003.09.010.

McPhee, M.G., Stanton, T.P., Morison, J.H., & Martinson, D.G., (1998). Freshening of the upper ocean in the Arctic: Is perennial sea ice disappearing? *Geophysical Research Letters, 25* (10), 1729-1732.

McPhee, M.G., Proshutinsky, A., Morison, J.H, Steele, M., & Alkire, M.B. (2009). Rapid change in freshwater content of the Arctic Ocean. *Geophysical Research Letters, 36* (10), doi:10.1029/2008GL037525.

Meincke, J., Rudels, B., & Friedrich, H.J. (1997). The Arctic Ocean-Nordic Seas thermohaline system. *ICES Journal of Marine Science: Journal du Conseil 54* (3), 283-299.

Menard, H. W., & Smith, S. M. (1966). Hypsometry of ocean basin provinces. *Journal of Geophysical Research*, *71* (18), 4305-4325.

Millero, F. J., Chen, C. T., Bradshaw, A., & Schleicher, K. (1980). A new high pressure equation of state for seawater. *Deep Sea Research Part A. Oceanographic Research Papers*, *27* (3), 255-264.

Molines, J.M. (2006). CDFTOOLS: a fortran 90 package of programs and libraries for diagnostic of the DRAKKAR OPA9 output. www-meom.hmg.inpg.fr/CDFTOOLS/cdftools-2.1.html.

Murray, R.J. (1996). Explicit Generation of Orthogonal Grids for Ocean Models, *Journal of Computational Physics*, 126 (2), 251-273.

Nurser, A. J. G., & Bacon, S. (2013). Eddy length scales and the Rossby radius in the Arctic Ocean. *Ocean Science Discussions*, *10* (5), 1807-1831. doi:10.5194/osd-10-1807-2013.

O'Dwyer J., Kasajima, Y., & Nøst, O.A., (2001). North Atlantic Water in the Barents Sea Opening, 1997 to 1999, *Polar Research 20* (2), 209-216.

Overland, J.E., & Roach, A.T. (1987). Northward Flow in the Bering and Chukchi Seas. *Journal of Geophysical Research 92* (C7), 7097-7105.

Overland, J.E., & Turet, P. (1994). Variability of the Atmospheric Energy Flux across 70°N computed from the GFDL data set, in *The Polar Oceans and Their Role in Shaping the Global Environment* (eds O.M Johannesen, R.D. Muench and J.E. Overland), 313-325.

Overland, J.E., Turet, P., & Oort, A.H. (1996). Regional variations of moist static energy flux into the Arctic. *Journal of Climate, 9* (1), 54-65.

Penduff, T., Barnier, B., Molines J.-M., & Madec, G. (2005). On the use of current meter data to assess the realism of ocean model simulations, *Ocean Modelling, 11* (3) 399-416. doi:10.1016/j.ocemod.2005.02.001.

Peterson, B.J., Holmes, R.M., McClelland, J.W., Vörösmarty, C.J., Lammers, R.B., Shiklomanov, A.I., Shiklomanov, I.A., & Rahmstorf, S. (2002). Increasing River Discharge to the Arctic Ocean*, Science*, Vol 298. doi:10.1126/science.1077445.

Polyakov, I. V., Timokhov, L. A., Alexeev, V. A., Bacon, S., Dmitrenko, I. A., Fortier, L., Frolov, I.E., Gascard., J.-C., Hansen, E., Ivanov, V.I., Laxon., S., Mauritzen, C., Perovich, D., Shimada, K., Simmons, H.L., Sokolov, V.T., Steele, M., & Toole, J. (2010). Arctic Ocean warming contributes to reduced polar ice

cap. *Journal of Physical Oceanography*, *40* (12), 2743-2756. doi:10.1175/2010JPO4339.1

Popova, E., Yool, A., Coward, A., Dupont, F., Deal, C., Elliot, S., Hunke, E., Jin, M., Steele, M., & Zhang, J. (2012). What controls primary production in the Arctic Ocean? Results from an ecosystem model intercomparison. *Journal of Geophysical Research 117*, C00D12. doi:10.1029/2011JC007112.

Popova, E.E., Yool, A., Aksenov, Y., Coward, A.C., & Anderson, T.R. (2014). Regional variability of acidification in the Arctic: a sea of contrasts. *Biogeosciences 11*, 293-308, doi:10.5194/bg-11-293-2014.

Press, W. H., Flannery, B. P., Teukolsky, S. A., & Vetterling, W. T. (1992). *Numerical Recipes in FORTRAN 77: Volume 1, Volume 1 of Fortran Numerical Recipes: The Art of Scientific Computing* (Vol. 1). Cambridge University Press.

Proshutinsky, A.Y., & Johnson, M.A. (1997). Two circulation regimes of the wind-driven Arctic Ocean. *Journal of Geophysical Research, 102*(C6), 12493-12514. doi: 10.1029/97JC00738

Rabe, B., Karcher, M., Kauker, F., Schauer, U., Toole, J.M., Krishfield, R.A., Pisarev, S., Kikuchi, T., & Su, J. (2014). Arctic Ocean basin liquid freshwater storage trend 1992-2012. *Geophysical Research Letters, 41* (3), 961-968. doi: 10.1002/2013GL058121.

Rattan, S., Myers, P.G., Treguier, A.-M., Theetten, S., Biastoch, A., Böning, & C. (2010). Towards an understanding of Labrador Sea salinity drift in eddy-permitting simulations. *Ocean Modelling, 35* (1), 77-88. doi:10.1016.j.ocemod.2010.06.007.

Rigor, I.G., Colony, R.L., & Martin, S. (2000). Variations in Surface Air Temperature Observations in the Arctic, 1979-97. *Journal of Climate 13*, 896-914.

Rigor, I.G., Wallace, J.M., & Colony, R.L. (2002). Response of Sea Ice to the Arctic Oscillation, *Journal of Climate 15*(18), 2648-2663. doi: 10.1175/1520-0442(2002)015<2648:ROSITT>2.0.CO;2.

Rind, D., Healy, R., Parkinson, C., & Martinson, D. (1995). The role of sea ice in $2xCO_2$ climate model sensitivity. Part I: the total Influence of sea ice thickness and extent. *Journal of Climate, 8* (3), 449-463.

Roullet, G., & Madec, G. (2000). Salt conservation, free surface, and varying levels: a new formulation for ocean general circulation models. *Journal of Geophysical Research*, *105* (C10), 23927-23942.

Ruddimann, W.F. (2001). *Earth's Climate Past and Future*. New York, NY, W.H. Freeman and Company.

Rudels, B. (1989). The formation of polar surface water, the ice export and the exchanges through the Fram Strait. *Progress in Oceanography*, *22* (3), 205-248.

Rudels, B., Larsson, A.-M., & Sehlstedt, P-I (1991). Stratification and water mass formation in the Arctic Ocean: some implications for the nutrient distribution. *Polar Research 10* (1), 19-32.

Rudels, B., Anderson, L.G., & Jones, E.P., (1996). Formation and evolution of the surface mixed layer and halocline of the Arctic Ocean. *Journal of Geophysical Research: Oceans (1978-2012), 101*(C4), 8807-8821.

Rudels, B., Jones, E.P., Schauer, U., & Eriksson, P. (2004). Atlantic sources of the Arctic Ocean surface and halocline waters. *Polar Research 23* (2), 181-208. doi: 10.1111/j.1751-8369.2004.tb00007.x.

Rudels, B. (2010). Constraints on exchanges in the Arctic Mediterranean – do they exist and can they be of use? *Tellus A, 62* (2), 109-122. doi.1111/j.1600-0870.2009.00425.x

Salmon, D. K., & McRoy, C. P. (1994). Nutrient-based tracers in the western Arctic: a new lower holocline water defined. *Geophysical Monograph Series*, *85*, 47-61.

Schauer, U., Loeng, H., Rudels, B., Ozhigin, V. K., & Dieck, W. (2002). Atlantic water flow through the Barents and Kara Seas. *Deep Sea Research Part I: Oceanographic Research Papers*, *49* (12), 2281-2298.

Schauer, U., & Beszczynska-Möller, A. (2009). Problems with estimation and interpretation of oceanic heat transport-conceptual remarks for the case of Fram Strait in the Arctic Ocean. *Ocean Science*, *5* (4), 487-494. doi:10.5194/os-5-487-2009.

Schlosser, P., Bauch, D., Fairbanks, R., & Bönisch, G. (1994). Arctic river-runoff: mean residence time on the shelves and in the halocline. *Deep Sea Research Part I: Oceanographic Research Papers, 41* (7), 1053-1068.

Screen, J.A., Simmonds, I. (2010). The central role of diminishing sea ice in recent Arctic temperature amplification. *Nature 464* (7293), 1334-1337. doi:101038/nature09051.

Semtner Jr, A.J. (1976). A model for the thermodynamic growth of sea ice in numerical investigations of climate. *Journal of Physical Oceanography 6* (3), 379-389.

Serreze, M.C., Maslanik, J.A., Scambos, T.A., Fetterer, F., Stroeve, J., Knowles, K., Fowler, C., Drobot, S., Barry, R.G., Haran, T.M. (2003). A record minimum arctic sea ice extent and area in 2002. *Geophysical Research Letters 30*(3). doi: 10.1029/2002GL016406.

Serreze, M.C, Barrett, A.P., Slater, A.G., Woodgate, R.A., Aagaard, K., Lammers, R.B., Steele, M., Moritz, R., Meredith, M., & Lee, C.M. (2006). The large-scale freshwater cycle of the Arctic. *Journal of Geophysical Research: Oceans (1978–2012), 111* (C11). doi:10.1029/2005JC003424.

Serreze, M.C., Barrett, A.P., Slater, A.G., Steele, M., Zhang, J., & Trenberth, K.E. (2007). The large scale energy budget of the Arctic. *Journal of Geophysical Research: Atmospheres (1984–2012), 112* (D11). doi:19.1029/2006JD008230.

Shchepetkin, A.F & McWilliams, J.C. (2011). Accurate Boussinesq Oceanic Modelling with a Practical, "Stiffened" Equation of State, *Ocean Modelling, 38* (1), 41–70. doi:10.1016/j.ocemod.2011.01.010.

Singh, P., & Singh, V.P. (2001). *Snow and Glacier Hydrology*. Kluwer Academic Press. ISBN 0-7923-6767-7.

Skagseth, Ø. (2008). Recirculation of Atlantic Water in the western Barents Sea. *Geophysical Research Letters, 35* (11), DOI: 10.1029/2008GL033785.

Smedsrud, L.H, Ingvaldsen, R., Nilsen, J.E.Ø., & Skagseth, Ø. (2010). Heat in the Barents Sea: transport, storage, and surface fluxes. *Ocean Science 6*, 219–234. doi: 10.5194/os-6-219-2010.

Smedsrud, L.H., Esau, I., Ingvaldsen, R.B., Eldevik, T., Haugan, P.M., Li, C., Lien, V.S., Olsen, A., Omar, A.M., Otterå, O.H., Risebrobakken, B., Sandø, A.B., Semenov, V.A., & Sorokina, S.A. (2013). The Role of the Barents Sea in the

Arctic Climate System. *Reviews of Geophysics, 51* (3), 415–449. doi: 10.1002/rog.20017.

Smethie, W. M., Schlosser, P., Bönisch, G., & Hopkins, T. S. (2000). Renewal and circulation of intermediate waters in the Canadian Basin observed on the SCICEX 96 cruise. *Journal of Geophysical Research: Oceans (1978–2012)*, *105* (C1), 1105–1121.

Steele, M., Morley, R., & Ermold, W. (2001). PHC: A Global Ocean Hydrography with a High-Quality Arctic Ocean. *Journal of Climate, 14* (9), 2079–2087. doi: 10.1175/1520-0442(2001)014.

Stephens, M.A. (1984). EDF Statistics for Goodness of Fit and Some Comparisons, *Journal of the American Statistical Association 69*, 730–737.

Stommel, H. (1984). The delicate interplay between wind-stress and buoyancy input in ocean circulation: the Goldsbrough variations. *Tellus A 36* (2), 111–119.

Strass, V.H., Fahrback, E., Schauer, U., & Sellman, L. (1993). Formation of Denmark Strait Overflow Water by Mixing in the East Greenland Current. *Journal of Geophysical Research: Oceans (1978–2012), 98* (C4), 6907–6919

Stroeve, J.C., Holland, M.M., Meier., W., Scambos, T., & Serreze, M.C. (2007). Arctic sea ice decline: Faster than forecast. *Geophysical Research Letters, 34*(9), doi: 10.1029/2007GL029703

Stroeve, J.C., Maslanik, J., Serreze, M.C., Rigor, I., Meier, W., & Fowler, C. (2011). Sea ice response to an extreme negative phase of the Arctic Oscillation during 2009/2010. *Geophysical Research Letters 38* (2), doi:10.1029/2010GL045662.

Tartinville, B., Campin, J.-M., Fichefet, T., & Goosse, H. (2001). Realistic representation of the surface freshwater flux in an ice-ocean general circulation model, *Ocean Modelling 3*, 95-108.

Teigen, S.H., Nilsen, F., Skogseth, R., Gjevik, B., & Beszczynska-Möller, A. (2011). Baroclinic instability in the West Spitzbergen Current. *Journal of Geophysical Research 116*, C07012. doi:10.1029/2011JC006974.

Thiede, J., Pfirman, S., Schenke, H-W.,& Reil, W. (1990). Bathymetry of Molloy Deep: Fram Strait between Svalbard and Greenland. *Marine Geophysical Researches, 12* (3), 197-214.

Thompson, D.W.J., & Wallace, J.M., (1998). The Arctic Oscillation signature in the wintertime geopotential height and temperature fields, *Geophysical Research. Letters, 25*(9), 1297-1300.

Timmermans, M.-L., Toole, J., Proshutinsky, A., Krishfield, R., & Plueddemann, A. (2008). Eddies in the Canada Basin, Arctic Ocean, observed from ice-tethered profilers. *Journal of Physical Oceanography*, *38* (1), 133-145. doi:10.1175/2007JPO3782.1.

Trenberth, K., Koike, T., & Onogi, K., (2008). Progress and prospects for reanalysis for weather and climate. *Eos, Transactions American Geophysical Union,* 89 (26), 234-235. doi: 10.1029/2008EO260002

Tsubouchi, T., Bacon, S., Garabato, A. N., Aksenov, Y., Laxon, S. W., Fahrbach, E., & Ingvaldsen, R. B. (2012). The Arctic Ocean in summer: A quasi-synoptic inverse estimate of boundary fluxes and water mass transformation. *Journal of Geophysical Research: Oceans (1978–2012)* , *117* (C1). doi:10.1029/2011JC007174.

Tverberg, V., Nøst, O.A., Lydersen, C., & Kovacs, K.M. Winter sea ice melting in the Atlantic Water subduction area, Svalbard *Norway Journal of Geophysical Research: Oceans 119*, 5945–5967. doi 10.1002/2014JC010013.

Vancoppenolle, M., Bopp, L., Madec, G., Dunne, J., Ilyina, T., Halloran, P.R., & Steiner, N. (2013). Future Arctic Ocean primary productivity from CMIP5 simulations: Uncertain outcome, but consistent mechanisms. *Global Biogeochemistry Cycles 27*. doi:10.1002/gbc.20055

Wang, M., & Overland, J.E. (2009). A sea ice free summer Arctic within 30 years? *Geophysical Research Letters, 36*(7), doi: 10.1029/2009GL037820.

Wassmann, P., Duarte, C.M., Agustí, S., & Sejr, M.K. (2011). Footprints of climate change in the Arctic marine ecosystem. *Global Change Biology 17: 1235–1249.* doi: 10.1111/j.1365–2486.2010.02311.

Webster, P.J. (1994). The role of hydrological processes in ocean–atmosphere interactions. *Reviews of Geophysics, 32* (4), 427–476.

Woodgate, R.A., Weingartner, T.J., & Lindsay, R. (2012). Observed increases in Bering Strait oceanic fluxes from the Pacific to the Arctic from 2001 to 2011 and their impacts on the Arctic Ocean water column. *Geophysical Research Letters 39*(24). doi: 10.1029/2012GL054092.

Yang, D., Shi, X., & Marsh, P. (2014). Variability and extreme of Mackenzie River daily discharge during 1973–2011*. Quaternary International (2014)*. doi:10.1016/j.quaint.2014.09.023